Light Hadron Spectroscopy and Soft Covariant Gauges in Lattice QCD

Sinéad M. Ryan

Doctor of Philosophy

The University of Edinburgh

1996

For my parents

Abstract

In this thesis two aspects of Lattice QCD are studied, the light hadron spectrum and decay constants and a stochastic gauge-fixing procedure.

Chapter 2 is an investigation of the effects of tadpole improvement on the Sheikholeslami-Wohlert clover action at $\beta = 6.2$. The mass spectra and decay constants of the two actions are compared using 60 gauge field configurations. Changing the value of the clover coefficent is found to have little effect on spectral quantities at this β value but reference is made to a similar study at $\beta = 5.7$ where greater effects are seen. The decay constants show a statistically significant c dependence. However, it is argued that without a non-perturbative value for the renormalisation constants Z_A and Z_V a conclusive statement cannot be made.

In Chapter 3 a complete study of the quenched, light hadron spectrum and decay constants at $\beta = 6.2$ is done, using 220 tadpole improved gauge field configurations and quark propagators with local and fuzzed sources. Using data at two additional β values, 6.0 and 5.7 the effects of scaling are investigated. The pseudoscalar and vector decay constants are calculated and ratios of decay constants are compared with their experimental values.

Chapter 4 describes a preliminary study of a new, covariant, one parameter gauge-fixing procedure. This scheme avoids the problem of Gribov copies by imposing a "soft" gauge fixing condition. Varying the gauge-fixing parameter allows a study of gauge dependence. Details of the lattice scheme and the algorithm to implement it are given. The behaviour of the internal energy of the system, the specific heat and the zero momentum gluon propagator is monitored. Results for the gauge dependence of the gluon propagator are presented.

Acknowledgements

I would like to thank my supervisors, Ken Bowler and Richard Kenway for allowing me to spend three wonderful years in Edinburgh. I am indebted to Claudio Parrinello for his help and enthusiasm throughout the project which is chapter 4 of this thesis and to David Henty who was always willing to help, even having left the department. Much gratitude, also to the British Council and in particular Monica Paterson, for the financial support I have received while in Edinburgh.

Emma, Katy, Mireia and Triona have all, at one time or another, rescued me from the world of physics and especially during these last months, made sure that I remember to eat !

Thanks to all the Edqcd-ers, but especially to Harry and Orlando with whom I have shared an office, coffee breaks and many crises, for making life in JCMB (and outwith !) such fun.

Finally, my deepest thanks go to my family. They have provided the moral support and encouragement during my student life which has made all the difference.

Contents

Chapter 1

Introduction

Quantum chromodynamics (QCD) is the gauge theory of the strong interaction, based on the unbroken, non-Abelian group $SU(3)$. The quanta of the theory are the gluons which mediate the strong interaction between particles, carrying colour charge. The theory is asymptotically free, as a consequence of the non-Abelian structure of the gauge group [3, 4, 5], so that interquark forces become small at small separations. This property ensures that perturbation theory, a standard field theoretic technique, accurately describes short distance, high energy physics. However, the correct theory of the strong interaction, must also describe the low energy, mass spectrum of particles and matrix elements between particle states, which are observed experimentally. At the length scales relevant to observable quantities the coupling is $\mathcal{O}(1)$ and perturbation theory becomes unreliable, making a non-perturbative formalism of QCD essential.

To date, Lattice QCD is the most successful non-perturbative theory of the strong interaction. Formulating QCD on a lattice provides a theory in which *ab initio* calculations of physical observables can be made, to an accuracy limited only by the available computational resources.

Within Lattice QCD, there are two possible strategies with which to probe the theory. The first is to study the quark and gluon propagators themselves. These are fundamental quantities and as such are expected to yield much information about features of QCD *e.g.* confinement. However, this study is complicated by the "non-physical" nature of these objects. This is explored in more detail in Chapter 4, using a new, gauge-fixing algorithm.

The second approach, and the most widely used, is to study the hadron spectrum of masses and the matrix elements between hadronic states. This thesis is mainly

concerned with a determination of the light hadron spectrum (hadrons made from u, d and s quarks). This is a central goal of Lattice QCD : such a successful calculation would be both a validation of QCD, as the theory of the strong interaction and of Lattice QCD as a computational tool.

In this chapter, a brief overview of Lattice QCD is given, focusing on the move from the continuum theory to the lattice, on the calculation of observables and the associated systematic and statistical errors and finally, on how to relate quantities calculated on a lattice to the analagous continuum quantity.

1.1 Lattice QCD from Continuum QCD

A starting point for the numerical simulation of QCD is to work in Euclidean space. A Wick rotation

$$t \longrightarrow \tau = it, \tag{1.1}$$

accomplishes this by continuing the space-time signature from $(1,-1,-1,-1)$ to $(1,1,1,1)$. The move from Minkowski to Euclidean space has two advantages. Firstly, the oscillatory nature of the continuum path-integral makes sampling the configuration space an extremely unreliable procedure. The Euclidean action, $S_E = iS_{\text{cont}}$, is exponentially damped which calms this behaviour. Secondly, the functional integral in the Euclidean theory is analogous to the partition function of a classical statistical mechanics system, for which numerical techniques are already available.

The gamma matrices of the theory are defined to satisfy the algebra,

$$\{\gamma_\mu^E, \gamma_\nu^E\} = 2\delta_{\mu\nu}, \tag{1.2}$$

$$\gamma_\mu^{E\dagger} = \gamma_\mu^E, \tag{1.3}$$

for the Hermitian choice

$$\gamma_0 = \gamma_4^E, \quad -i\gamma_i = \gamma_i^E \quad \text{and} \quad \gamma_5 = \gamma_5^E. \tag{1.4}$$

With this choice the Euclidean, continuum QCD action is

$$S = \int d^4x \, \frac{1}{4} F_{\mu\nu} F^{\mu\nu} + \overline{\psi}(x)(\not{D} + m)\psi(x), \tag{1.5}$$

where $\overline{\psi}(x)$ and $\psi(x)$ are the quark fields at a point x. They carry flavour, Dirac spinor and colour indices, which are suppressed here for clarity. The covariant derivative, $\not{D}$ which makes the action invariant under local gauge transformations is defined by

$$D_\mu = \partial_\mu - igA_\mu \quad \text{and} \quad \not{D} = \gamma^\mu D_\mu, \tag{1.6}$$

and, in analogy with the Riemann curvature tensor, the field strength tensor, $F_{\mu\nu}$ describes the gauge part of the action and is defined as

$$F_{\mu\nu} \equiv \partial_\mu A^a_\nu(x) - \partial_\nu A^a_\mu(x) + g f^{abc} A^b_\mu A^c_\nu. \tag{1.7}$$

The gauge fields, $A_\mu(x)$ are elements of $su(N)$ the Lie Algebra of $SU(N)$, such that

$$A_\mu(x) = A^a_\mu T^a, \tag{1.8}$$

where T^a are the generators of the group. They are traceless, hermitian matrices satisfying, in particular for $SU(3)$

$$\left[T^a, T^b\right] = i f_{abc} T_c, \tag{1.9}$$

and

$$T_a = \frac{\lambda_a}{2} \quad ; \quad a = 1, \ldots 8, \tag{1.10}$$

and with the normalisation $\mathrm{Tr}\,(T_a T_b) = \frac{1}{2}\delta_{ab}$.

The action in Equation (1.5) is invariant under local gauge transformations, $\Lambda(x) \in SU(3)$, in which the quark and gluon fields transform in the following

way,

$$\psi(x) \longrightarrow \Lambda(x)\psi(x), \tag{1.11}$$

$$\overline{\psi}(x) \longrightarrow \overline{\psi}(x)\Lambda^{-1}(x), \tag{1.12}$$

$$A_\mu(x) \longrightarrow \Lambda(x)A_\mu(x)\Lambda^{-1}(x) - \frac{1}{ig}\left(\partial_\mu\Lambda(x)\right)\Lambda^{-1}(x). \tag{1.13}$$

Having defined a Euclidean theory, it is then mapped from the continuum to a hypercubic lattice, of finite volume and non-zero lattice spacing, a. In principle the continuum theory can be recovered by taking this lattice spacing to zero, the naive continuum limit. This will be discussed further towards the end of this chapter.

The lattice is a natural regulator of the field theory, introducing a UV cutoff in momentum space. The momenta, on a periodic lattice of spatial extent, aN_s, have the discrete values

$$\vec{p} = \frac{2\pi}{aN_s}(n_1, n_2, n_3), \quad \text{with} \quad -N_s/2 < p < N_s/2, \tag{1.14}$$

so that each component is bounded by π/a.

To arrive at a lattice action for QCD, the continuum field variables must be associated with their lattice counterparts. Consider the gauge fields, $A_\mu(x)$. They have the same function as the Christoffel symbols (connections) in general relativity. To compare two infinitesimally separated quark fields $\psi(x)$ and $\psi(x+dx)$ they must be considered at the same point in space-time using parallel transport. An $SU(N)$ matrix associated with a path in spacetime, which parallel transports the field $\psi(x)$ along a curve, $\mathcal{C}$ to the field $\psi(x+dx)$ is defined by

$$\mathcal{U}(\mathcal{C}_{\mathbf{x}+d\mathbf{x},\mathbf{x}}) \equiv 1 - A_\mu(x)dx^\mu. \tag{1.15}$$

The effect of many parallel transports can be generalised from the above, to

describe how a finite path is traversed, as [6]

$$\mathcal{U}(\mathcal{C}) = \mathcal{P}\exp^{\int_C A_\mu dx^\mu}. \tag{1.16}$$

$\mathcal{P}$ is a path ordering similar to the time ordering operator, acting on the matrices, $A_\mu(x)$ such that $A_\mu(x_1)$ is placed to the right of $A_\mu(x_2)$ if the curve $\mathcal{C}$ reaches x_1 before x_2.

On a lattice with spacing, a, the links provide the shortest non-zero path between any two points, so the parallel transporters, $\mathcal{U}$, are naturally associated with the links, U in the following way

$$U_\mu(x) \equiv \mathcal{P}\exp^{iagA_\mu\left(x+\frac{a\mu}{2}\right)} \quad \in SU(N), \tag{1.17}$$

where, g is the bare coupling of the theory and the continuum integral has been replaced by a midpoint approximation in the usual spirit of discretisation. A lattice of extent L has periodic boundary conditions if $U_\mu(x)$ and $U_\mu(x+\nu L)$ are identified.

In this way the quark fields, $\overline{\psi}(x)$ and $\psi(x)$ are associated with the sites on the lattice and the gluon fields with the links between them. The variables of the lattice field theory are thus defined on a finite number of points and since the gauge group is compact, all integrals are made finite. Numerical simulations are now possible.

There are two types of gauge-invariant objects which can be constructed from the links on the lattice :

A string terminated by a fermion at one end and an antifermion at the other,

$$\overline{\psi}(x)U_\mu(x)\ldots U_\nu(y-\hat{\nu})\psi(y). \tag{1.18}$$

The trace of a closed string (Wilson loop), the simplest of which is the pla-

quette,

$$P_{\mu\nu} = \mathrm{Tr}\left[U^{\square}_{\mu\nu}(x)\right], \tag{1.19}$$

$$\text{with} \quad U^{\square}_{\mu\nu}(x) = U_{\mu}(x)U_{\nu}(x+\hat{\mu})U^{\dagger}_{\mu}(x+\hat{\nu})U^{\dagger}_{\nu}(x). \tag{1.20}$$

1.1.1 The Gauge Action

Using these definitions the gluonic part of the action can now be discretised, in terms of the link variables, preserving the local gauge invariance, with the substitution,

$$\begin{aligned} S_G &= \int d^4x \frac{1}{4} F_{\mu\nu}F^{\mu\nu}, \\ &\longrightarrow \frac{2N_c}{g^2}\sum_x \sum_{\mu>\nu}\left[1 - \frac{1}{N_c}\Re\mathrm{e}\mathrm{Tr}U^{\square}_{\mu\nu}(x)\right]. \end{aligned} \tag{1.21}$$

The bare coupling, g is related to β through

$$\beta = \frac{2N_c}{g^2}, \tag{1.22}$$

and $U^{\square}_{\mu\nu}(x)$ is the Wilson loop from Equation (1.20). The constant term is ignored so the gauge action becomes

$$S_G = -\frac{\beta}{N_c}\sum_x \sum_{\mu>\nu} \Re\mathrm{e}\mathrm{Tr}U^{\square}_{\mu\nu}(x), \tag{1.23}$$

where the sum $\sum_{\mu<\nu}$ is for $1 \leq \nu < \mu$. The lattice field strength tensor, $F^{\mathrm{lat}}_{\mu\nu}$, is also defined in terms of the links, from its continuum equivalent, to be

$$F^{\mathrm{lat}}_{\mu\nu} = \frac{1}{4}\frac{1}{2ig}\left[U^{\square}_{\mu\nu} - U^{\square\dagger}_{\mu\nu}\right]. \tag{1.24}$$

1.1.2 The Fermion Action

Naively discretising the fermionic part of the action by replacing continuum derivatives with finite differences gives

$$\begin{aligned} S_F &= \int d^4x\, \overline{\psi}(x)\,(\not{D} + m)\,\psi(x), \\ &\longrightarrow \sum_x \left\{ \sum_{\mu=1}^{d} \overline{\psi}(x)\gamma_\mu \left[U_\mu(x)\psi(x+\hat{\mu}) - U_\mu^\dagger(x-\hat{\mu})\psi(x-\hat{\mu}) \right] \right\} \\ &\quad + \sum_x \left\{ m\overline{\psi}(x)\psi(x) \right\}. \end{aligned} \tag{1.25}$$

This leads to the species doubling problem - a consequence of the zeros of $\sin p_\mu$ in the free fermion propagator

$$M_{xy}^{-1} = \int_{-\frac{\pi}{2},\frac{3\pi}{2}} \frac{d^dk}{(2\pi)^d} \frac{\exp^{ip(x-y)}}{m + i\sum_\mu \gamma_\mu \sin p_\mu}, \tag{1.26}$$

occurring at, $p_\mu = 0$ and $p_\mu = \pi$, corresponding to the edges of the Brillouin zone. In four dimensions, Equation (1.25) corresponds to a continuum theory with 2^4 non-interacting, equal mass, fermions.

A theorem by Nielson and Ninomiya [7] (the "No-Go" theorem) says that such doubling is a feature of any reasonable, lattice regularisation scheme. The theorem states that for a local lattice action that is bilinear, translationally invariant, Hermitian and with continuous chiral symmetry the continuum limit will contain multiple fermion species in opposite chirality pairs.

There are two approaches which have been successful in handling the fermion doubling problem. The first is the staggered fermion approach whereby the size of the Brillouin zone is reduced by effectively doubling the lattice spacing and thus eliminating some of the unwanted modes. This is achieved by distributing the fermionic degrees of freedom on the lattice such that for each Grassmann-variable the lattice spacing is effectively $2a$. The second, the Wilson fermion method, exploits the non-uniqueness of the action to break chiral symmetry. Any discretisation for which the continuum theory is recovered at the zero lattice spacing limit

is valid. Therefore, the action is modified by the addition of a higher order term which conspires to make $(2^d - 1)$ fermions infinitely heavy in the continuum limit. For the purposes of this thesis, only Wilson fermions are considered.

Wilson's proposed fermion action is [10]

$$\begin{aligned} S_{W_F} &= \sum_x \Bigg\{ \sum_{\mu=1}^{d} \overline{\psi}(x)\gamma_\mu \left[U_\mu(x)\psi(x+\hat{\mu}) - U_\mu^\dagger(x-\hat{\mu})\psi(x-\hat{\mu}) \right] + m\overline{\psi}(x)\psi(x) \\ &\quad -\frac{r}{2}\sum_{\mu=1}^{d} \overline{\psi}(x) \left[U_\mu(x)\psi(x+\hat{\mu}) + U_\mu^\dagger(x-\hat{\mu})\psi(x-\hat{\mu}) - 2\psi(x) \right] \Bigg\}, \end{aligned} \tag{1.27}$$

where r is an arbitrary nonzero constant which has no physical meaning, since the Wilson term must vanish in the classical, continuum limit. It is therefore set equal to one. The action has been made gauge-invariant by introducing the gauge fields on the links joining point-split fermion fields. This action can be expressed more compactly as follows

$$S_{W_F} = \sum_{x,y} \frac{1}{2\kappa} \overline{\psi}(x) \mathcal{M}_{W_F}(x,y;U)\psi(y), \tag{1.28}$$

where κ is the hopping parameter, defined as

$$\kappa = \frac{1}{8 + 2am_q}. \tag{1.29}$$

The hopping parameter at zero quark mass is denoted, κ_{crit}, and the lattice bare quark mass is

$$am = \frac{1}{2}\left(\frac{1}{\kappa} - \frac{1}{\kappa_{\text{crit}}} \right). \tag{1.30}$$

$\mathcal{M}_{W_F}(x,y;U)$ is the Wilson fermion matrix

$$\mathcal{M}_{W_F}(x,y;U) = \delta(x,y) - \kappa \not{D}(x,y;U), \tag{1.31}$$

where the quark fields have been rescaled by a factor $\sqrt{2\kappa}$, and finally, $\not{D}(x,y;U)$

is

$$\not{D}(x,y;U) = \sum_{\mu}\{U_{\mu}(x)(1-\gamma_{\mu})\delta(x+\hat{\mu},y) + U^{\dagger}_{\mu}(x-\hat{\mu})(1+\gamma_{\mu})\delta(x-\hat{\mu},y)\Big\}. \quad (1.32)$$

The term

$$-\frac{r}{2}\sum_{\mu=1}^{d}\overline{\psi}(x)\left[U_{\mu}(x)\psi(x+\hat{\mu}) + U^{\dagger}_{\mu}(x-\hat{\mu})\psi(x-\hat{\mu}) - 2\psi(x)\right], \quad (1.33)$$

is called the Wilson term. The price paid for curing the fermion doubling problem is that this term breaks chiral symmetry. Consequently the fermion mass does not necessarily vanish at $m = 0$. The parameters of the theory must therefore be tuned to their critical values using some criterion. In general, this is that the pion mass vanish in the critical limit.

The Lattice QCD action can now be written

$$S_{QCD}[U] = S_G[U] + S_{W_F}[U]. \quad (1.34)$$

1.1.3 The Sheikholeslami-Wohlert Action

Formulating the theory on a lattice in this way has naturally introduced discretisation errors. The gluonic part of the QCD action, described above, has discretisation errors of $\mathcal{O}(a^2)$, whereas the fermionic part has errors of $\mathcal{O}(a)$. So the first steps in any attempt to reduce these errors are directed towards the fermionic term.

An improvement scheme proposed by Symanzik [11] also uses the non-uniqueness of the action, described in the previous section. $\mathcal{O}(a)$ discretisation effects, in on-shell quantities, are removed by the addition of local, higher-dimensional ("irrelevant") counter-terms to the lattice action and the composite fields of interest. These terms are chosen to cancel the $\mathcal{O}(a)$ cutoff effects. The coefficients of these

terms are not *a priori* known and must be determined (usually through perturbation theory).

This approach was used by Sheikholeslami and Wohlert [13] to write down an $\mathcal{O}(a)$ improved action for Lattice QCD. They showed, by performing field transformations in the functional integral of the theory, that from the possible counter-terms all except one can be neglected or absorbed into a redefinition of the fields. The remaining counter-term, called the "clover" term in the action is

$$-c_{sw}\frac{i\kappa}{2}\sum_{x,\mu,\nu}\overline{\psi}(x)\sigma_{\mu\nu}F_{\mu\nu}(x)\psi(x), \tag{1.35}$$

For $\mathcal{O}(a)$ improvement of matrix elements, the quark fields must also be modified. As shown by Heatlie [15], the replacement (called rotations) of the fields

$$\psi(x) \longrightarrow \left(1-\frac{1}{2}\vec{\not{D}}\right)\psi(x), \tag{1.36}$$

$$\overline{\psi}(x) \longrightarrow \overline{\psi}(x)\left(1+\frac{1}{2}\overleftarrow{\not{D}}\right), \tag{1.37}$$

where $\not{D}$ is the lattice covariant derivative acting on the quark fields

$$\vec{\not{D}}\ \psi(x) = \frac{1}{2}\left\{U_\mu(x)\psi(x+\hat{\mu})-U_\mu^\dagger(x-\hat{\mu})\psi(x-\hat{\mu})\right\}, \tag{1.38}$$

$$\overline{\psi}(x)\ \overleftarrow{\not{D}} = \frac{1}{2}\left\{\overline{\psi}(x+\hat{\mu})U_\mu^\dagger(x)-\overline{\psi}(x-\mu)U_\mu(x-\hat{\mu})\right\}, \tag{1.39}$$

generates the required improvement. The improved QCD action, called the Sheikholeslami-Wohlert (SW) action is

$$S_{SW}[U] = S_G[U]+S_{W_F}[U]-c_{sw}\frac{i\kappa}{2}\sum_{x,\mu,\nu}\overline{\psi}(x)\sigma_{\mu\nu}F_{\mu\nu}(x)\psi(x), \tag{1.40}$$

The coefficient of the clover term, c_{sw} is a function of the bare coupling, g_0. There is a non-perturbative value of this quantity such that $\mathcal{O}(a)$ cutoff effects are cancelled as required. Because the clover term is local, its coefficient is, in general calculated in perturbation theory. However, a recent lattice calculation

indicates that c_{sw} is underestimated in a perturbative approach.

To lowest order Sheikholeslami and Wohlert calculated that $c_{sw} = 1$ [13]. Heatlie *et al.* subsequently showed that the SW-action removes terms of order, $(g_0^{2n} a \log a^n)$, at n^{th} order in perturbation theory [15].

An initial study of the effect of the clover term in the action, using $c_{sw} = 1$, on hadronic observables and matrix elements was done in [14] and substantial improvement was found. In Chapter 2, a mean-field improved SW-action is described. The motivation for this improvement is the lack of agreement between numerical simulations and perturbation theory, even for short distance observables, where they should be compatible. A multiplicative renormalisation of the link operators removes some unphysical contributions to the action which are the cause of the mismatch. This scheme removes some, though not all, discretisation errors of $\mathcal{O}(ag^2)$.

1.2 Numerical Simulation

Having formally defined the Lattice QCD action a practical means of numerically simulating the theory must be developed. The generating functional for Lattice QCD [9] is

$$Z = \int D\overline{\psi} D\psi DU \exp^{-S_G + \overline{\psi}\mathcal{M}(x,y;U)\psi}. \tag{1.41}$$

where $\mathcal{M}(x,y;U)$ is the fermion matrix. DU is constructed from the Haar measure on the $SU(3)$ group. It is defined over every link and $D\overline{\psi}D\psi$ is defined over the Grassmann variables at every site. They are given by,

$$\begin{aligned} DU &= \prod_{x,\mu} dU_\mu(x), \\ D\overline{\psi}D\psi &= \prod_x d\overline{\psi}(x) d\psi(x). \end{aligned} \tag{1.42}$$

In the functional integral of Equation (1.41), the Grassmann-valued quark fields, $\psi(x)$ and $\overline{\psi}(x)$, cannot be evaluated in a stochastic process and must be integrated out before any numerical simulations can be attempted. This creates an effective

action, which depends only on the gauge fields, so the path-integral is

$$Z = \int DU \det \mathcal{M} \exp^{-S_G}[U]. \tag{1.43}$$

The vacuum expectation value of an observable is expressed as

$$\langle \mathcal{O} \rangle = \frac{1}{Z} \int DU \det \mathcal{M} \exp^{-S_G}[U] \mathcal{O}(U). \tag{1.44}$$

Since the action has been rotated to Euclidean time by Equation (1.1) a Monte Carlo algorithm can be used to determine vacuum expectation values, using techniques developed for statistical mechanics.

1.2.1 General Monte Carlo Techniques

Although the lattice reduces the calculation of expectation values to an integration problem, standard numerical algorithms are unsuitable for evaluating the path-integral, for two reasons. Firstly, the number of integration variables in DU is large. Since the majority of lattice calculations, and in particular the work in this thesis, are performed within the "quenched" approximation, I will from now on assume this[1]. In essence, it amounts to assuming

$$\det \mathcal{M} = \text{constant} \quad \equiv \quad 1. \tag{1.45}$$

so that Equation (1.43) becomes

$$Z = \int DU \ \exp^{-S_G}[U]. \tag{1.46}$$

However, even after quenching the theory the number of variables is, $\approx 10^4 - 10^6$. The second disadvantage for standard integration techniques, is the sharp peak in the factor, $\exp^{-S_G[U]}$, about the classical solutions to the field equations. For these reasons Monte Carlo algorithms provide the best way of dealing with simulations of this magnitude, an outline of which is the following:

[1] This is explained in more detail later in this chapter.

A dataset of N gauge field configurations, $\{U_i\}_{i=1...N}$, are generated with "importance sampling" so that only those configurations which contribute most to the path-integral are chosen. In particular, choosing the configurations with probability density, $P \propto \exp^{-S_G[U]}$, the expectation value of an observable, $\mathcal{O}$ is simply written as

$$\langle \mathcal{O}[U] \rangle \sim \frac{1}{N} \sum_{i=1}^{N} \mathcal{O}[U_i]. \tag{1.47}$$

The algorithm which generates these configurations can be thought of as a Markov process, the configurations being elements of the Markov chain. There is however, one extra constraint on the algorithm, which is that it must satisfy detailed balance. This requirement forces the system towards its equilibrium (canonical) configuration with each step of the Markov process. Detailed balance is ensured by choosing the probability, P of moving from configuration C to C', to satisfy

$$P(C' \leftarrow C)P[C] = P(C \leftarrow C')P[C']. \tag{1.48}$$

Perhaps the simplest algorithm, satisfying the criteria of detailed balance and selecting configurations with the required probability is the Metropolis algorithm [22].

1.2.2 The Transfer Matrix

The formal connection between statistical mechanics and quantum mechanics is provided by the transfer matrix. It plays the rôle of a bridge between the linear operators on a Hilbert space of states and probability theory.

For a well-defined quantum theory, the transfer matrix is a bounded, hermitian, positive-definite operator. On a Euclidean lattice with a Wilson gauge action, it links states at time t to their nearest neighbours at $t \pm 1$ so that it is also called the evolution operator. The lattice definition is

$$\mathbf{T} = \exp^{-Ha}, \tag{1.49}$$

where H is the Hamiltonian of the system. The eigenvectors and eigenvalues are

given by

$$\hat{H}|\psi_n\rangle = E_n|\psi_n\rangle \quad ; \quad E_{n+1} > E_n, \tag{1.50}$$

and the lowest eigenvalue is E_0, corresponding to the vacuum state $|0\rangle$. The generating function is

$$Z = \mathrm{Tr}\left(\mathbf{T}^N\right), \tag{1.51}$$

where N is the lattice extent, in Euclidean time.

The mass spectrum of the system can be derived from the eigenvalues of $\mathbf{T}$ by extracting the long-time behaviour of correlation functions built from operators $\mathcal{O}(t)$, and having the quantum numbers of the particle required. For a two point correlation function,

$$\langle \mathcal{O}(t_0)\mathcal{O}(t_1)\rangle \propto \exp^{-(E_1-E_0)|t_1-t_0|}. \tag{1.52}$$

Specifically, the effective mass of a particle can be extracted from the ratio of correlation functions at timeslices, t and $t \pm 1$.

$$\mathcal{F}\left[\frac{\langle \mathcal{O}(0)\mathcal{O}(t)\rangle}{\langle \mathcal{O}(0)\mathcal{O}(t+1)\rangle}\right] = am_{\mathrm{eff}}. \tag{1.53}$$

In §1.4, the function $\mathcal{F}$ is derived for mesons and baryons.

1.3 Gauge-Fixing in Lattice QCD

Considering first of all, the continuum theory, it is well known that the path-integral

$$Z = \int DA_\mu(x)\, \exp^{-S_{\mathrm{YM}}[A]}, \tag{1.54}$$

is problematic. The action is invariant under a gauge transformation

$$A_\mu \longrightarrow A^g_\mu \quad ; \quad A^g_\mu = g(x)A_\mu(x)g^{-1}(x) + g(x)\partial_\mu g^{-1}(x), \tag{1.55}$$

which means that it is constant on the orbit of the gauge-group formed from all A^g_μ, for some A_μ. The integral over the gauge fields, A_μ over-counts the degrees of

freedom, by including all A_μ, even those related by a gauge transformation. This introduces an infinite contribution to the path-integral, which must be factored out to have a meaningful quantisation of the theory.

Faddeev and Popov [20] showed that such a quantisation is possible. Requiring that the path integral does not integrate over all gauge fields connected by a gauge transformation, is in fact requiring that it remain in a definite gauge. A gauge-fixing term is introduced in the path integral which allows the gauge group integration to be factored out. This convergence term does not affect the vacuum expectation values of gauge-invariant quantities.

In Lattice QCD, no gauge-fixing term is required because the link variables (the lattice gauge fields) have only finite range. The gauge group is compact and hence the volume in the path-integral space, generated by all possible gauge transformations, is finite. In principle, therefore, no gauge-fixing term is necessary when calculating physical, gauge-invariant observables, on a lattice. However, the quark and gluon propagators of the theory are gauge-dependent. To study these and other gauge-dependent objects the gauge must be fixed. The popular choice (in the continuum and on the lattice) has been Landau gauge, imposed by the constraint

$$\partial_\mu A^\mu = 0. \tag{1.56}$$

Numerically, this is implemented by minimising the functional

$$F = -\frac{1}{4g^2 V} \sum_{x,\mu} \Re\mathrm{eTr}\left[g(x) U_\mu(x) g^\dagger(x+\hat{\mu})\right]. \tag{1.57}$$

A correct quantisation procedure will restrict the path-integral integration to a "hypersurface", which intersects each orbit only once. Equation (1.56) alone, does not guarantee this, introducing Gribov copies [50]. In Chapter 4, I will report on a preliminary investigation of a new, gauge-fixing algorithm which both avoids the Gribov ambiguity and allows for a study of the gauge dependence of the gluon propagator.

1.4 Two-point Hadron Correlators

Correlation functions for a given particle are constructed from time-ordered products of interpolating field operators ϑ. These operators are created by "tying together" quark propagators, using Dirac gamma matrices with the correct quantum numbers to simulate the particle of interest.

This interpolating field must have a finite overlap with the single particle state in question. In principle, for a field ϑ_h and an hadronic particle state $h(k)$, if

$$\langle 0|\vartheta_h(0)|h(k)\rangle \neq 0, \tag{1.58}$$

then ϑ_h is an interpolating field. However, in practice it is important that the overlap of ϑ_h and the physical particle state be maximised and the coupling to radial excitations be minimised.

For mesons and baryons, generic interpolating fields are, respectively

$$\vartheta_{\mathrm{M}}(x) = \overline{\psi}_\beta(x)\Gamma\psi_\alpha(x), \tag{1.59}$$

$$\vartheta_{\mathrm{B}}(x) = \epsilon_{ijk}\left(\psi^i_\alpha(x)\mathrm{C}\,\Gamma\psi^j_\beta(x)\right)\psi^k_\delta(x), \tag{1.60}$$

α, β, δ are the flavour indices, i, j, k the colour indices, C in Equation (1.60) is the charge conjugation matrix and Γ is one of 16 Dirac gamma matrices. Table 1.1 contains a list of the operators used in this thesis, the corresponding particles and their J^{PC} number. The quark fields, of flavour α, β, δ, are at the same spatial point so inserting gauge fields to maintain gauge invariance is unnecessary.

A two-point correlation function as described above is

$$c(\vec{x}, t) = \langle 0|\mathcal{T}[\vartheta_h(x)\vartheta^\dagger_h(0)]|0\rangle, \tag{1.61}$$

with a time ordering operator, $\mathcal{T}$. The operator at the source, $\vartheta^\dagger_h(0)$, has the appropriate quantum numbers to create the hadron of interest. This is subsequently annihilated at the sink by $\vartheta_h(x)$. To see more clearly the information needed to form such a correlator, consider the mesonic interpolating field in Equation (1.59).

Hadron	J^{PC}	Γ structure
PS	0^{-+}	$\overline{\psi}^{\alpha}\gamma_5\psi^{\alpha}$
V	1^{--}	$\overline{\psi}^{\alpha}\gamma_i\psi^{\alpha}$
A_4	0^{-+}	$\overline{\psi}^{\alpha}\gamma_4\gamma_5\psi^{\alpha}$
A_1	1^{++}	$\overline{\psi}^{\alpha}\gamma_i\gamma_4\psi^{\alpha}$
A_0	0^{++}	$\overline{\psi}^{\alpha}\psi^{\alpha}$
N	$\frac{1}{2}^{+}$	$\epsilon_{\alpha\beta\delta}\left(\psi^{\alpha}C\gamma_5\psi^{\beta}\right)\psi^{\delta}$
		$\epsilon_{\alpha\beta\delta}\left(\psi^{\alpha}C\gamma_4\gamma_5\psi^{\beta}\right)\psi^{\delta}$
Δ	$\frac{3}{2}^{+}$	$\epsilon_{\alpha\beta\delta}\left(\psi^{\alpha}C\gamma_{\mu}\psi^{\beta}\right)\psi^{\delta}$

Table 1.1: The operators used to create hadron states and their corresponding J^{PC}.

Inserting this in Equation (1.61) gives

$$c(\vec{x},t) = \langle 0|\overline{\psi}^i_\alpha(x)\Gamma^{ij}\psi^j_\alpha(x)\overline{\psi}^k_\beta(0)\Gamma^{\dagger kl}\psi^l_\beta(0)|0\rangle. \tag{1.62}$$

The correlator is now Wick contracted to give

$$\begin{aligned} c(\vec{x},t) &= \lim_{N\to\infty} \Gamma^{ij}\Gamma^{\dagger kl}\langle 0|\overline{\psi}^i_\alpha(x)\psi^l_\beta(0)|0\rangle\langle 0|\psi^j_\alpha(x)\overline{\psi}^k_\beta(0)|0\rangle, \\ &= \lim_{N\to\infty} \frac{1}{N}\sum_{n=1}^{N}\left[-\Gamma^{ij}\Gamma^{\dagger kl}Q^{li(n)}_{\beta\alpha}(0,x)Q^{jk(n)}_{\alpha\beta}(x,0)\right]. \end{aligned} \tag{1.63}$$

The hermiticity property of the quark propagator,

$$Q^{li}_{\beta\alpha}(0,x) = \gamma_5^{rs}Q^{\dagger st}_{\beta\alpha}(x,0)\gamma_5^{ti}, \tag{1.64}$$

means the correlator can be written as

$$c(\vec{x},t) = \lim_{N\to\infty} \frac{1}{N}\sum_{n=1}^{N}\mathrm{Tr}\left[Q^{(n)}(x,0)\Gamma^\dagger\gamma_5 Q^{\dagger(n)}(x,0)\gamma_5\Gamma\right], \tag{1.65}$$

with the trace over spin and colour and $Q^{(n)}(x,0)$ is the quark propagator calculated on the n^{th} gauge configuration. So, to calculate a correlator, the quark propagator, $Q(x,0)$ and the operator, Γ are needed. Note that Equation (1.64), when applied to the correlator, means that a quark propagator need only be calculated from the origin to all space-time points, rather than from all points to all points. The same analysis for two-point baryon correlators can be done using the baryon operator of Equation (1.60), but is a little more involved.

The quark propagator, $Q(x,0)$ is obtained by solving an equation of the form

$$\mathcal{M}(x,y;U)Q(x,0) = \eta(x,0). \tag{1.66}$$

which requires the inversion of the fermion matrix, $\mathcal{M}(x,y;U)$. $\eta(x,0)$ is a source function, which can be point-like or spatially extended.

To extract useful information from the correlation function, consider once again

Equation (1.61). For some hadronic particle, m_h a complete set of states is inserted in $c(\vec{x},t)$, with spatial momentum $\vec{p}$, and using translational invariance, so that the correlation function can be written as

$$c(\vec{x},t) = \sum_n \int \frac{d^3\vec{p}}{16\pi^3 E_n(\vec{p})} \langle 0|\vartheta_h(0)|m_h,\vec{p}\rangle\langle m_h,\vec{p}|\vartheta_h^\dagger(0)|0\rangle \exp^{-ip.x}. \tag{1.67}$$

Using this expression, the correlator at momentum, $\vec{q}$ is obtained by weighting the operators with a phase factor $\exp^{-i\vec{q}.\vec{x}}$, such that

$$\begin{aligned} c(\vec{q},t) &= \sum_{\mathbf{x}} c(\vec{x},t)\exp^{-i\vec{q}.\vec{x}}, \\ &= \sum_n \frac{1}{2E_n(\vec{q})} \langle 0|\vartheta_h(0)|m_h,\vec{q}\rangle\langle m_h,\vec{q}|\vartheta_h^\dagger(0)|0\rangle \exp^{iE_n(\vec{q})t}. \end{aligned} \tag{1.68}$$

In a Euclidean theory, with a periodic lattice

$$c(\vec{q},t) = \sum_n \left(A_n(\vec{q})\exp^{-E_n(\vec{q})t} + B_n(\vec{q})\exp^{-E_n^*(\vec{q})(\mathrm{T}-t)}\right), \tag{1.69}$$

with

$$A_n(\vec{q}) = \frac{1}{2E_n(\vec{q})}|\langle 0|\vartheta_h(0)|m_h,\vec{q}\rangle|^2, \tag{1.70}$$

and

$$B_n(\vec{q}) = \frac{1}{2E_n^*(\vec{q})}|\langle 0|\vartheta_h(0)|m_h^*,\vec{q}\rangle|^2. \tag{1.71}$$

The $*$ indicates a backwardly propagating particle. For large times, Equation (1.69) can be approximated as

$$c(\vec{q},t) = \left(A_0(\vec{q})\exp^{-E_0(\vec{q})t} + B_0(\vec{q})\exp^{-E_0^*(\vec{q})(\mathrm{T}-t)}\right). \tag{1.72}$$

In mesons the backwardly and fowardly propagating particles are identical so that the correlation function becomes

$$c(q,t) = 2A_0(\vec{q})\exp^{-E_0(\vec{q})\mathrm{T}/2}\cosh E_0(\vec{q})\left(\frac{\mathrm{T}}{2}-t\right), \tag{1.73}$$

For baryons, however, the backward and forward parts are not the same, baryons having a heavier backwardly propagating parity partner such that $A_0(\vec{q}) \neq B_0(\vec{q})$ and $E_0(\vec{q}) \neq E_0^*(\vec{q})$.

Equations (1.72) and (1.73) imply that as t is increased, contributions to $c(\vec{q}, t)$ from excited states decrease, and the effective mass tends to its ground state value. For both mesons and baryons, the energy (mass) of the lightest state can be extracted from the exponential decay of this state, as described by Equation (1.53) in the previous subsection.

1.4.1 Fuzzing

To improve the overlap of the interpolating field and the ground state of the physical particle, extended sources and sinks have been used [19] in a process called *fuzzing*. At large times, the greatest contamination of the ground state signal for hadronic operators is from the first excited state. The fuzzing prescription maximises the ground state overlap, relative to that of its first excited state. Modified propagators are defined as in [18] with fuzzed links [17] which are created by iteration of

$$U' = \mathcal{P}\left[fU + \sum_{\nu \neq \mu} U_\nu(x) U_\mu(x+\nu) U_\nu^\dagger(x+\mu)\right], \tag{1.74}$$

where f is a link-staple mixing factor and $\mathcal{P}$ is a projection to an $SU(3)$ matrix. A fuzzed propagator is the average of the propagators to the site $(\mathbf{x}, t)$ originating at six points with spatial displacements of $\pm R$ connected by fuzzed links. The summation over all six orientations gives an isotropic spatial dependence so J^{PC} numbers are unaffected. For mesons, such a fuzzed propagator is combined with a local propagator using the relevant Γ matrix to create an operator with the correct quantum numbers. For baryons, three fuzzed propagators are combined in the same way. Using fuzzed propagators is computationally less expensive than standard smearing techniques *e.g.* Jacobi smearing, because once the propagator has been fuzzed the time to generate a correlator is the same as for local propagators. The fuzzing radius R must be tuned so that the ground state signal

is maximised. Unlike smeared data a combination of doubly-fuzzed propagators with the same fuzzing radius cannot be used because the fuzzed links will partially cancel and the data more closely resemble local data.

1.5 Errors : Systematic and Statistical

Although hadronic masses and other observables can now be extracted from the lattice data, an estimation of the associated systematic and statistical errors is essential, for a reliable calculation.

1.5.1 Systematic Errors

The Quenched Approximation

The fermion determinant in Equation (1.43), $\det \mathcal{M}$, is a non-local quantity, coupling every link, U_μ to every other link on the lattice, involving a computationally intensive, lattice-wide calculation. It represents the dynamical effects of internal quark loops (the creation and annihilation of quarks) which phenomenological arguments predict have only small effects on some quantities. It is usual then to set, $\det \mathcal{M} = 1$, in lattice calculations and work within the quenched approximation. Essentially now, the gauge updating is done using the pure gauge action, $S_G[U]$ and the remaining numerical load is in the inversion of the fermion matrix, $\mathcal{M}$. This represents a significant saving in computer time, making large scale computer simulations possible. All work in this thesis is carried out in the quenched approximation. However, an uncontrolled systematic error has been introduced, which may affect different lattice quantities in different ways. This will be discussed further in Chapter 3.

Discretisation Errors due to Non-zero Lattice Spacing

This area has already been touched upon in this chapter. There are two possible approaches to this problem. The first is to do lattice simulations at different values of the lattice spacing and then extrapolate the results to the $a \longrightarrow 0$, continuum limit. The second is the improvement programme, proposed by Symanzik for systematically removing higher order effects from the lattice action.

The Finite Volume

The systematic error due to finite volume effects can be quantified by doing calculations at the same value of the lattice spacing but different physical volumes and comparing the results. All work in this thesis was done at $\beta = 6.2$, at the same lattice size : $(24^3 \times 48)$, making an estimation of the inherent finite volume effects impossible. The most important consideration for light hadron spectroscopy is that the lattice size at which simulations are done is bigger than the pion, the lightest particle of the system. The pion Compton wavelength is ≈ 1.5fm and the lattice used here has a physical size of ≈ 1.68fm : barely bigger than the pion. In practice, however simulations are done at unphysically heavy quark masses, where the pion is smaller, and then extrapolated to the physical regime.

Extracting Fitted Masses

The ratio of correlators for meson and baryon data are fitted to the functions described by Equations (1.72) and (1.73). The choice of minimum timeslice and the time range over which to fit introduces another systematic error. This is explored in some more detail in Chapter 3.

1.5.2 Statistical Errors

Correlations in the data

When a particle described by a correlator, $c(\vec{q}, t)$, as defined in §1.4, propagates through the lattice, there will be correlations between its value on different timeslices. To take this into account, correlators are fitted to exponential functions of Equations (1.72) and (1.73) using a least-χ^2 minimisation algorithm with SVD[2]. To do this, a data covariance matrix is defined as

$$\mathrm{cov}(t_i, t_j) = \frac{1}{N(N-1)} \sum_{n=1}^{N} \left[c^{(n)}(t_i) - \overline{c}\right] \left[c^{(n)}(t_j) - \overline{c}\right], \qquad (1.75)$$

N is the number of configurations in the dataset, $c^{(n)}(t_i)$ is the value of the correlator for configuration, n on timeslice t_i and similarly for $c^{(n)}(t_j)$. $\overline{c}$ is the average value taken over all the configurations.

In general, it proves more reliable to work with a data correlation matrix, $\mathrm{corr}(t_i, t_j)$,

[2]Single Valued Decompostion.

which is more stable, having, $\mathrm{corr}(t_i, t_i) = 1$, and values between $[0, 1]$ on the off-diagonal elements. It is defined as

$$\mathrm{corr}(t_i, t_j) \equiv \frac{\mathrm{cov}(t_i, t_j)}{\sigma(t_i)\sigma(t_j)}, \tag{1.76}$$

where $\sigma(t)$ is the standard deviation. Now, to fit to a function $F(t_i, \vec{a})$, where $\vec{a}$ are the parameters of the fit, the χ^2 function is defined as

$$\chi^2(\vec{a}) = \sum_{t_i, t_j} \delta c(t_i, \vec{a}) \mathrm{corr}^{-1}(t_i, t_j) \delta c(t_j, \vec{a}), \tag{1.77}$$

with

$$\delta c(t_i, \vec{a}) = \frac{1}{\sigma(t_i)} \left[c(t_i) - F(t_i, \vec{a}) \right]. \tag{1.78}$$

$c(t_i)$, is the value of the correlator at time t_i and $F(t_i, \vec{a})$ is the value at the same time of the fit function. This function is minimised until a "best fit" is found. A usual indication that the best fit to the data has been found is a

$$\chi^2/\mathrm{d.o.f.} \sim 1, \tag{1.79}$$

where d.o.f. is the number of degrees of freedom given by

(number of fit points - number of fit parameters).

Bootstrap Error Estimation

Bootstrap resampling is used to estimate the statistical error. For a dataset with N independent and identically distributed datapoints the true dataset, $\mathcal{D}_0$, is used to create any number of synthetic datasets, all with N points, $[\mathcal{D}_1, \mathcal{D}_2 \ldots]$. This is done by drawing points with replacement from the original dataset. Replacement means that each time this is done a slightly different dataset is generated. These new datasets are then used in the fitting routine to obtain a distribution of simulated parameters and an associated statistical error. A confidence level is associated with the bootstrapping procedure. This estimates the certainty that the true parameter values fall within the probability distribution generated by the

bootstrap analysis.

In both, Chapter 2 and 3, the analysis is done using 1000 bootstrap subsamples generated at the 68% confidence level of resampling. In Chapter 4 however, the errors are estimated from a jackknife analysis. Jackknife is similar to a bootstrapping procedure but with one configuration dropped from the average in each sample generated. The variance is defined to be

$$\sigma_{JK} = \left(\frac{N-1}{N} \sum_{i=1}^{N} \left(\overline{x}_i - \langle \overline{x} \rangle \right)^2 \right)^{\frac{1}{2}} \tag{1.80}$$

where

$$\langle \overline{x} \rangle \equiv \sum_{i=1}^{N} \frac{x_i}{N} \tag{1.81}$$

and $\overline{x}_i$ is the sample average of the dataset, deleting the i^{th} point, defined as

$$\overline{x}_i \equiv \frac{1}{N-1} \sum_{j \neq i} x_j \tag{1.82}$$

1.6 From the Lattice to the Continuum

To make realistic predictions using Lattice QCD, it must approach the continuum theory for decreasing lattice spacing. The lattice theory has two parameters: the bare coupling, g_0 and the quark mass, defined by the hopping parameter, κ. The coupling scales with the lattice spacing, so that $g_0 \sim g_0(a)$, and is called the running coupling. That the coupling scales in this way is not unexpected, since if the lattice spacing is made finer the number of sites and links in a given volume will increase. For the physics to stay the same the bare parameters must be tuned with a. Therefore in the continuum limit, $(a \longrightarrow 0)$, one needs a theoretical prediction for the behaviour of $g_0(a)$. The renormalisation group equation prediction is

$$a = \frac{1}{\Lambda} \left(\beta_0 g_0^2 \right)^{-\frac{\beta_1}{2\beta_0^2}} \exp^{-\frac{1}{2\beta_0^2 g_0^2}} \left(1 + \mathcal{O}(g_0^2) \right), \tag{1.83}$$

where Λ is an integration constant with dimensions of mass. The parameters β_0 and β_1 are given by[3]

$$\beta_0 = \frac{11 - \frac{2}{3}N_f}{16\pi^2} \quad \text{and} \quad \beta_1 = \frac{1}{(16\pi^2)^2}\left(102 - \frac{38}{3}N_f\right). \tag{1.84}$$

Individual masses, ma which scale according to Equation (1.83) are said to show asymptotic scaling.

In practice however, the approach to the continuum is computationally expensive: rising like $1/a^6$ in the quenched theory. So, to make contact with the continuum limit, one generally proceeds as follows :

- At a given value of the lattice spacing, data are generated at different quark masses (different κ values). This is done at unphysically heavy quark masses which must then be extrapolated to the critical quark mass at κ_c.
- Using the linear relationship from PCAC

$$m_\pi^2 \propto m_q, \tag{1.85}$$

  and the criterion that $m_\pi^2 = 0$ at the critical point, κ_c is extracted.
- The ρ mass at this critical point is then found by extrapolating to its value at κ_c. This number is compared with its experimental counterpart to set the scale for this particular lattice calculation. In principle, any dimensionful quantity can be used to set the scale but traditionally this has been done using m_ρ.
- Lattice values can now be converted to physical numbers using this scale and compared with experimental results.

Ideally, this procedure is repeated at different lattice spacings so that lattice masses, ma, are calculated for various couplings, $g(a)$. As the continuum is approached, ratios of these masses become independent of $g(a)$ and so they should

[3]Note that when working in the quenched approximation, the number of flavours, N_f, is zero.

remain constant as g is varied, even if the individual masses do not exhibit asymptotic scaling. This property is generally referred to as "scaling". In Chapter 3, data at three couplings is used to test whether scaling is seen for light quarks mass in the range $5.7 \leq \beta \leq 6.2$.

The emphasis in this chapter has been on concepts in Lattice QCD and methods relevant to the following chapters. A more in-depth treatment of lattice gauge theory can be found in the literature [1, 2].

Chapter 2

The effect of $\mathcal{O}(a)$ improvement in quenched QCD

In this chapter the quenched light-hadron spectrum and decay constants are determined at two values of the clover coefficient, c_{sw}. The results are compared, to investigate the effects of mean-field improvement (called tadpole improvement) of the action. With this in mind, a similar dataset was used at both c_{sw} values. Although the evidence of improvement will probably not be as substantial at $\beta = 6.2$ as on a coarser lattice, *e.g.* $\beta = 5.7$, the comparison may nonetheless indicate that as discretisation errors are brought under control, any remaining discrepancy with experiment is due to systematic errors.

Reference is made to a recent paper [28] containing results of a similar analysis at $\beta = 5.7$.

2.1 Tadpole Improvement

The Symanzik [11] improvement programme outlined in Chapter 1 has prompted much work on the reduction of discretisation effects. The SW-action is a first step towards reducing errors due to the lattice spacing in Wilson-like fermionic actions. In this chapter, a mean-field improved action is described, which further reduces the discretisation errors of the fermion action. Highly improved actions are also being investigated which should allow spectrum calculations to be done on coarse lattices [24]. However, this level of improvement requires the addition of terms to both the gluonic and fermionic parts of the action introducing extra perturbative coefficients.

In Chapter 1 the coefficient c_{sw} was introduced, a mean-field improved redefinition of this parameter has been shown [25] to reduce errors to $\mathcal{O}(ag^2)$. In a recent,

non-perturbative calculation of c_{sw} [38], it is claimed that all $\mathcal{O}(ag^{2n})$ errors are removed, leaving errors of $\mathcal{O}(a^2)$. In this thesis, the value of c_{sw} is determined as proposed in [25] and so I will focus on that method.

The motivation for the redefinition of c_{sw} stems from the lack of agreement between calculations in lattice perturbation theory and Monte Carlo simulations [43], even for short distance quantities where both approaches should be reliable. Lepage and Mackenzie have shown that the bare coupling, $\alpha_{\rm lat}$ is a bad expansion parameter for perturbative series. In general, a renormalised coupling should be used, a running coupling, whose value in any expansion depends on the length scales relevant to the process considered. The argument for using $\alpha_{\rm lat}$ is that perturbative quantities in Lattice QCD generally involve length scales of the order of the lattice spacing. Only small renormalisation of the coupling is therefore expected, with respect to the bare value. However, this ignores possible scale-independent renormalisations of $\alpha_{\rm lat}$ and precisely this occurs, making expansions in the bare parameter inaccurate.

The authors have shown that choosing a renormalised coupling brings perturbation theory into much better agreement with non-perturbative simulations [25].

The origin of the mismatch between the lattice coupling and its continuum analogue is in the non-linear mapping between the lattice link operator and the continuum gauge fields. Recall the expression for the link variable is

$$U_\mu(x) = \exp^{iagA_\mu(x)} \sim 1 + iagA_\mu(x). \tag{2.1}$$

Higher order terms in this expansion contain additional factors of agA_μ which, if the A_μ are contracted, generate UV divergences exactly cancelling the additional powers of a and leaving terms suppressed only by powers of the coupling g^2. These "tadpole" terms can be large, affecting the results of a lattice calculation. Going back to Equation (2.1), in the continuum $(1 + iagA_\mu(x))$ has an expectation value of 1 but in lattice theory, tadpole renormalisation of $U_\mu(x)$ means this expectation value is less than 1. The discrepancy suggests the following modification to

Equation (2.1)

$$U_\mu(x) = u_0 \left(1 + iagA_\mu(x)\right), \tag{2.2}$$

where u_0, is the mean value of the link variable, and has a value < 1.

The renormalised coupling, g, is commonly referred to as the boosted coupling and is given by

$$g = \frac{2N_c}{\beta u_0^4}. \tag{2.3}$$

In the SW-action, the redefinition of $U_\mu(x)$ results in the replacements

$$c_{sw} = \frac{\tilde{c}}{u_0^3}, \tag{2.4}$$

$$\kappa = \frac{\tilde{\kappa}}{u_0}. \tag{2.5}$$

The tree-level estimate [15], $\tilde{c} = 1$, is used. The hopping parameter at zero quark mass, $\tilde{\kappa}_c$, is expected to be close to its tree-level value of $1/8$.

There is some ambiguity in the value of u_0, since in principle, any short distance quantity can be used. A gauge-invariant defintion of u_0 is

$$u_0 = \left\langle \frac{1}{3} \mathrm{Tr} U_{\mathrm{plaq}} \right\rangle^{\frac{1}{4}}. \tag{2.6}$$

and this expression is used in the simulations described in this thesis. At $\beta = 6.2$, its value is 0.88506. A one-loop determination and a two-loop estimation of c_{sw} by Naik [41] agree well with the mean-field value above, which inspires confidence in numerical simulations using these parameters.

2.2 Simulation Details

The comparison was carried out at $\beta = 6.2$, on a $24^3 \times 48$ lattice using 60 gauge field configurations and two values of the clover coefficient : the tree-level value, $c_{sw} = 1.0$ and the mean-field improved value, $c_{sw} = 1.4424$. The configurations were generated with a hybrid over-relaxed algorithm using the gluonic action defined in Equation (1.23). Gauge field configurations at $c_{sw} = 1.0$ were generated on a 64-node Meiko *i*860 Computing Surface using the SW-action defined in Chapter 1 and

generation of the tadpole-improved dataset was done on a Cray T3D at Edinburgh. Propagators were calculated at three values of the hopping parameter, using both local and fuzzed sources and sinks for the tadpole-improved dataset and purely local sources and sinks for the $c_{sw} = 1$ case. Three datasets at varying levels of improvement can then be considered : $c_{sw} = 1$ with local data; $c_{sw} > 1$ with local data and $c_{sw} > 1$ with fuzzed data. All quark propagators were calculated using a minimal residual algorithm. The propagators in the SW-action are rotated, see Equations (1.36) and (1.37), whereas for the tadpole-improved case they are unrotated.

The lattice details are shown in Table 2.1.

c_{sw}	κ_1, κ_2, κ_3	Fuzzing
1.0	0.14144, 0.14226, 0.14262	LL
1.4424	0.13640, 0.13710, 0.13745	LL, LF, FL, FF

Table 2.1: Lattice details for the comparison on 60 gauge field configurations. The fuzzing notation LL, FL etc. refers to the source and sink respectively *e.g.* LL means local sources and sinks whereas FL means a fuzzed source and local sink.

2.3 Fitted Masses

Using the quark propagators, two-point correlation functions are constructed as described in Chapter 1. For mesons, both degenerate and non-degenerate quark masses are used. A least-χ^2 fit of the zero-momentum, time-sliced, meson correlators to a single hyperbolic cos function is done. Degenerate baryons only are constructed and the zero-momentum, time-sliced correlators are fitted to a single exponential.

For both mesons and baryons, sliding window fits are used to choose the optimal fitting ranges. The χ^2/d.o.f. and Q[1] are measured for a range of $t_{\rm min}$ and $t_{\rm max}$. The

[1] Q is a measure of the probability of achieving a good χ^2. It has bounds $Q(a,0) = 1, Q(a,\infty) = 0$ and is given by,

$$Q(\text{d.o.f.}/2, \chi^2/2) \equiv 1 - \frac{1}{\Gamma(\text{a})} \int_{\text{x}}^{\infty} \exp^{-\text{t}}\, \text{t}^{\text{a}-1} \text{dt}, \quad \text{a} > 0. \tag{2.7}$$

stability of the ground-state mass as the fitting range is varied is also monitored. For the local data at both $c_{sw} = 1$ and $c_{sw} > 1$ the optimal fitting ranges are the same as those used in [23]. The pseudoscalar is fitted using time-slices $14-22$ and the vector meson using time-slices $13-23$ for all but the heaviest κ combination, where the time range was $15-23$. The nucleon is fitted using $16-22$ and the Δ, using $16-21$.

For the $c_{sw} > 1$ fuzzed data, the onset of the plateau is earlier than in the local case, as expected. In general, it is possible to fit over ten time-slices. However, the vector meson has a characteristic "wiggle" which is not cured by fuzzing. In particular, the lightest κ-values cannot be reliably fitted to greater than time-slice 21 as the data become extremely noisy at higher time-slices. The fitting range is reduced accordingly to $12-20$ for these quark masses. To ensure that the correct ground state is extracted, a double exponential fit to the data is done. This is shown in Figure 2.1, where clearly the two fitted masses agree.

The fuzzed baryon data allows the fitting range to be pushed back to $13-22$ and $14-22$ for the nucleon and delta respectively, as compared with $16-22$ and $16-21$ for $c_{sw} = 1$. Once again, however, the plateau for the lightest κ combinations only extends to time-slice 21. This deterioration of the plateau may be a signal that the fuzzing radius is not optimal. Although the plateau becomes noisy at $t \geq 21$ for $c_{sw} > 1$, using a fuzzed source has allowed the fitting range to be extended. The effective masses of the pion, vector meson, nucleon and Δ for the lightest quark can be seen in Figure 2.2 and 2.3.

In Chapter 3, where much higher statistics are used, multi-exponential fits are used to investigate the effect of higher excited states on the data, but for this comparison single exponentials were found to be sufficient.

The effective mass plots for the heaviest κ combinations are shown in Figure 2.4.

Tables 2.2 to 2.5 contain the estimates of the ground state masses for the pseu-

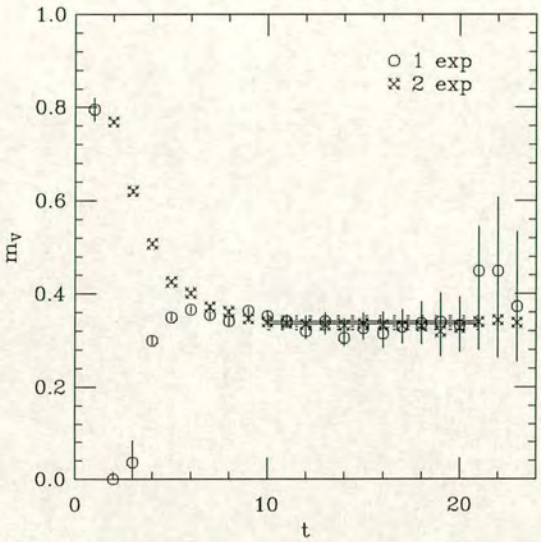

Figure 2.1: The effective mass of the vector meson, for $\kappa = 0.13745$.

doscalar, vector meson, nucleon and delta for all κ combinations. The χ^2/d.o.f. and the value of Q are also given. The fuzzed meson and baryon data lie between the $c_{sw} = 1$ and the $c_{sw} > 1$ local data. This appears to indicate that there are substantial excited state contributions to the local $c_{sw} > 1$ data, but this should become clearer in Chapter 3 when higher statistics are used with fuzzed data.

2.4 The Edinburgh Plot

The Edinburgh plot, is a useful method of presenting baryon data since it is a dimensionless ratio of observables which does not require an extrapolation. This plot is shown in Figure 2.5 for both values of the clover coefficient. There is no change in the ratio of the baryon masses on going from $c_{sw} = 1$ to $c_{sw} > 1$, except for a small effect at the lightest κ value. In [28], at $\beta = 5.7$, a sizeable effect is seen as the clover coefficient is changed : the ratio decreases towards the phenomenological curve, for increasing c_{sw}. This is reasonable as a greater effect is expected at coarser lattice spacings. The $\beta = 6.2$ baryon data is also subject to systematic errors (particularly, to contamination from higher excited states)

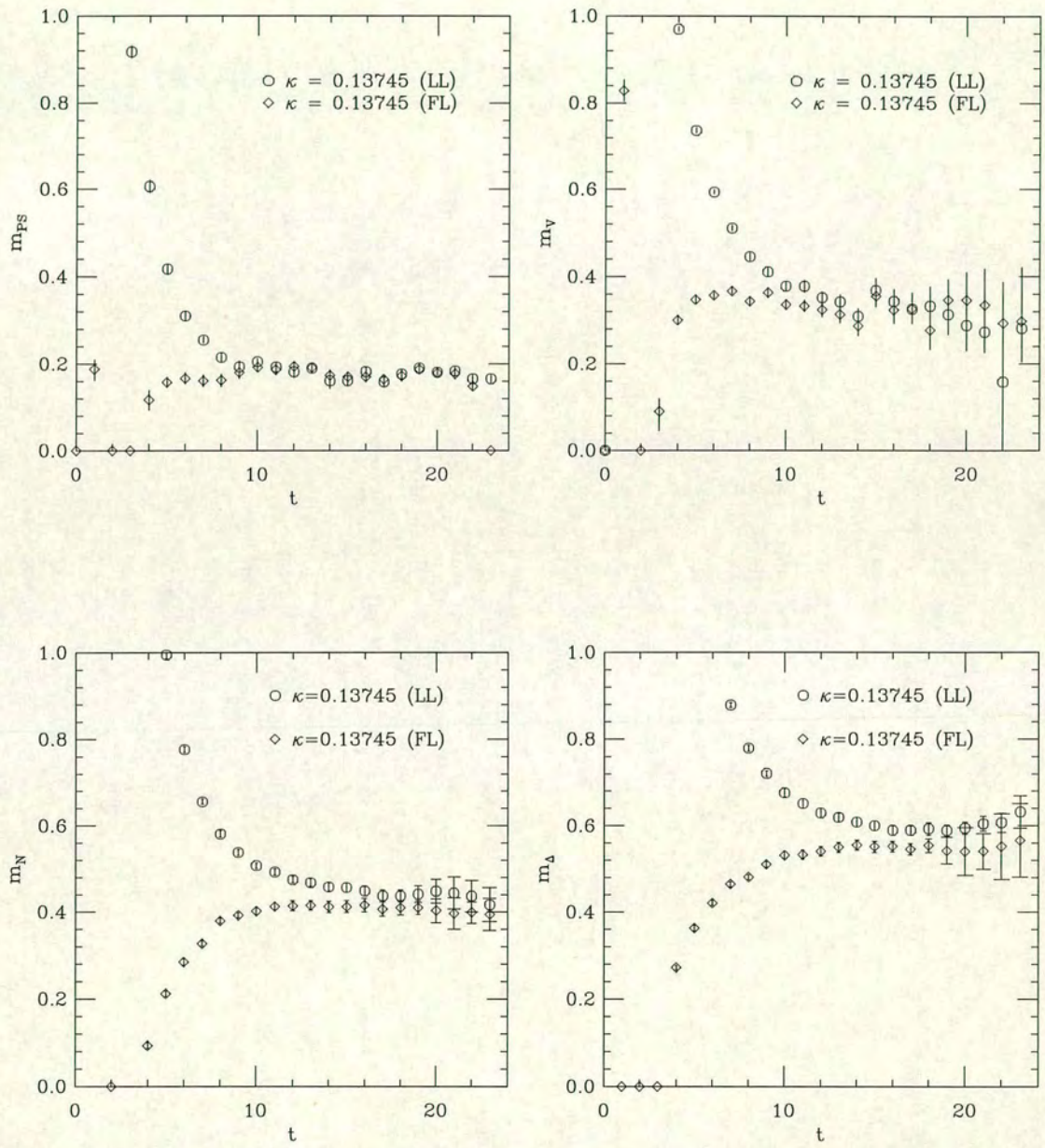

Figure 2.2: Effective mass plots for pseudoscalar, vector, nucleon and Δ for the lightest quark mass simulated *i.e.* $\kappa = 0.13745$. A comparison is not made here with the fits at $\kappa = 0.14262$ (the lightest $c_{sw} = 1$ quark mass) since these κ values were not matched and cannot be expected to have similar masses.

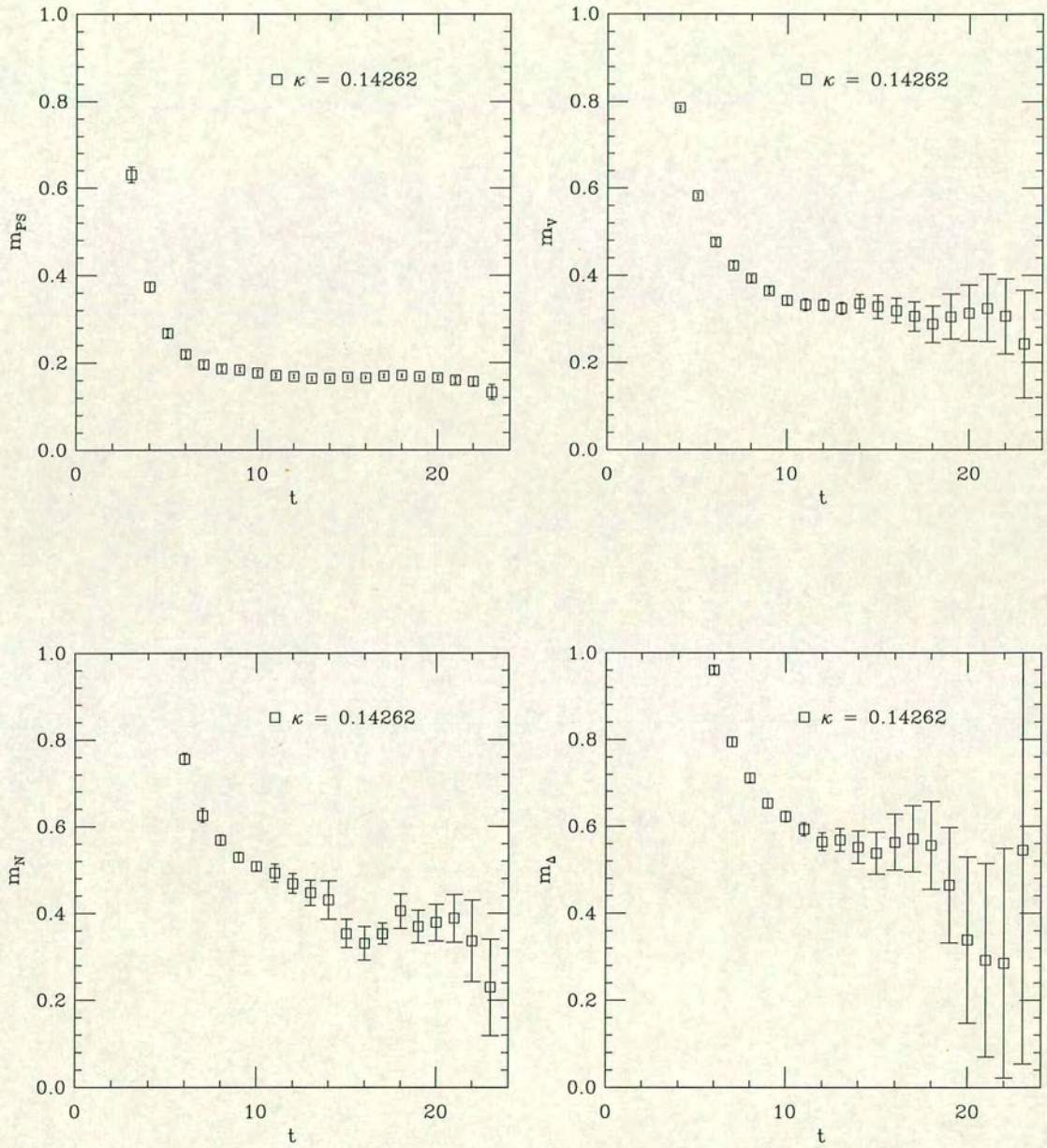

Figure 2.3: Effective mass plots for pseudoscalar, vector, nucleon and Δ for the lightest quark mass simulated, at $\kappa = 0.14262$ at $c_{sw} = 1$.

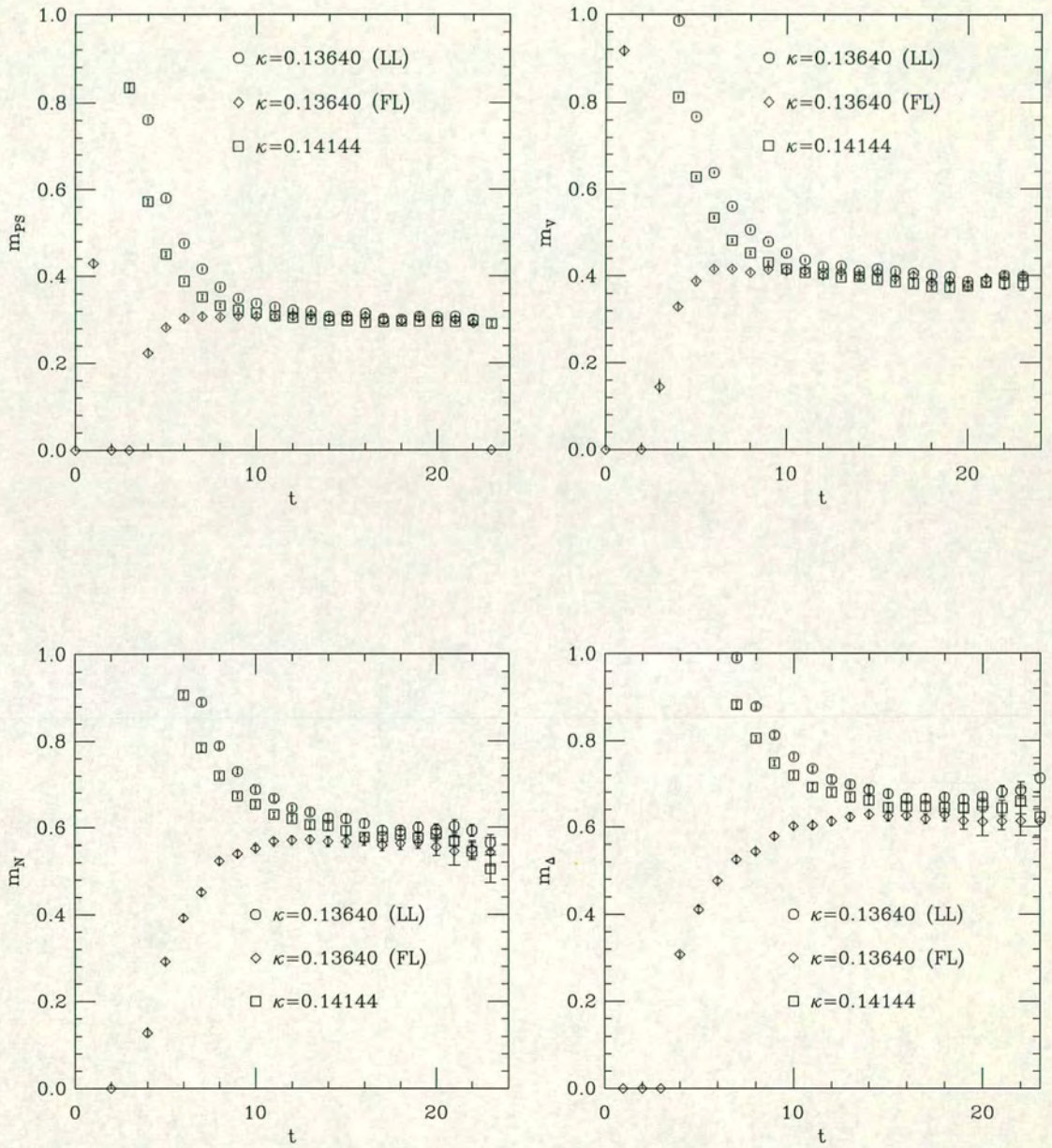

Figure 2.4: Effective mass plots for pseudoscalar, vector, nucleon and Δ for the heaviest quark mass simulated, at $\kappa = 0.13640$ for $c_{sw} > 1$ and $\kappa = 0.14144$ at $c_{sw} = 1$.

c_{sw}	κ_1, κ_2	Fuzzing	m_{PS}	Fit Range	χ^2/d.o.f.	Q
1.0	0.14144, 0.14144	(LL, LL)	$0.298^{+\ 2}_{-\ 2}$	14–22	1.2	0.474
	0.14226, 0.14144	(LL, LL)	$0.259^{+\ 2}_{-\ 2}$	14–22	0.91	0.326
	0.14226, 0.14226	(LL, LL)	$0.214^{+\ 2}_{-\ 3}$	14–22	0.99	0.121
	0.14262, 0.14144	(LL, LL)	$0.241^{+\ 2}_{-\ 3}$	14–22	0.76	0.233
	0.14262, 0.14226	(LL, LL)	$0.192^{+\ 3}_{-\ 3}$	14–22	0.99	0.283
	0.14262, 0.14262	(LL, LL)	$0.167^{+\ 3}_{-\ 4}$	14–22	1.03	0.197
1.4424	0.13640, 0.13640	(LL, LL)	$0.308^{+\ 2}_{-\ 2}$	14–22	1.6	0.611
		(LL, FL)	$0.303^{+\ 1}_{-\ 2}$	12–22	1.4	0.604
	0.13710, 0.13640	(LL, LL)	$0.270^{+\ 2}_{-\ 2}$	14–22	1.3	0.657
		(LL, FL)	$0.265^{+\ 2}_{-\ 3}$	12–22	1.5	0.759
	0.13710, 0.13710	(LL, LL)	$0.226^{+\ 2}_{-\ 2}$	14–22	1.3	0.575
		(LL, FL)	$0.223^{+\ 2}_{-\ 3}$	12–22	1.8	0.870
	0.13745, 0.13640	(LL, LL)	$0.249^{+\ 3}_{-\ 3}$	14–22	1.2	0.503
		(LL, FL)	$0.244^{+\ 3}_{-\ 3}$	12–22	1.5	0.818
	0.13745, 0.13710	(LL, LL)	$0.202^{+\ 3}_{-\ 3}$	14–22	1.4	0.488
		(LL, FL)	$0.199^{+\ 3}_{-\ 4}$	12–22	1.2	0.908
	0.13745, 0.13640	(LL, LL)	$0.175^{+\ 3}_{-\ 3}$	14–22	1.7	0.912
		(LL, FL)	$0.173^{+\ 4}_{-\ 4}$	12–22	1.3	0.937

Table 2.2: Pseudoscalar masses for all κ combinations and two values of c_{sw}.

c_{sw}	κ_1	Fuzzing	m_Δ	Fit Range	χ^2/d.o.f.	Q
1.0	0.14144	(LL,LL)	0.646^{+10}_{-10}	16–21	0.18	0.412
	0.14226	(LL,LL)	$0.579^{+10}_{-\ 9}$	16–21	0.28	0.444
	0.14262	(LL,LL)	0.556^{+66}_{-46}	16–21	0.43	0.399
1.4424	0.13640	(LL,LL)	0.666^{+10}_{-11}	16–21	0.32	0.455
		(LL,FL)	$0.644^{+\ 9}_{-\ 9}$	16–21	0.41	0.573
	0.13710	(LL,LL)	0.612^{+12}_{-13}	16–21	0.24	0.365
		(LL,FL)	0.582^{+12}_{-13}	16–21	0.22	0.474
	0.13745	(LL,LL)	0.591^{+14}_{-13}	16–21	0.31	0.277
		(LL,FL)	0.569^{+12}_{-13}	16–21	0.45	0.365

Table 2.3: Δ masses for degenerate κ combinations, at both values of c_{sw}.

c_{sw}	κ_1, κ_2	Fuzzing	m_V	Fit Range	χ^2/d.o.f.	Q
1.0	0.14144, 0.14144	(LL,LL)	$0.389^{+\ 7}_{-\ 6}$	15–23	1.9	0.802
	0.14226, 0.14144	(LL,LL)	$0.370^{+\ 6}_{-\ 5}$	13–23	1.3	0.913
	0.14226, 0.14226	(LL,LL)	$0.343^{+\ 9}_{-\ 7}$	13–23	0.87	0.882
	0.14262, 0.14144	(LL,LL)	$0.360^{+\ 8}_{-\ 9}$	13–23	1.0	0.967
	0.14262, 0.14226	(LL,LL)	0.331^{+11}_{-10}	13–23	0.6	0.821
	0.14262, 0.14262	(LL,LL)	0.319^{+14}_{-13}	13–23	0.4	0.895
1.4424	0.13640, 0.13640	(LL,LL)	$0.404^{+\ 5}_{-\ 5}$	15–23	1.2	0.666
		(LL,FL)	$0.400^{+\ 5}_{-\ 5}$	12–21	1.2	0.961
	0.13710, 0.13640	(LL,LL)	$0.385^{+\ 5}_{-\ 5}$	13–23	0.94	0.776
		(LL,FL)	$0.381^{+\ 5}_{-\ 6}$	12–21	1.7	0.973
	0.13710, 0.13710	(LL,LL)	$0.361^{+\ 7}_{-\ 7}$	13–23	0.62	0.887
		(LL,FL)	$0.346^{+\ 6}_{-\ 8}$	12–21	1.7	0.899
	0.13745, 0.13640	(LL,LL)	$0.376^{+\ 7}_{-\ 7}$	13–23	0.867	0.810
	0.13745, 0.13640	(LL,FL)	$0.366^{+\ 7}_{-\ 7}$	12–20	0.75	0.976
	0.13745, 0.13710	(LL,LL)	$0.352^{+\ 8}_{-\ 9}$	12–20	0.588	0.823
		(LL,FL)	$0.339^{+\ 7}_{-\ 8}$	12–20	0.86	0.856
	0.13745, 0.13745	(LL,LL)	0.341^{+11}_{-11}	12–20	0.44	0.794
		(LL,FL)	$0.328^{+\ 8}_{-\ 8}$	12–20	0.64	0.898

Table 2.4: Vector meson masses, for degenerate and non-degenerate κ combinations.

c_{sw}	κ_1	Fuzzing	m_N	Fit Range	χ^2/d.o.f.	Q
1.0	0.14144	(LL,LL)	$0.573^{+15}_{-\ 6}$	16–22	1.1	0.51
	0.14226	(LL,LL)	0.462^{+21}_{-14}	16–22	1.2	0.55
	0.14262	(LL,LL)	0.372^{+24}_{-16}	16–22	0.64	0.76
1.4424	0.13640	(LL,LL)	0.588^{+10}_{-19}	16–22	1.2	0.367
		(LL,FL)	0.589^{+11}_{-11}	12–21	1.2	0.389
	0.13710	(LL,LL)	0.486^{+18}_{-18}	16–22	1.3	0.229
		(LL,FL)	0.501^{+15}_{-17}	12–21	1.4	0.262
	0.13745	(LL,LL)	0.434^{+18}_{-18}	16–22	1.3	0.324
		(LL,FL)	0.428^{+15}_{-17}	12–21	1.5	0.259

Table 2.5: Nucleon masses of degenerate κ combinations at both $c_{sw} = 1$ and $c_{sw} > 1$.

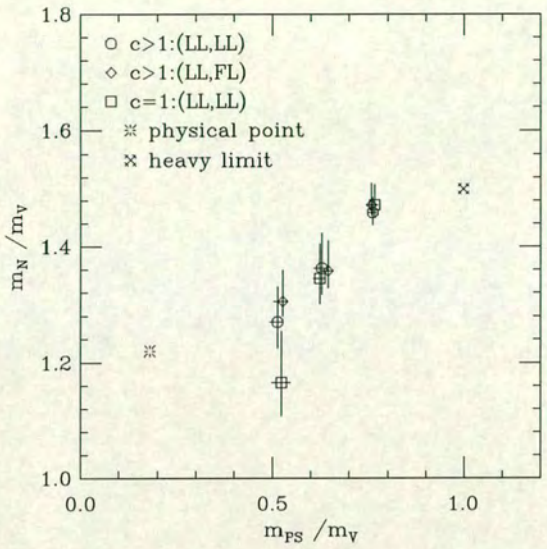

Figure 2.5: Edinburgh Plot for baryon data

because the statistics are low and the data are local. In Chapter 3, the Edinburgh plot is presented with higher statistics and fuzzed data.

2.5 Comparing Extrapolated and Interpolated Hadron Masses

To extract estimates of physical meson masses from the lattice light-light data, $m_{\rm PS}^2$ was extrapolated to the chiral limit where it is assumed to have zero mass. κ_c is the hopping parameter for zero quark mass.

The following assumptions are also made about the functions to fit to: that the pseudoscalar meson mass obeys the PCAC relation, $m_{\rm PS}^2 \propto m_q$, and can be fitted to the form

$$m_{\rm PS}^2(\kappa_1, \kappa_2) = b_{\rm PS}\left(\frac{1}{\kappa_{\rm eff}} - \frac{1}{\kappa_c}\right), \tag{2.8}$$

where $\kappa_{\rm eff}$ is the effective hopping parameter, given by

$$\frac{1}{\kappa_{\rm eff}} = \frac{1}{2}\left(\frac{1}{\kappa_1} + \frac{1}{\kappa_2}\right). \tag{2.9}$$

The second assumption is that the vector meson mass is linear in m_q and can be fitted to

$$m_V(\kappa_1, \kappa_2) = a_V + b_V \left(\frac{1}{\kappa_{\text{eff}}} - \frac{1}{\kappa_c} \right). \tag{2.10}$$

Similarly for the baryons, assuming a linear dependence on quark mass, the following expression is used in both the nucleon and Δ extrapolations

$$m_B = a_B + b_B \left(\frac{1}{\kappa_{\text{eff}}} - \frac{1}{\kappa_c} \right). \tag{2.11}$$

2.5.1 Pseudoscalar Mass

Linear extrapolations in the pseudoscalar mass to find κ_c, have an acceptable χ^2/d.o.f. for all values of c_{sw}. This indicates that a linear fit to the data is reasonable and the issue of curvature is not addressed here. The $c_{sw} > 1$, fuzzed data has the lowest χ^2/d.o.f., implying that this is the most accurate fit to the data. By eye however, and on comparing the values in Table 2.6 there is little difference between the values of κ_c at $c_{sw} > 1$. The final values of κ_c are in Table 2.6 and Figure 2.6 shows a linear fit to the data. At tree-level the critical hopping param-

c_{sw}	Fuzzing	$\tilde{\kappa}_c$	χ^2/d.o.f.
1.0	(LL,LL)	$0.143166 \pm \frac{20}{21}$	2.4
1.4424	(LL,LL)	$0.122083 \pm \frac{30}{28}$	3.0
1.4424	(LL,FL)	$0.122078 \pm \frac{27}{24}$	1.7

Table 2.6: $\tilde{\kappa}_c$ for both values of the clover coefficient. The quoted error is statistical.

eter, $\kappa_c = 1/8$. Historically, using non-tadpole-improved actions, the values of κ_c have been in very poor agreement with this prediction. In Table 2.6 the tadpole-improved κ_c is clearly in much better agreement with the tree-level prediction. This improvement is repeated at coarser lattices [28]. A one-loop calculation in boosted lattice perturbation theory [29] gives a value of $\tilde{\kappa}_c = 0.12215(5)$. The perturbative and non-perturbative $\tilde{\kappa}_c$ are in excellent agreement and close to the

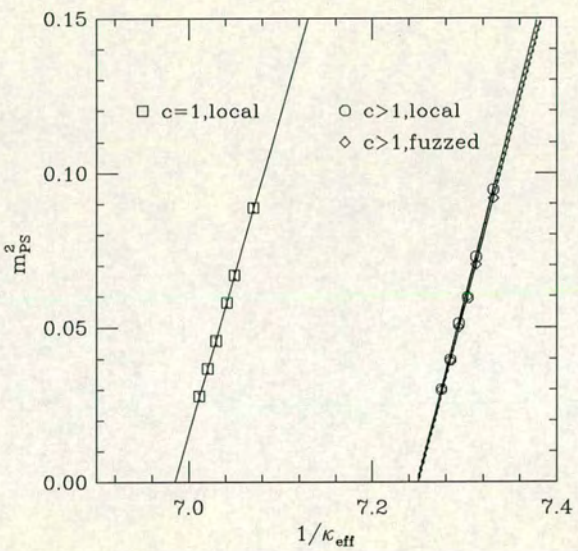

Figure 2.6: Linear extrapolations of m^2_{PS} in effective quark mass for $c_{sw} = 1$ and $c_{sw} > 1$ data. The unrenormalised values of κ_c are : $0.143166, 0.137937, 0.137932$ for the $c_{sw} = 1$, $c_{sw} > 1$ local and fuzzed respectively.

tree-level value. This trend is also seen at $\beta = 6.0$ and $\beta = 5.7$ [39].

2.5.2 Vector Mass

Extrapolations of the vector meson mass to κ_c using Equation (2.10) have an acceptable χ^2/d.o.f. for all cases, so that linear fits are judged to be reliable. The results of the fit are in Table 2.7. The scale, as set by m_ρ, varies significantly due to the difference in the extrapolated vector meson mass at different c_{sw}. The details are in Table 2.7. For $c_{sw} = 1$ and fuzzed $c_{sw} > 1$ data, the values agree with the value from the string tension of $a^{-1} = 2.73(5)$GeV which tends to increase confidence in the corresponding extrapolated ρ masses.

c_{sw}	Fuzzing	am_ρ	χ^2/d.o.f.	a^{-1} [GeV]
1.0	(LL,LL)	0.291^{+12}_{-12}	3.6	2.66^{+12}_{-12}
1.4424	(LL,LL)	0.306^{+15}_{-16}	1.0	2.52^{+13}_{-13}
1.4424	(LL,FL)	0.296^{+15}_{-15}	0.1	2.61^{+13}_{-13}

Table 2.7: Chirally extrapolated results for the vector meson from a linear fit, the errors are statistical.

2.5.3 Interpolation to Strange : κ_s and J.

The hopping parameter at the strange quark mass is determined by fitting to $m^2_{PS}(\kappa_1, \kappa_2)/m^2_\rho$, taking κ_1 to κ_c and using κ_2 to match to the experimental ratio[2] $M^2_K/M^2_\rho = 0.413$. There is evidence that the strange quark mass cannot be consistently determined but rather depends on the experimental ratio chosen to define it [27, 39]. This will be investigated in Chapter 3 for the range of possible experimental ratios. In this chapter the concern is c_{sw} dependence and κ_s is calculated as described above.

The motivation for the introduction of the parameter, J is that it allows a comparison of lattice spectrum results with experimental data, without an extrapolation

[2]I use the convention that masses denoted with "M" refer to experimental values and those denoted by "m" are the lattice values.

to the chiral limit. It is defined as [40]

$$J = m_v \frac{dm_V}{dm_{\rm PS}^2}, \tag{2.12}$$

where the mass, m_v is set using the experimental ratio[3]

$$\frac{M_{K^*}}{M_K} = 1.8. \tag{2.13}$$

Little change is found in J for varying c_{sw}, in fact all values are within errors and in disagreement with the number derived from experimental data. Values of J and κ_s are in Table 2.8.

	$c_{sw} = 1.0$	$c_{sw} > 1.0$	
	(LL,LL)	(LL,LL)	(LL,FL)
$\tilde{\kappa}_s$	0.14190^{+10}_{-10}	$0.122104^{+\ 9}_{-\ 9}$	$0.12153^{+\ 7}_{-\ 7}$
J	0.393^{+12}_{-13}	0.375^{+11}_{-10}	0.391^{+12}_{-12}

Table 2.8: Values of the hopping parameter at the strange quark mass and the parameter J.

2.5.4 Baryon Extrapolations

The nucleon and Δ were extrapolated to the chiral limit using Equation (2.11). These extrapolations are shown in Figure 2.7. The χ^2/d.o.f. for the $c_{sw} = 1$ nucleon data is 5.0 with $Q = 0.024$ which implies a poor fit. For both the local and fuzzed $c_{sw} > 1$ cases the χ^2/d.o.f. is lower : 3.1 and 1.94 respectively. In [23] it was noted that a linear fit to m_N^2 gives a better χ^2/d.o.f.. However, there is no theoretical justification for this choice so only a linear fit to m_N is considered here.

The Δ extrapolation seems to be more reliable at $c_{sw} = 1$, although the errors are larger. A linear fit to Equation (2.11) includes the three points in the three different cases considered here. For $c_{sw} = 1$ the χ^2/d.o.f. is 0.1 and $Q = 0.76$. A

[3]The effect on J, of choosing a different reference quark mass is explored in Chapter 3.

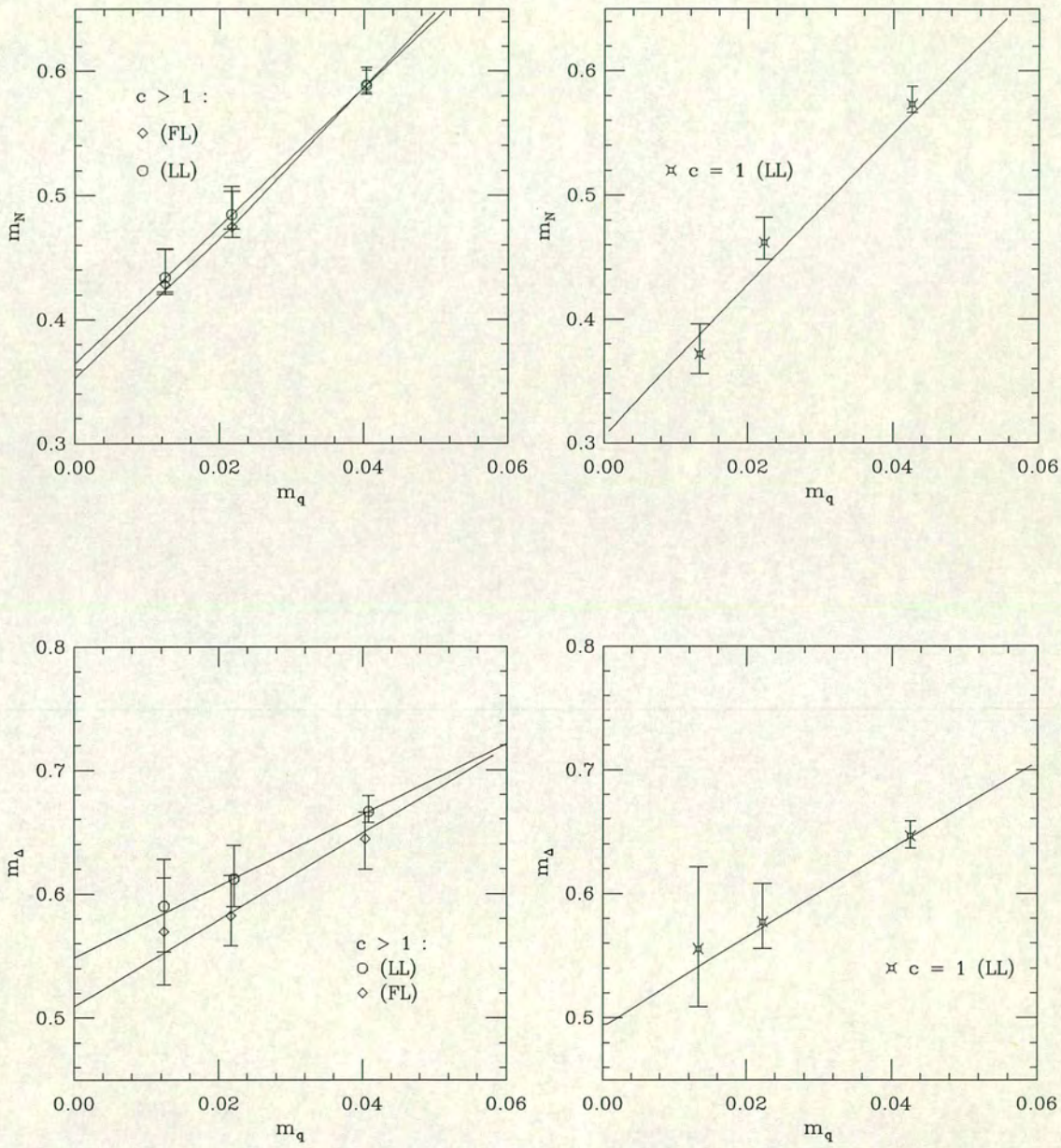

Figure 2.7: Nucleon and Δ extrapolations for the case $c_{sw} = 1$ and $c_{sw} > 1$.

similar analysis of the tadpole-improved datasets gives the local and fuzzed data a χ^2/d.o.f. of ≈ 0.25 and 0.32 respectively. The extrapolation with fuzzed data does give a lower Δ mass, but when converted to physical units the numbers agree within errors. The values of the nucleon and the Δ at κ_c are in Table 2.9. Also included is the interpolated value of the Ω which has $J^{\mathrm{P}} = \frac{3}{2}^+$, the same as the Δ.

Mass	$c_{sw} = 1.0$	$c_{sw} > 1.0$	
	(LL,LL)	(LL,LL)	(LL,FL)
m_N	0.310^{+30}_{-20}	0.364^{+30}_{-28}	0.352^{+26}_{-24}
m_Δ	0.495^{+40}_{-39}	0.547^{+45}_{-41}	0.509^{+34}_{-36}
m_Ω	0.620^{+20}_{-20}	0.644^{+20}_{-20}	0.623^{+19}_{-19}

Table 2.9: Chirally extrapolated and interpolated baryon masses.

2.6 Comparison with Experiment

The chirally interpolated and extrapolated results for strange and non-strange mesons and baryons are compared with the corresponding experimental values in Table 2.10. The scale is set from m_ρ. The physical numbers determined from the

Mass	$c_{sw} = 1.0$	$c_{sw} > 1.0$		Expt
	(LL,LL) (MeV)	(LL,LL) (MeV)	(LL,FL) (MeV)	(MeV)
m_{K^*}	$867^{+\ 9}_{-\ 8}$	$861^{+\ 8}_{-\ 8}$	880^{+10}_{-10}	892
m_ϕ	968^{+21}_{-10}	$968^{+10}_{-\ 9}$	994^{+19}_{-17}	1020
m_η	668^{+12}_{-11}	711^{+15}_{-14}	726^{+15}_{-15}	"686"
m_N	825^{+80}_{-60}	917^{+76}_{-71}	918^{+68}_{-63}	938
m_Δ	1317^{+106}_{-104}	1353^{+113}_{-112}	1328^{+89}_{-91}	1232
m_Ω	1649^{+53}_{-53}	1623^{+50}_{-50}	1626^{+46}_{-46}	1672

Table 2.10: Light-hadron masses in physical units, and compared with the experimental values

fuzzed tadpole-improved dataset agree most closely with the experimental values,

except for the mass of the Δ which is over-estimated, but this is true for all values of c_{sw} : the results are within errors and higher than the experimental value.

2.7 The Hyperfine Splitting

Heavy quark effective theory (HQET) predicts that the (vector meson mass)^2 − (pseudoscalar mass)^2 splitting is approximately constant for heavy-light systems. This has been verified by experiment: $m^2_{B^*} - m^2_B \approx 0.49\,\mathrm{GeV}^2$ and $m^2_{D^*} - m^2_D \approx 0.53\,\mathrm{GeV}^2$. Experimental data for light-light systems suggests that this trend is continued for light quark masses with $m^2_{K^*} - m^2_K \approx 0.55\,\mathrm{GeV}^2$ and $m^2_\rho - m^2_\pi = 0.57\,\mathrm{GeV}^2$. Non-perturbative calculations of the hyperfine splitting for the light quark sector have failed noticeably to reproduce this effect.

Hyperfine splitting in HQET is proportional to the chromo-magnetic coupling between the gluon field and the heavy quark *i.e.*

$$\propto \langle\, \overline{Q}\sigma_{\mu\nu}F^{\mu\nu}Q\,\rangle, \tag{2.14}$$

and to leading order in a this is the "clover term". Hence an improvement in mass splitting, for heavy quark systems is to be expected, on going from the Wilson ($c_{sw} = 0$) action to the SW-action ($c_{sw} = 1$) and similarly, increasing the value of the clover coefficient (tadpole improving) might be expected to increase the effect of this term. Although an equivalent statement cannot be made for light quarks it is at least plausible to expect some level of improvement.

Figure 2.8 shows the hyperfine splitting in lattice units for all c_{sw} values. It is clear that there is no improvement on increasing the value of the clover coefficient. There is no statistically significant difference between the slopes of the $c_{sw} = 1$ and the tadpole data. Both will disagree with experimental results from heavy-light physics, if the trend of decreasing $m^2_V - m^2_{PS}$ with increasing quark mass is continued into the charmonium sector.

With this lack of improvement in mind, two points are investigated. Firstly, it is possible to examine further the c_{sw} dependence of the vector-pseudoscalar mass splitting using an existing UKQCD dataset at $\beta = 6.2$. This was used in [42] to

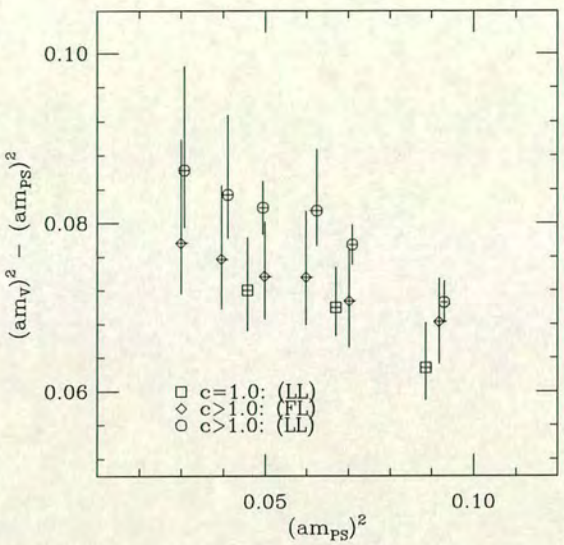

Figure 2.8: Hyperfine splitting at $\beta = 6.2$ in lattice units for $c_{sw} = \{1.0, 1.4424\}$.

study the hyperfine splitting in charmonium for the Wilson ($c_{sw} = 0$) and SW-actions. However, it consists of a reduced dataset of only 18 configurations so there will be large statistical errors. These results are shown in Figure 2.9. The scale has been set from the ρ mass. Secondly, the spin-averaged splitting at a lower β is examined. At $\beta = 5.7$ a similar analysis has been done [28] with higher statistics using three different fermionic actions (including results from the GF11 collaboration [34]). This is shown in Figure 2.10. At $\beta = 6.2$, little effect is seen on changing the clover coefficient from $c_{sw} = 0$ to $c_{sw} = 1$ and then to $c_{sw} > 1$. However, there is a significant change in slope at $\beta = 5.7$ on going from $c_{sw} = 0$ to $c_{sw} = 1$. Again, little effect is seen after tadpole improvement. The reason for the lack of improvment as the clover coefficient is increased is unclear. There are two possibilities: the clover term is of limited value in reducing discretisation effects in this particular quantity or, other errors (*e.g.* from setting the scale) are relevant.

An interesting argument by Fiebig and Woloshyn [35] is that the lack of constancy

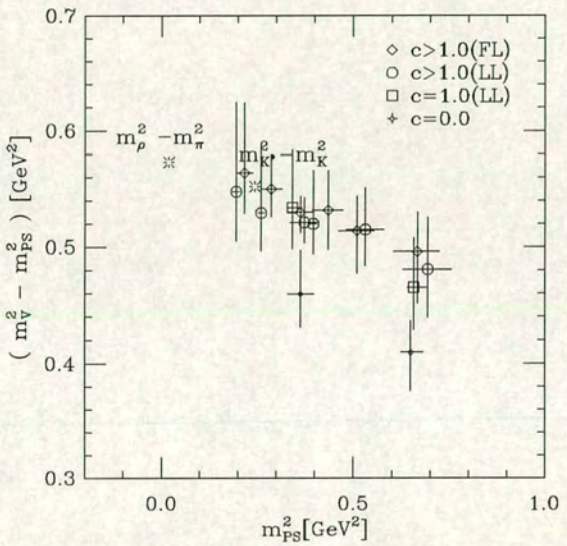

Figure 2.9: Mass splittings at $\beta = 6.2$ in GeV. All available values of c_{sw} are included in this plot. There is evidence for improvement on increasing the clover coefficient from 0 to 1 (+ to □). However, there is little change in the slope after further increasing c_{sw}.

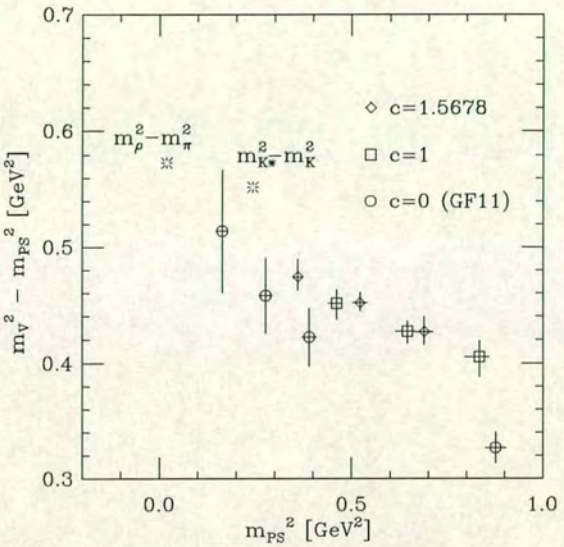

Figure 2.10: Mass splittings at $\beta = 5.7$. 150 gauge field configurations were used on a $16^3 \times 32$ lattice. Sources are Jacobi smeared.

in $(m_V^2 - m_{PS}^2)$ may be due to chiral effects away from the chiral limit. This is based on a paper which argues that the constant behaviour of the vector-pseudoscalar mass splitting is an algebraic consequence of the chiral symmetry in QCD [36]. For lattice calculations with Wilson fermions the deviation from a constant of $(m_V^2 - m_{PS}^2)$ may be an indication of the rôle of the Wilson term in the action (this term explicitly breaks chiral symmetry). Supporting this hypothesis is the very different behaviour observed for staggered fermions, which have different chiral properties, keeping a remnant of chiral symmetry [37].

2.8 The Decay Constants

It has been argued [32, 33] that the decay constants in a quenched theory will be lower than their experimental values. The authors in [32] argue that since the leading coefficient, β_0, entering the Callan-Symanzik equation is larger in the quenched approximation than in the full theory, the quark charge falls faster with momentum after quenching the theory and, therefore, at short distances the

attractive quark-antiquark potential in quenched QCD will be weaker than the full theory. So mesonic wave functions will be more spread out at the origin. Decay constants are proportional to quark-antiquark wave functions and hence will be lower for quenched QCD than for full QCD.

In this section the pseudoscalar, (f_π, f_K) and vector, $(1/f_\rho, 1/f_{K^*}, 1/f_\phi)$ decay constants are compared in the quenched approximation, for different c_{sw} values.

2.8.1 Fit Functions for the Decay Constants

The Pseudoscalar Decay Constants

The pseudoscalar decay constant, f_{PS}, is determined from a ratio of two-point correlators

$$C_{PP} = \sum_{\mathbf{x}} \langle P_5(\mathbf{x}, t), P_5^\dagger(0,0)\rangle, \tag{2.15}$$

and

$$C_{AP} = \sum_{\mathbf{x}} \langle A_4(\mathbf{x}, t), P_5^\dagger(0,0)\rangle, \tag{2.16}$$

which are fitted to the following expressions

$$C_{PP} \sim \frac{\mathcal{Z}_{PP}}{m_{\rm PS}} \exp^{-m_{\rm PS}\frac{N_t}{2}} \cosh\left(m_{\rm PS}\left(\frac{N_t}{2} - t\right)\right), \tag{2.17}$$

$$C_{AP} \sim \frac{\mathcal{Z}_{AP}}{m_{\rm PS}} \exp^{-m_{PS}\frac{N_t}{2}} \sinh\left(m_{\rm PS}\left(\frac{N_t}{2} - t\right)\right). \tag{2.18}$$

$\mathcal{Z}_{PP}$ and $\mathcal{Z}_{AP}$ are the amplitudes from which the hadronic matrix elements and $m_{\rm PS}$ are extracted.

$$\begin{aligned} \mathcal{Z}_{PP} &= |\langle 0|P_5|P\rangle|^2, \\ \mathcal{Z}_{AP} &= |\langle 0|A_4|P\rangle||\langle 0|P_5|P\rangle| = \frac{1}{Z_A} f_{\rm PS} m_{\rm PS} |\langle 0|P_5|P\rangle|. \end{aligned} \tag{2.19}$$

The ratio of the correlators in Equations (2.17) and (2.18) is

$$\frac{\sum_{\mathbf{x}}\langle A_4(x,t)P^\dagger(0)\rangle}{\sum_{\mathbf{x}}\langle P(x,t)P^\dagger(0)\rangle} \sim \frac{f_{\rm PS} m_{\rm PS}}{Z_A\langle 0|P|P\rangle} \tanh\left(m_{\rm PS}\left(\frac{N_t}{2} - t\right)\right). \tag{2.20}$$

The factors $m_{\rm PS}$ and $\langle 0|P|P\rangle$ are determined via the effective mass fits. Although in principle, either $\langle A_4(x,t)P^\dagger(0)\rangle$ or $\langle P(x,t)A_4^\dagger(0)\rangle$ can be used in the ratio (2.20), the former gives a better signal and is used.

The Vector Decay Constants

The normalisation of the vector current is chosen to be

$$\langle 0|J_j^\mu|V(p,\epsilon,j)\rangle = \epsilon^\mu \frac{m_V^2}{Z_V f_V}, \tag{2.21}$$

and the vector decay constant is determined from the two-point correlation function

$$\sum_{j=1}^{3}\sum_{\mathbf{x}}\langle V_j(x,t)V_j^\dagger(0)\rangle \sim \frac{\mathcal{Z}_V}{m_V}\exp^{-m_V\frac{N_t}{2}}\cosh\left(m_V\left(\frac{N_t}{2}-t\right)\right). \tag{2.22}$$

where as before $\mathcal{Z}_V$ is the amplitude, which using the normalisation defined in Equation (2.21) is

$$\begin{aligned}\mathcal{Z}_V &= |\langle 0|V_j|V\rangle||\langle 0|V_j|V\rangle|,\\ &= \frac{1}{Z_V^2}\left(\frac{m_V^4}{f_V^2}\right).\end{aligned} \tag{2.23}$$

The vector decay constants can then be determined from a fit to

$$\frac{3m_V^3}{Z_V^2 f_V^2}\exp^{-m_V\frac{N_t}{2}}\cosh\left(m_V\left(\frac{N_t}{2}-t\right)\right). \tag{2.24}$$

Renormalisation Constants

The constants, Z_A and Z_V, are needed to reconcile the lattice currents with the current algebra in the continuum limit. These constants have been calculated perturbatively [29] for a tapole improved SW-action, giving (at $\beta = 6.2$)

$$Z_\Gamma = 1 + \xi_\Gamma\left[\frac{2N}{\beta}\frac{c^{\frac{4}{3}}}{4\pi}\right], \tag{2.25}$$

with $\xi_{\overline{\psi}\gamma_\mu\gamma_5\psi} = -0.54$ and $\xi_{\overline{\psi}\gamma_\mu\psi} = -0.66$.

$$Z_A = 0.932, \tag{2.26}$$

$$Z_V = 0.917. \tag{2.27}$$

The corresponding values for $c_{sw} = 1$ are

$$Z_A = 0.98, \tag{2.28}$$

$$Z_V = 0.83. \tag{2.29}$$

A non-perturbative calculation of the renormalisation constants has been done for the $c_{sw} = 1$ case, with the results [30],

$$Z_A = 1.045^{+10}_{-14}, \tag{2.30}$$

$$Z_V = 0.817^{+\,2+\,8}_{-\,2-\,8}. \tag{2.31}$$

To date, no equivalent calculation has been done for the tapole-improved action used here.

At this point, rotations of the quark propagators are important. Although this is not the case for extracting masses, for calculations of matrix elements rotations must be included for improvement.

The correlators for $c_{sw} = 1$ data are generated with rotated propagators. However, the correlators for $c_{sw} = 1.4424$ are not and the rotations must be put in by hand. The equations of motion can be used to express the expectation value of an improved, on-shell observable, bilinear in the quark fields, as [15, 16]

$$\mathcal{O}_\Gamma = (1 + am_q\,(1 - z))\,\overline{\psi}(x)\left(\Gamma + z\frac{a}{2}\gamma_\mu D^\mu\right)\psi(x), \tag{2.32}$$

where $0 \leq z \leq 1$ and no rotations means implicitly setting $z = 0$. Therefore to explicitly include rotations requires a multiplication by $1 + am_q$ where m_q is the

bare quark mass given by

$$m_q = \frac{1}{2}\left(\frac{1}{\kappa} - \frac{1}{\kappa_c}\right). \tag{2.33}$$

An issue with this expression is the value to be used for κ_c *i.e.* the one-loop perturbative value of 1/8 or the value of κ_c determined from the simulations. From Table 2.6, using tadpole-improved data these numbers are quite close and it has been shown [31] that the final values of both $f_{\rm PS}$ and $1/f_V$ are consistent within errors. The non-perturbative, extrapolated value of κ_c is therefore used.

2.8.2 Results for the Pseudoscalar Decay Constants

The pseudoscalar decay constants were determined from a fit to Equation (2.20). The fitting ranges used were the same as those quoted in Table 2.2 for the fitted masses. An initial comparison of the decay constants was done using the perturbative values of the renormalisation constants for both the $c_{sw} = 1$ and $c_{sw} > 1$ cases. The value of f_π was determined by linearly extrapolating $f_{\rm PS}$ in $m^2_{\rm PS}$ to $m^2_{\rm PS} = 0$. To compare with experiment $f_{\rm PS}/m_V$ is plotted against $m^2_{\rm PS}$ in Figure 2.11. Table 2.11 lists the chirally extrapolated values of the pseudoscalar decay constants.

From Figure 2.11, I note that the local, tadpole-improved data are further from the experimental values than for $c_{sw} = 1$, although the slopes are still in agreement. When fuzzed $c_{sw} > 1$ data are used, the ratio $f_{\rm PS}/m_V$ moves towards the experimental numbers, but the slope is also closer to a constant.

However, for the $c_{sw} = 1$ case, the non-perturbative values of the renormalisation constant given in Equation (2.30) can be used for a more accurate value. These numbers are also in Table 2.11. The effect of changing the renormalisation constant is now clear: the $c_{sw} = 1$ numbers are improved, moving closer to the experimental values. Taking the current best numbers at both c_{sw} values the ratio f_π/m_ρ is 0.144(6) for $c_{sw} = 1$ and 0.142(10) for $c_{sw} > 1$ as compared with experiment, 0.172.

$f_{\rm PS}$	$c_{sw}=1.0$		$c_{sw}>1.0$	
	$Z_A=0.97$	$Z_A=1.045$	$Z_A=0.932$	
	(LL,LL)	(LL,LL)	(LL,LL)	(LL,FL)
f_π	0.0388^{+10}_{-15}	0.0418^{+10}_{-15}	0.0377^{+17}_{-17}	0.0419^{+28}_{-28}
f_K	0.0455^{+2}_{-3}	0.0502^{+2}_{-3}	0.0464^{+1}_{-2}	0.0504^{+4}_{-4}
f_K/f_π	1.20^{+3}_{-2}	1.20^{+3}_{-2}	1.23^{+3}_{-4}	1.21^{+6}_{-6}
f_π/m_ρ	0.134^{+6}_{-6}	0.144^{+6}_{-6}	0.124^{+9}_{-9}	0.142^{+9}_{-10}

Table 2.11: The pseudoscalar decay constants are determined at $c_{sw}=1$ using a perturbative and a non-perturbative Z_A. Only a perturbative value is used at $c_{sw}>1$, but local and fuzzed data are used.

2.8.3 Results for the Vector Decay Constants

A linear extrapolation of $1/f_V$ to m_ρ gives the decay constant $1/f_\rho$, and interpolating to the ϕ and K^* masses gives $1/f_\phi$ and $1/f_{K^*}$. The vector decay constants also show a significant change due to tadpole improvement, this time, however, towards the experimental values. Table 2.12 lists the decay constants determined with perturbative and non-perturbative values of the renormalisation constant Z_V for $c_{sw}=1$ and at $c_{sw}>1$ with the perturbative Z_V. From Equations (2.31) and (2.29) the perturbative and non-perturbative values of Z_V are almost the same and so unlike the pseudoscalar case there is very little uncertainty to be attached to this perturbative number. Once again the use of fuzzing increases the value

$1/f_V$	$c_{sw}=1.0$		$c_{sw}>1.0$	
	$Z_V=0.83$	$Z_V=0.817$	$Z_V=0.917$	
	(LL,LL)	(LL,LL)	(LL,LL)	(LL,FL)
$1/(f_\rho)$	0.316^{+7}_{-13}	0.311^{+7}_{-13}	0.271^{+9}_{-9}	0.288^{+10}_{-9}
$1/(f_\phi)$	0.280^{+3}_{-6}	0.276^{+3}_{-6}	0.235^{+4}_{-5}	0.240^{+4}_{-4}
$1/(f_{K^*})$	0.298^{+5}_{-9}	0.293^{+5}_{-9}	0.254^{+6}_{-6}	0.268^{+7}_{-7}

Table 2.12: Vector decay constants. These again are calculated using perturbative and non-perturbative values of Z_V at $c_{sw}=1$ and both local and fuzzed data at $c_{sw}>1$ with a perturbative value of Z_V.

of the decay constants, in this case, however, moving the data away from experi-

ment although the extrapolated values agree with experimental numbers, within errors.

2.8.4 Comparison with Experiment

In Table 2.13 the results at different c_{sw} values are compared with the experimental data available. The scale has been set from the ρ mass for both values of the clover coefficient. In Figure 2.11 the decay constants are plotted with the relevant

Physical Quantity	$c_{sw}=1$	$c_{sw}>1$		Expt
	(LL,LL)	(LL,LL)	(LL,FL)	
f_π	113^{+3}_{-3}	97^{+4}_{-4}	109^{+8}_{-8}	132
f_K	135^{+8}_{-8}	119^{+3}_{-3}	131^{+5}_{-5}	160
$1/f_\rho$	0.311^{+7}_{-13}	0.271^{+9}_{-9}	0.286^{+9}_{-9}	0.28
$1/f_\phi$	0.276^{+3}_{-6}	0.235^{+4}_{-5}	0.240^{+4}_{-4}	0.23
f_π/m_ρ	0.144^{+6}_{-7}	0.124^{+9}_{-9}	0.142^{+10}_{-10}	0.172
f_K/m_ρ	0.160^{+7}_{-8}	0.152^{+7}_{-7}	0.170^{+6}_{-7}	0.208
f_K/m_{K^*}	0.144^{+5}_{-6}	0.131^{+7}_{-7}	0.149^{+6}_{-6}	0.179
$m_\phi/f_\phi m_\rho$	0.351^{+8}_{-9}	0.301^{+7}_{-7}	0.308^{+5}_{-5}	0.305

Table 2.13: A comparison with experimental values. The values quoted for $c_{sw}=1$ are determined using the non-perturbative renormalisation constants. All the values quoted are in MeV

experimental values included.

From Figure 2.11 it appears tadpole improvement is having an adverse effect on the pseudoscalar decay constants. A dimensionless ratio is plotted so errors due to setting the scale are not relevant. It may be that in reducing the discretisation errors other effects become more noticeable, which previously had cancelled. The data do also appear to be constant with increasing quark mass. However, no firm conclusions can be drawn at this stage without a non-perturbative determination of Z_A. In a ratio of pseudoscalar decay constants Z_A is cancelled and this can then be reliably compared with experiment. The ratio f_K/f_π, in Table 2.14 is found to be consistently in agreement with experiment, suggesting that the perturbative estimation of Z_A is not accurate. Figure 2.11 shows that tadpole improvement

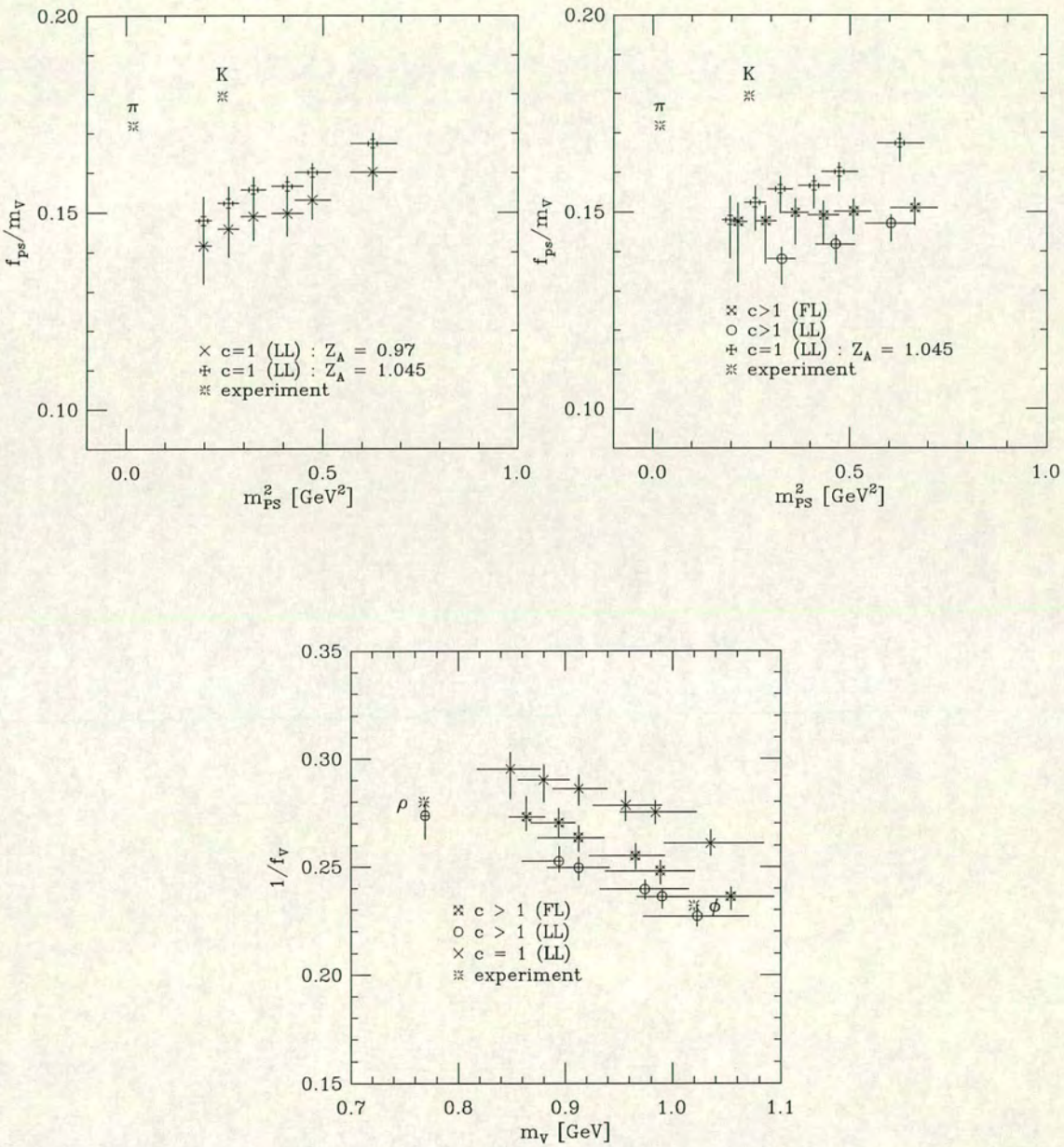

Figure 2.11: Vector and Pseudoscalar decay constants. The vector decay constants plotted at $c_{sw} = 1$ have been determined with the non-perturbative Z_V. The experimental values of the pion, kaon, ρ and ϕ decay constants are shown on the relevant plots.

Ratio	$c_{sw} = 1$		$c_{sw} > 1$		Expt
	$Z_A = 0.97$	$Z_A = 1.045$	$Z_A = 0.932$		
	(LL,LL)	(LL,LL)	(LL,LL)	(LL,FL)	
f_K/f_π	1.20^{+3}_{-3}	1.20^{+3}_{-2}	1.23^{+3}_{-4}	1.21^{+6}_{-6}	1.21

Table 2.14: The ratio f_K/f_π compared with experiment : it is independent of Z_A

has a substantial effect on the vector decay constants. Here, there is less uncertainty attached to the renormalisation constant since the perturbative and non-perturbative Z_V agree. The decay constants are higher in value than the experimental numbers but there is agreement within errors. In [23] it was concluded that significant discretisation or finite volume effects were the cause of the higher than expected values of the vector decay constants, given the argument in [32]. Removing leading discretisation effects has brought the numbers into much better agreement and maintained a slope in agreement with experiment. Since the value of Z_V is not expected to change greatly when it is calculated non-perturbatively this is very encouraging.

2.9 Summary

The spectrum and decay constants have been calculated and compared using two values of the clover coefficient. Although it is not expected that at $\beta = 6.2$ the evidence of improvement will be as great as for a coarser lattice, *e.g.* $\beta = 5.7$, this study is worthwhile since it is done on a dataset where the only change is the introduction of tadpole improvement and the subsequent introduction of fuzzed data. It is therefore possible (and reassuring) to confirm that there are no pathologies associated with using $c_{sw} > 1$. The consistency between results at $c_{sw} = 1$ and $c_{sw} > 1$ also confirms that discretisation effects are small at $\beta = 6.2$. As expected, the value of κ_c is in much better agreement with the tree-level prediction but in general, spectral quantities show little change after tadpole improvement. The values of J and the hyperfine splitting are unchanged, at least within statistical errors. The parameter J appears to be independent of

the lattice spacing and the fermionic action used and so a lack of change here is not unexpected. The discrepancy with experiment is believed to be a quenching effect. For the mass splitting, a substantial improvement is seen when the clover term is introduced to the Wilson fermion action. This occurs at $\beta = 5.7$ and to a lesser extent at $\beta = 6.2$. However, the subsequent lack of improvement on increasing the effect of the clover term is puzzling and may indicate that other errors are now dominant. This trend was also seen by Woloshyn and collaborators [35] who compared a two-link next-to-nearest-neighbour action with the Wilson action. There is also a lack of change in the Edinburgh plot, except for a small effect at the lightest quark mass, which appears to have been underestimated by the local data. This is further investigated with higher statistics in the next chapter.

There is a significant change in the decay constants. The pseudoscalar decay constants move further from their experimental values. However, the significance of this trend cannot be accurately assessed until a non-perturbative determination of Z_A is made. Ratios of pseudoscalar decay constants are consistent with experiment, which is encouraging. For the vector decay constants more conclusive statements can be made, since there is not the same level of uncertainty in the renormalisation constant, Z_V. The tadpole data show definite improvement, lying slightly below the experimental values for the local $c_{sw} > 1$ case and above for the fuzzed $c_{sw} > 1$ data. Both are closer to experimental numbers than the $c_{sw} = 1$ results. The change in value of both the pseudoscalar and vector decay constants with the introduction of fuzzing needs to be understood.

In summary, lattice determinations of some quantities are more sensitive to tadpole improvement than others. Although for some quantities there is no change the situation is not made worse : a condition of improvement. Using a tadpole-improved action changes the coefficient of the $\mathcal{O}(ag^2)$ errors in physical quantities, hopefully reducing them. This may mean that errors due to the quenched approximation and the finite volume of the lattice, which were previously suppressed or cancelled, are now more visible and must be investigated in a separate study.

In a recent paper by Lüsher *et al.* [38] the clover coefficient, c_{sw} is evaluated non-

perturbatively using a Schrödinger functional on quark states. The value quoted is significantly larger than the number used in this work (for $\beta = 6.2$ it is ≈ 1.8). It may be that further improvement will be seen on using this value in future simulations.

Chapter 3

The Light Hadron Spectrum and Decay Constants at $\beta = 6.2$

A precision calculation of the light hadron spectrum is an important task for Lattice QCD. Accurate results here would confirm QCD as the theory of the strong interaction and also inspire confidence in the calculation of other non-perturbative quantities, which are of phenomenological interest.

That simulating light quarks is difficult, is well established. The size of hadrons made from u and d quarks is determined by the pion Compton wavelength so that large lattices are needed to calculate them. Also, the u and d quark masses are small, making the Dirac matrix badly-conditioned and costly to invert. For this reason, it is impractical to work at physical, light quark masses. So, in general, simulations are done for unphysically heavy quarks and the results extrapolated to the physical regime. Present day computer power and algorithms allow hadrons containing one or more strange quarks to be simulated directly on the lattice. With just one additional input parameter, many more (strange) hadrons become calculable.

Because of the computational cost, the quenched approximation is very often employed to make large-scale calculations feasible. Unfortunately though, the effect of a fermion loop is, roughly, inversely proportional to its mass, so that light hadrons are expected to be amongst the quantities most severely affected by quenching.

It is now accepted that high statistics are an essential part of a light hadron simulation, to reduce statistical errors and thereby make systematic effects *e.g.* from quenching, identifiable.

The question therefore is : can hadrons made of u, d and s quarks be reliably simulated in quenched Lattice QCD ?

3.1 Simulation Details

Most of the computational details have already been given in Chapter 2, where a subset of 60 fuzzed, gauge field configurations was analysed. In this chapter, 220, $24^3 \times 48$ gauge configurations are used in a high statistics study of the tadpole-improved, light hadron spectrum and decay constants at $\beta = 6.2$.

Meson correlators are constructed from fuzzed quark propagators using all degenerate and non-degenerate κ combinations. The baryon correlators are constructed from degenerate combinations of the fuzzed propagators only. All the propagators used in this analysis are unrotated. The clover coefficient is $c = 1/u_0^3$. The lattice parameters for this simulation are in Table 3.1.

Configurations	220
κ	0.13640, 0.13710, 0.13745
u_0 : c	0.88506 : 1.4424
Meson Fuzzing Combinations	(LL,LL),(LL,LF) (LL,FL),(LL,FF)
Baryon Fuzzing Combinations	(LL,LL,LL),(LF,LF,LL) (FL,FL,LL),(FF,FF,LL)

Table 3.1: κ values and fuzzing combinations used for both mesons and baryons.

3.2 Extracting Fitted Masses

The motivation for fuzzing is to minimise the overlap between the ground state and the first excited state. Using correlators, built from propagators with different fuzzing combinations (see Table 3.1), a multi-exponential fit to the data is possible. In this analysis, mesons and baryons composed of local correlators and correlators fuzzed at the source are used in a double exponential fit to the following,

$$y_M \sim A_M \exp^{-m_0 x} + A_M \exp^{-m_0 (N_t - x)} + B_M \exp^{-m_1 x} + A_M \exp^{-m_1 (N_t - x)} \quad (3.1)$$

$$y_B \sim A_B \exp^{-m_0 x} + B_B \exp^{-m_1 x}. \quad (3.2)$$

where the labels M and B refer to mesons and baryons. N_t is the lattice extent in the time direction and, A and B are the amplitudes of the ground and excited states respectively. The masses, m_0 and m_1, of the ground and first excited state, are extracted for all κ combinations. For a range of $t_{\rm min}$ and $t_{\rm max}$ the ground state, first excited state and the χ^2/d.o.f. are recorded. Figures 3.1, 3.2 and 3.3 show that the ground state mass can be clearly distinguished from the excited state contribution. The degenerate κ combinations are shown here (this is the only baryon data analysed) but the results are similar for the non-degenerate mesons.

Figure 3.4 demonstrates why the correlator, (LL,FL) is chosen for both the double and single exponential fits to the data. The signal for this combination is much cleaner than for the other three possibilities and the plateau is longer and more stable. This, combined with higher statistics, means that it is possible to fit to $t_{\rm max} \sim 23$. The figure shows the effective mass of the vector meson, for the non-degenerate κ combination, $(0.13745, 0.13640)$. The pattern is the same for all quark masses, degenerate and non-degenerate, and for all particles considered here.

From the sliding-window fits, a fitting range can be chosen, from which the ground state mass is determined, satisfying the following criteria

- the fit has an acceptable χ^2/d.o.f. which is taken to mean χ^2/d.o.f. ≈ 1.
- the ground state mass is stable for $t_{\rm min} \pm 1$.
- the excited state mass is clearly separated from the ground state.
- the value of m_0 is consistent for single and multi-exponential fits.

Using a single exponential function to fit the (LL,FL) and (FL,FL,LL) data, the ground state masses for all κ combinations are extracted, obeying the χ^2/d.o.f. and stability requirements. The results from single and double exponential fits are

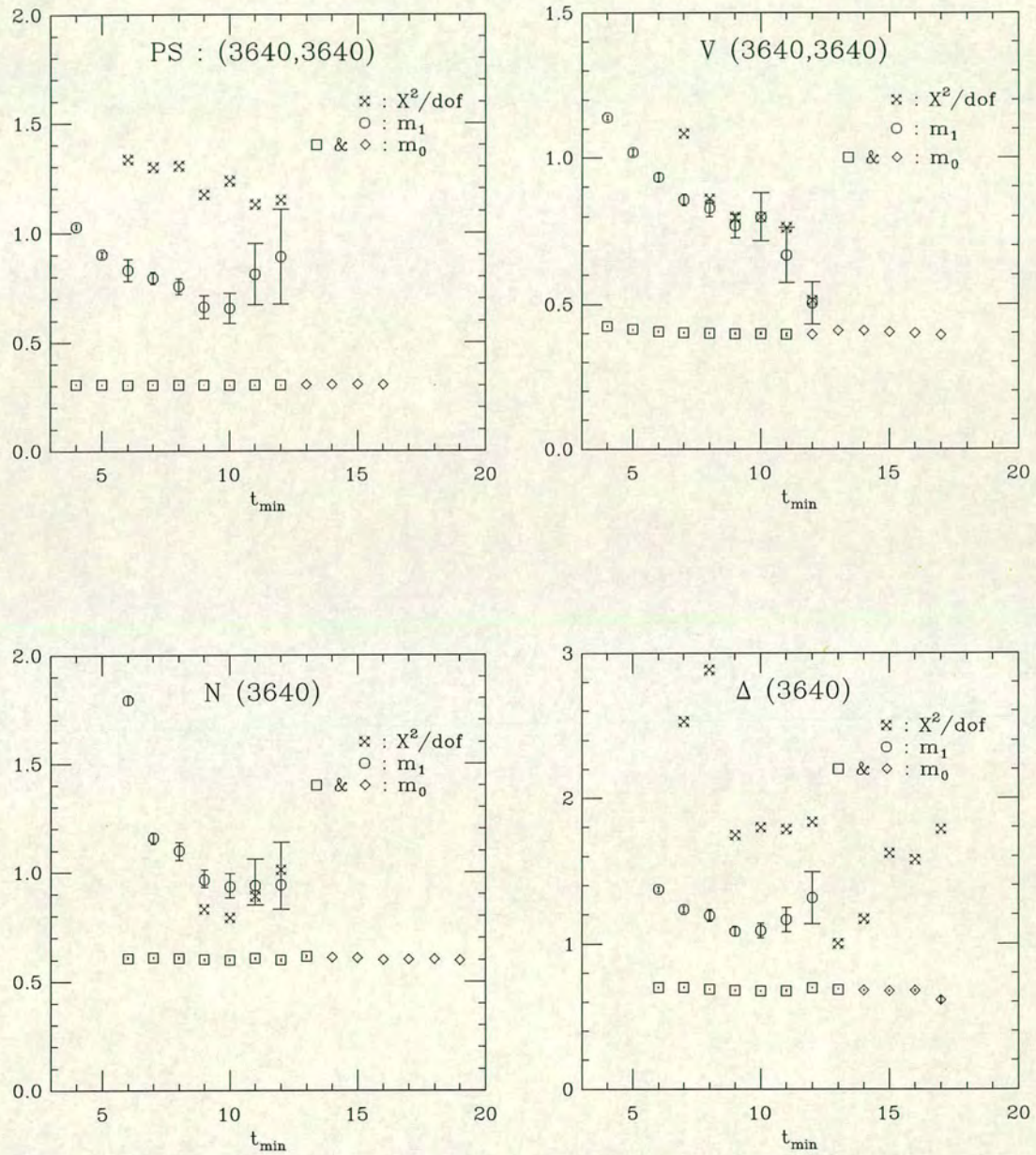

Figure 3.1: Sliding-window plots for the pseudoscalar, vector meson, nucleon and Δ at the κ combination $(0.13640, 0.13640)$. The squares and diamonds are the ground state masses (m_0), fitted at different t_{min}. Squares, are the mass determined from a double exponential fit and diamonds from a single exponential. The excited state mass is represented by the octogons and stars are the χ^2/d.o.f..

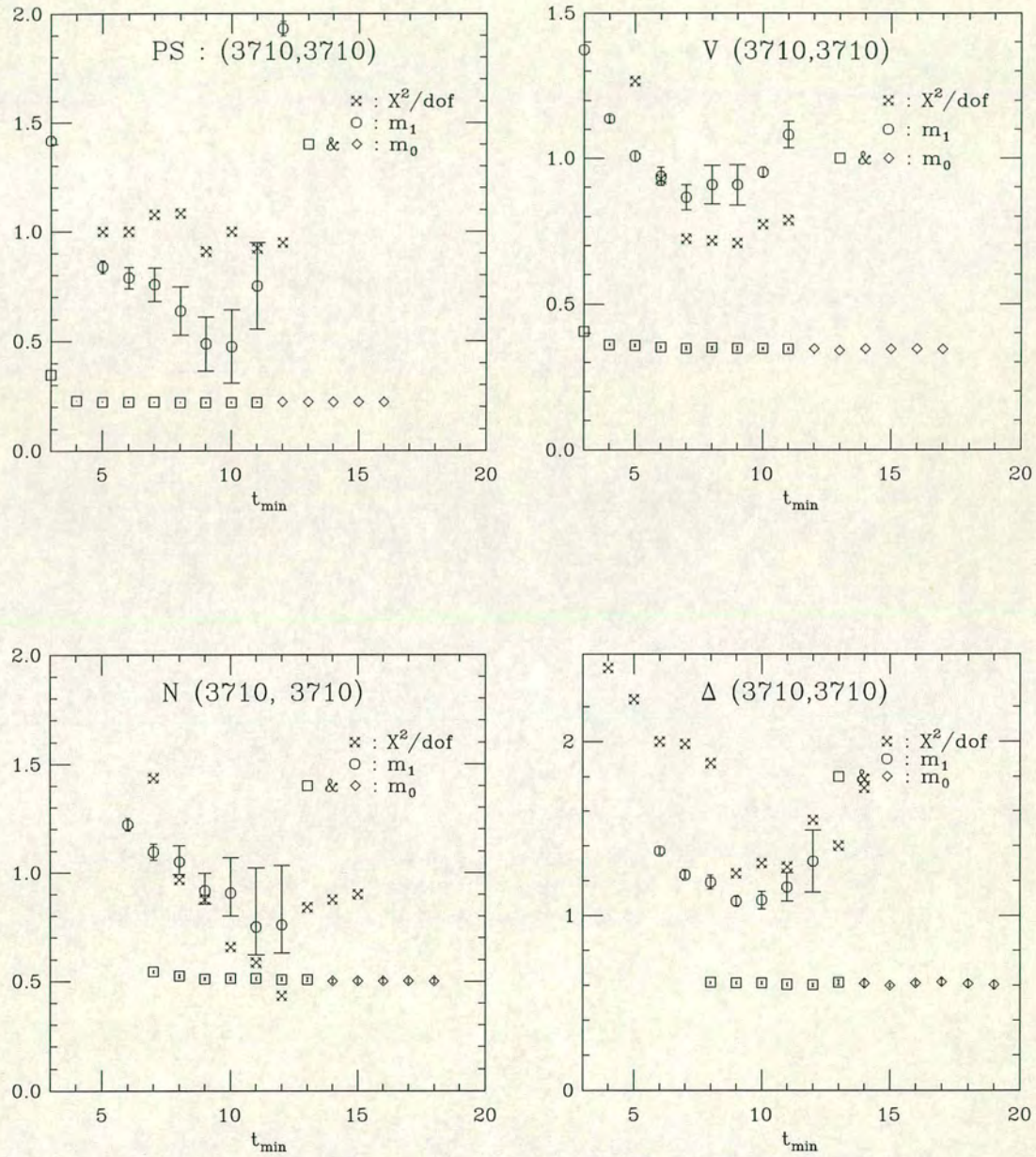

Figure 3.2: Sliding-window plots for the pseudoscalar, vector meson, nucleon and Δ at the κ combination $(0.13710, 0.13710)$. The convention for the plotting symbols is the same as in Figure 3.1.

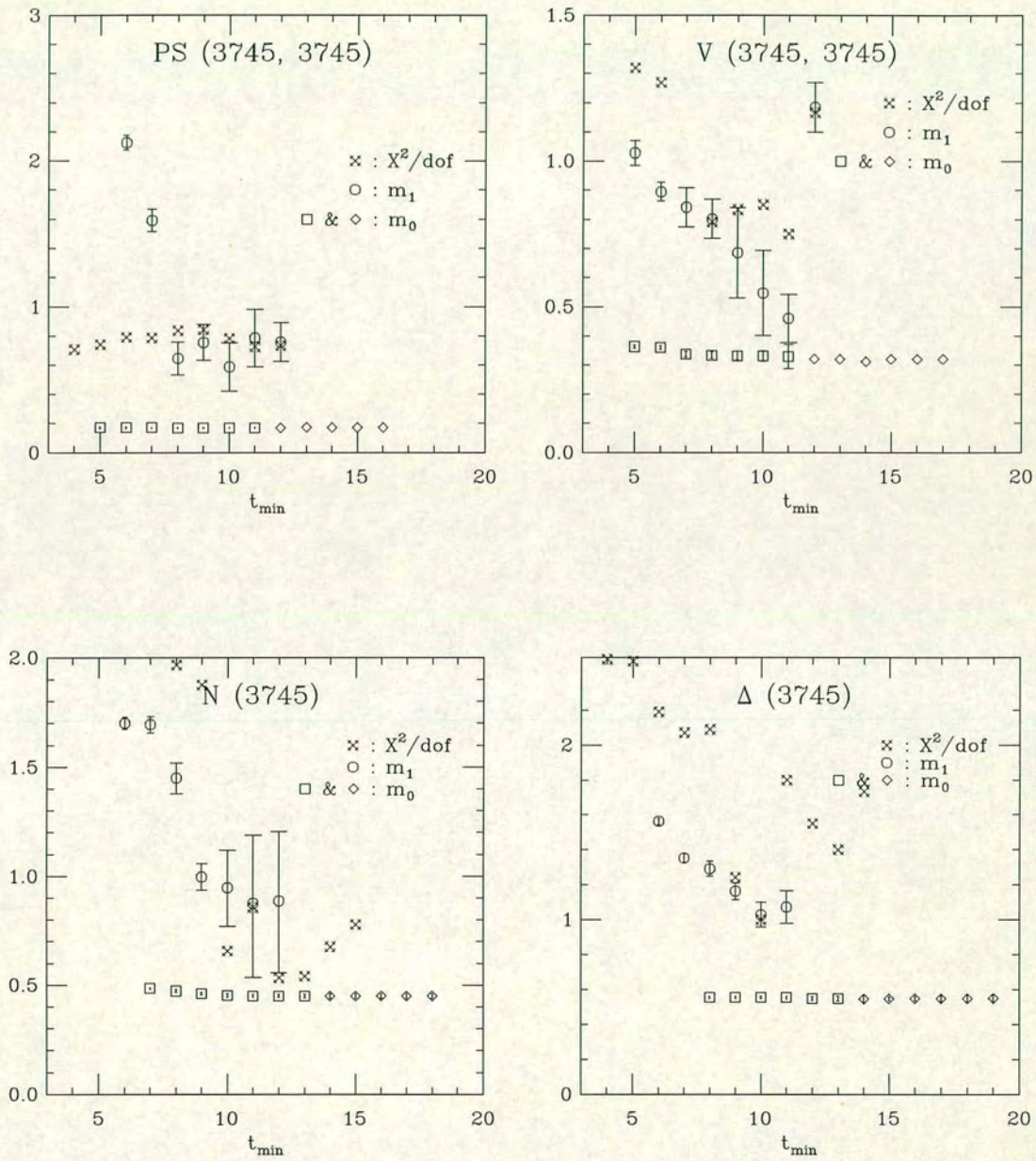

Figure 3.3: Sliding-window plots for the pseudoscalar, vector meson, nucleon and Δ at the κ combination $(0.13745, 0.13745)$. Once again, the convention for the plotting symbols is the same as in Figure 3.1.

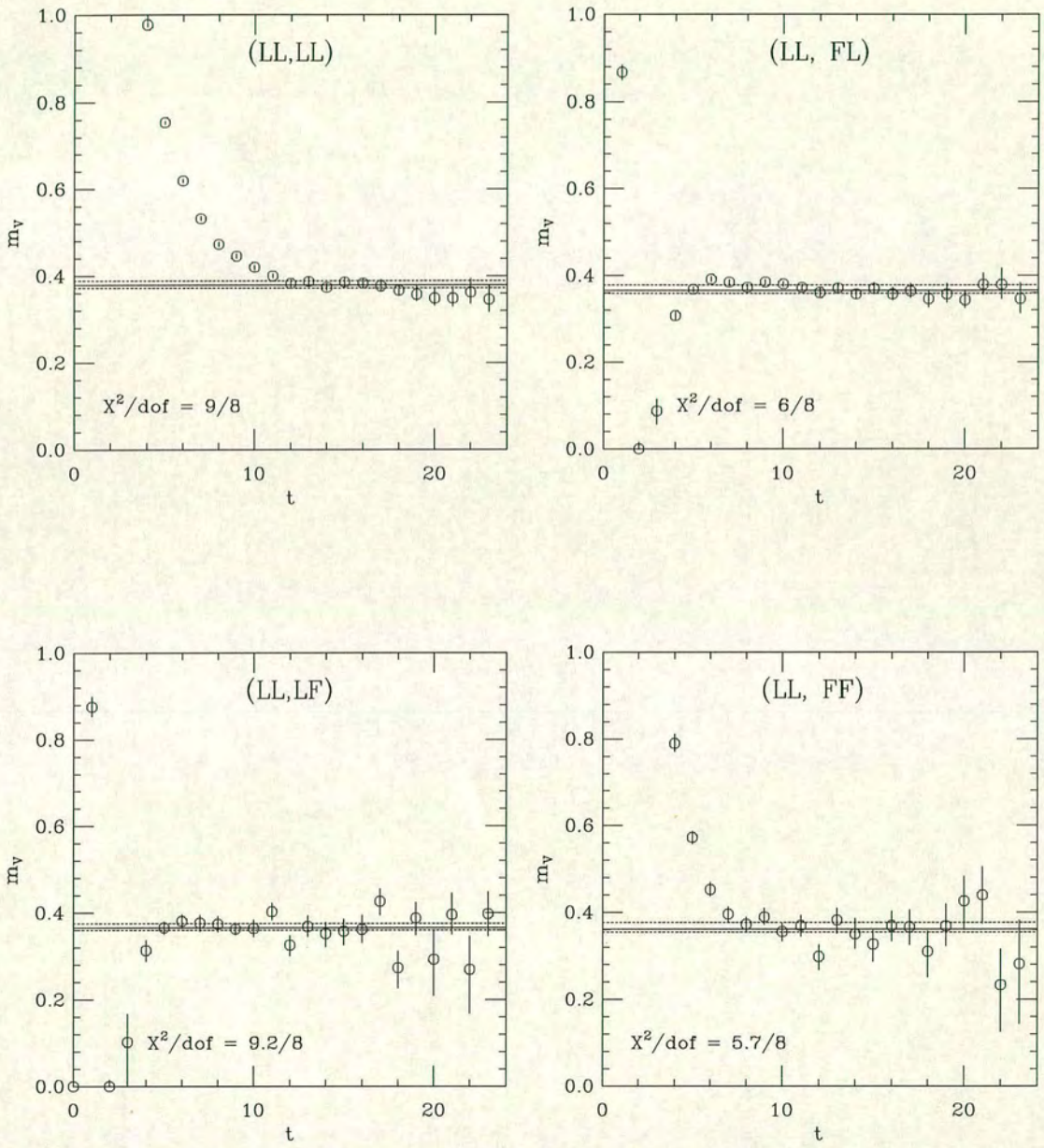

Figure 3.4: Single exponential fits to the effective mass of the vector meson, for the nondegenerate κ combination, $(0.13745, 0.13640)$, for all four possible fuzzing combinations. The fitting range in all cases is $12 - 22$.

compared in Tables 3.2 to 3.5. The fitted masses agree within errors, in all cases. This implies that using a single exponential function determines the ground state mass correctly, for high statistics and fuzzed data. A single exponential fit to the data is therefore reliable and has the advantage that it is more easily automated than a multi-exponential fitting program.

κ_1	κ_2	Fit type	m_{PS}	Fit Range	χ^2/d.o.f.	Q
0.13640	0.13640	1exp	0.303^{+1}_{-1}	10–22	0.84	0.611
		2exp	0.303^{+2}_{-2}	9–23	1.1	0.599
0.13710	0.13640	1exp	0.265^{+1}_{-1}	10–22	0.92	0.657
		2exp	0.267^{+2}_{-2}	6–23	1.2	0.627
0.13710	0.13710	1exp	0.222^{+1}_{-1}	10–22	0.81	0.575
		2exp	0.223^{+2}_{-2}	5–23	1.0	0.667
0.13745	0.13640	1exp	0.244^{+2}_{-2}	10–22	0.93	0.474
		2exp	0.243^{+1}_{-1}	6–23	0.86	0.511
0.13745	0.13710	1exp	0.198^{+2}_{-2}	10–22	0.86	0.326
		2exp	0.197^{+1}_{-1}	6–23	0.75	0.343
0.13745	0.13745	1exp	0.171^{+2}_{-2}	10–22	0.78	0.121
		2exp	0.171^{+4}_{-3}	6–23	0.79	0.372

Table 3.2: Pseudoscalar masses for all κ combinations, using both single and double exponential fits.

3.3 Mass Predictions in Hadron Spectroscopy

As described at the beginning of this chapter, the masses of non-strange hadrons are determined by extrapolation, whereas those hadrons containing strange quarks are simulated directly on the lattice and can be determined by interpolation. Both methods have already been used in Chapter 2 but here these methods are investigated more thoroughly.

3.3.1 Extrapolations

Having arrived at final values for the fitted masses, using the minimising χ^2/d.o.f. analysis at each κ value, as described in §3.2, the first step is to determine κ_c. This procedure is used in Chapter 2 : the pseudoscalar masses are extrapolated

κ_1	Fit Type	m_N	Fit Range	χ^2/d.o.f.	Q
0.13640	1exp	0.599^{+8}_{-8}	12–21	1.01	0.367
	2exp	0.594^{+10}_{-7}	10–21	0.79	0.462
0.13710	1exp	0.507^{+10}_{-9}	12–21	0.43	0.229
	2exp	0.502^{+9}_{-9}	10–21	0.66	0.321
0.13745	1exp	0.454^{+12}_{-11}	13–21	0.54	0.121
	2exp	0.451^{+11}_{-9}	10–21	0.67	0.309

Table 3.3: Nucleon masses for all κ combinations, for single and double exponential fits.

κ_1	κ_2	Fit Type	m_V	Fit Range	χ^2/d.o.f.	Q
0.13640	0.13640	1exp	0.399^{+2}_{-2}	11–23	1.86	0.666
		2exp	0.399^{+4}_{-4}	7–23	0.6	0.853
0.13710	0.13640	1exp	0.374^{+3}_{-3}	11–23	1.70	0.776
		2exp	0.378^{+4}_{-4}	7–23	0.8	0.771
0.13710	0.13710	1exp	0.347^{+4}_{-4}	12–22	1.26	0.887
		2exp	0.348^{+6}_{-6}	7–23	0.8	0.955
0.13745	0.13640	1exp	0.361^{+4}_{-4}	12–22	1.32	0.474
		2exp	0.360^{+6}_{-6}	6–22	1.2	0.593
0.13745	0.13710	1exp	0.337^{+5}_{-5}	12–22	1.00	0.326
		2exp	0.336^{+4}_{-4}	6–22	0.91	0.512
0.13745	0.13745	1exp	0.323^{+7}_{-7}	12–22	0.89	0.126
		2exp	0.323^{+6}_{-5}	6–22	0.84	0.372

Table 3.4: Vector masses for degenerate and nondegenerate κ combinations. Single and double exponential fits are used.

κ_1	Fit Type	m_Δ	Fit Range	χ^2/d.o.f.	Q
0.13640	1exp	0.646^{+10}_{-11}	12–21	0.3	0.455
	2exp	0.642^{+12}_{-14}	9–21	1.8	0.555
0.13710	1exp	0.582^{+12}_{-13}	12–21	0.4	0.365
	2exp	0.574^{+13}_{-14}	9–21	1.4	0.427
0.13745	1exp	0.567^{+21}_{-23}	13–22	0.99	0.209
	2exp	0.555^{+22}_{-22}	10–21	1.6	0.341

Table 3.5: Δ masses for single and double exponentials, for the degenerate κ combinations.

to $m_{\rm PS}^2 = 0$, where κ_c is defined. The χ^2/d.o.f. of this fit is high, ≈ 11, but this is probably a consequence of the extremely small errors on the fitted pseudoscalar masses and not an indication that the fit is "bad". In [44] it was noted that there was a high χ^2/d.o.f. associated with a linear fit to three points in this dataset and that perhaps this was an indication of curvature. I investigate that possibility here, by fitting the data to a quadratic form. From quenched chiral perturbation theory this form is,

$$m_{\rm PS}^2 = a_{\rm PS} + b_{\rm PS}/\kappa + c_{\rm PS}/\kappa^2, \tag{3.3}$$

where logarithmic divergences have been ignored and the expression is written in terms of the hopping parameter since the extrapolation is to κ_c.

The linear and quadratic fits are shown in Figure 3.5. They strongly indicate that there are no curvature effects in this data. The linear function fits the six points extremely well. Also, the values of κ_c as determined linearly and quadratically agree, within errors. These are shown in Table 3.6. Finally, the coefficient of the quadratic term in Equation (3.3) is -0.1^{+2}_{-2}, confirming that the PCAC relation, $m_{\rm PS}^2 \propto mq$, is valid for the quark masses used here. The measured κ_c is, as expected, close to the tree-level prediction (in Table 3.6).

The Normal Quark Mass

It has been standard practice to use κ_c as the point to which masses are extrapolated and subsequently converted to physical values. At κ_c, it is assumed that

$m_u = m_d = 0$ *i.e.* $\kappa_u = \kappa_d = \kappa_c$. An alternative (and somewhat more intuitive) point to extrapolate to is the "normal" quark mass, κ_n. This is defined for degenerate u and d quarks at[1]

$$\frac{m_{\rm PS}}{m_V} = \frac{M_\pi}{M_\rho} = 0.172. \tag{3.4}$$

Therefore, κ_n corresponds to $m_n a$, the value of $m_q a$ which gives the physical value of M_π/M_ρ. This is determined from a fit of m_V to $m^2_{\rm PS}$, shown in Figure 3.5. Essentially masses are evaluated at the physical (non-zero) pion mass.

The values of κ_n from both a linear and a quadratic fit are also contained in Table 3.6. Both numbers agree within errors, as for κ_c. For the purposes of this chapter, all extrapolations are to κ_n, as determined from the linear fit. Using κ_n instead of κ_c should, of course, make little difference to the physics extracted from the lattice.

	Linear fit	Quadratic fit
$\tilde{\kappa}_c$	$0.12210^{+\ 1}_{-\ 1}$	$0.12213^{+\ 2}_{-\ 2}$
$\tilde{\kappa}_n$	$0.12206^{+\ 2}_{-\ 2}$	$0.12211^{+\ 3}_{-\ 2}$
$\kappa_{\rm crit} = 0.125$		

Table 3.6: The hopping parameter as determined by extrapolating $m^2_{\rm PS}$ to the critical quark mass and the normal quark mass for both linear and quadratic fits. $\kappa_{\rm crit}$ is the tree-level value.

3.3.2 Lattice masses at κ_n

Having determined the reference quark mass, $m_n a$, for this calculation, the next step is to evaluate the vector meson, nucleon and Δ masses at this point. The linear forms for these extrapolations have already been introduced (see Chapter 2). In this chapter, linear and quadratic fits are made to the data. I will describe each particle separately.

[1] I adopt the convention that masses denoted by, "M", refer to experimental quantities whereas, "m", refers to lattice values.

The ρ mass

The χ^2/d.o.f. = 0.2, from the linear fit is very low, indicating that Equation (2.10) is a good choice. It is not the case that the χ^2/d.o.f. is low simply because the errors are large. It is clear from Figure 3.5 that the statistical errors are small. For consistency and to check the value obtained from a linear fit, a quadratic fit is also done, using the form predicted by quenched chiral perturbation theory[2] [49]

$$m_V = a_V + b_V m_{\rm PS}^2 + c_V m_{\rm PS}^3 \tag{3.5}$$

This is shown, together with the linear fit, in Figure 3.5 and there is no appreciable difference between them. The extrapolated vector meson masses, obtained using Equations (2.10) and (3.5), are within errors and the coefficient of the quadratic term is -2^{+4}_{-4} : consistent with zero. Therefore it is assumed there are no higher order contributions (from $m_{\rm PS}^3$).

The verdict that linear fits are reasonable for mesons is not unexpected, since even for the 60 configurations used in Chapter 2, a good fit to the data is possible. A far more open issue is the baryon sector. This is now discussed but with just three masses the fits will be less reliable.

The nucleon mass

The natural first choice is to assume a linear dependence on quark mass and fit to Equation (2.11). For the full dataset used here, the χ^2/d.o.f. is reasonable : it is 1.72 compared with 1.94 when using just 60 configurations (and recall it was 5.0 for the SW-action). By eye, the data do seem to fit a straight line quite well. Assuming the quadratic form for baryon fit functions to be [49]

$$m_N = a_N + b_N m_{\rm PS}^2 + c_N m_{\rm PS}^3. \tag{3.6}$$

m_N is extracted from a quadratic fit. This is, however, unreliable, since with just three masses a χ^2/d.o.f. cannot be quoted. As noted in Chapter 2 and in [23]

[2]Once again contributions from logarithmic divergences have been neglected.

a linear fit of, $m_N^2 \, vs. \, m_q$, does give a lower χ^2/d.o.f., but the lack of theoretical justification makes it an unreasonable choice. Perhaps with more quark masses *i.e.* using non-degenerate baryons, the situation will become clearer, but for now values of m_N are quoted from the linear fit only.

The Δ mass

This extrapolation suffers from much the same problems as the nucleon case : with just three points it is difficult to pin down its behaviour. The χ^2/d.o.f. $= 1.61$ is slightly better than the nucleon but, on the other hand, the statistical errors are larger. A quadratic fit to the data, using Equation (3.6), gives a mass lower than the linear value, see Table 3.7. Since in Chapter 2 it was noted that the Δ mass was overestimated this could be interpreted as a curvature effect. However, only the linear value is considered here, for the same reasons as applied to the nucleon extrapolation.

All the extrapolated masses are collected in Table 3.7 and the extrapolations, both linear and quadratic, for each particle are in Figures 3.5 and 3.6.

	Linear fit	Quadratic fit
$m_{\rho\|\kappa_c}$	$0.290^{+\ 8}_{-\ 8}$	0.284^{+15}_{-15}
$m_{\rho\|\kappa_n}$	$0.293^{+\ 9}_{-\ 9}$	0.279^{+15}_{-15}
m_N	$0.385^{+10}_{-\ 9}$	0.367^{+19}_{-19}
m_Δ	0.481^{+10}_{-10}	0.464^{+31}_{-30}

Table 3.7: The extrapolated masses, evaluated at κ_n, of the ρ, nucleon and Δ for both linear and quadratic fits, in lattice units.

3.3.3 Interpolations

The method used to determine κ_s has already been described in Chapter 2. The range of quark masses, at which simulations were done, encompasses the strange quark mass and so it can be extracted by interpolation : an intrinsically more robust procedure than extrapolation. The errors quoted on interpolated quantities will, therefore, be lower than those on extrapolated quantities. Before presenting the masses of hadrons containing strange quarks, the dependence of κ_s on the

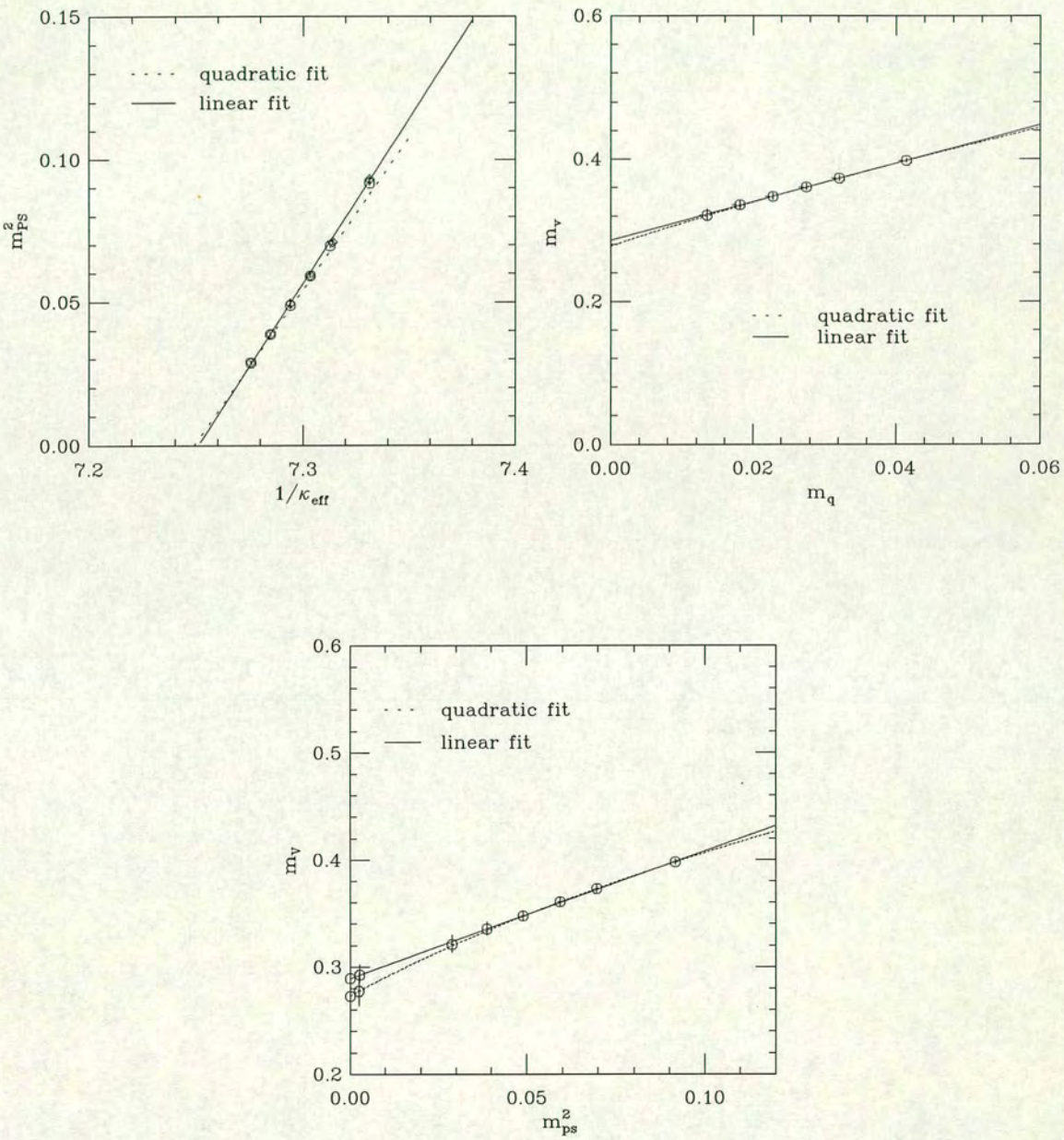

Figure 3.5: Extrapolations of pseudoscalar mass squared and the vector meson mass, to the critical and normal quark, for both linear and quadratic fits.

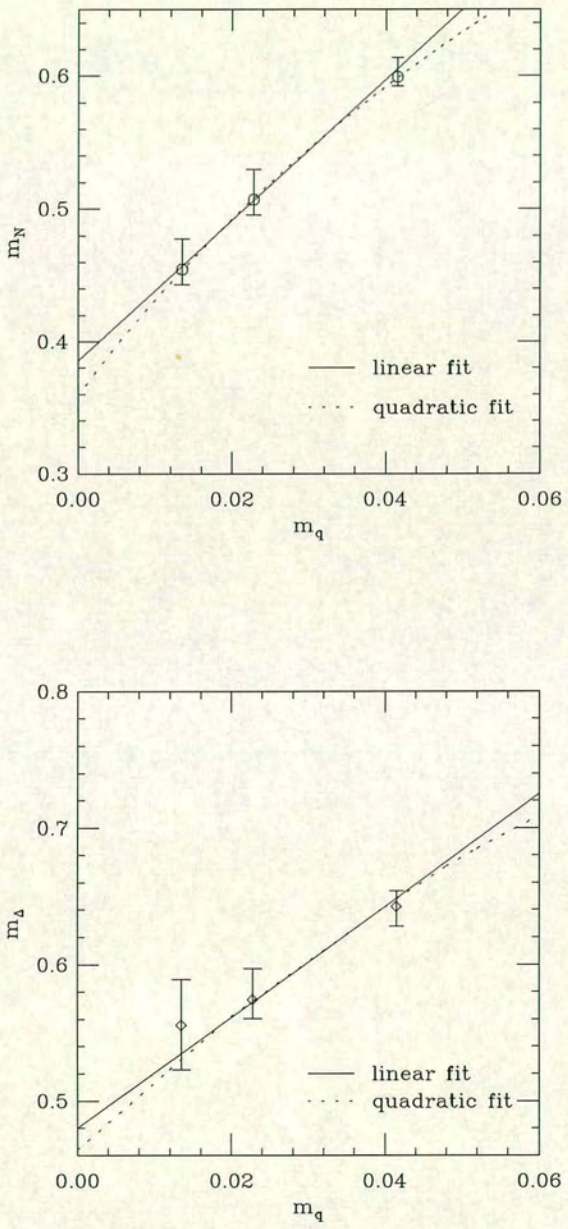

Figure 3.6: Extrapolations of the nucleon and Δ masses, for both linear and quadratic fits.

experimental input, used to determine it, is discussed.

3.3.4 Systematic errors in determining κ_s

A source of uncertainty in the calculation of κ_s and subsequently in strange-hadron masses, is the choice of experimental ratio used. In principle, one is free to choose the ratio of any strange hadron mass to the ρ mass, as input to the calculation. In [23] and [44], M_K^2/M_ρ^2 was used. The ambiguity involved in this choice has, until recently, been neglected. Here, I show that m_s can vary, by up to 20%, depending on the ratio used. This is illustrated in Table 3.8. The strange quark mass quoted in the final column is calculated from

$$m_s(a) = \frac{1}{2a}\left(\frac{1}{\kappa_s} - \frac{1}{\kappa_c}\right), \tag{3.7}$$

where the scale has been set using m_ρ. This change in κ_s with the input parameter

Ratio	κ_s	$\tilde{\kappa}_s$	m_s (MeV)
M_K^2/M_ρ^2	0.13656^{+9}_{-9}	0.12086^{+9}_{-9}	85.4
M_η^2/M_ρ^2	0.13666^{+7}_{-7}	0.12095^{+6}_{-6}	82.0
M_{K^*}/M_ρ	0.13638^{+15}_{-15}	0.12071^{+13}_{-13}	100.7
M_ϕ/M_ρ	0.13637^{+15}_{-15}	0.12070^{+13}_{-13}	101.1

Table 3.8: κ_s, determined using different mass ratios at $\beta = 6.2$.

has also been seen by other authors and at other β values [27]. I repeat the calculation of κ_s at $\beta = 5.7$, using different input ratios, two lattice volumes and two values of c_{sw}. The results are in Table 3.9. These results appear to show that the systematic error, in determining κ_s is independent of the lattice volume, the lattice spacing and c_{sw}. At this point, some ratio must be chosen with which to measure κ_s. In this chapter, I use M_K^2/M_ρ^2, which gives the highest number for κ_s (m_η is not considered since it is a theoretical prediction [47]). However, for many of the quantities measured, a value determined from the strange quark mass, fixed by M_ϕ/M_ρ, will also be given. This is at the lower end of possible values of κ_s,

$\beta = 5.7$					
Ratio	c_{sw}	Lattice	κ_s	$\tilde{\kappa}_s$	m_s (MeV)
M_K^2/M_ρ^2	$1/u_0^3$	$12^3 \times 32$	0.13977^{+7}_{-7}	0.12031^{+6}_{-6}	103.0
		$16^3 \times 32$	0.13984^{+11}_{-13}	0.12038^{+11}_{-11}	102.1
	1	$16^3 \times 32$	0.14931^{+10}_{-10}		106.8
M_η^2/M_ρ^2	$1/u_0^3$	$12^3 \times 32$	0.13991^{+7}_{-6}	0.12045^{+6}_{-6}	98.9
		$16^3 \times 32$	0.13998^{+10}_{-12}	0.12050^{+10}_{-10}	98.0
	1	$16^3 \times 32$	0.14945^{+11}_{-11}		102.8
M_{K^*}/M_ρ	$1/u_0^3$	$12^3 \times 32$	0.13918^{+12}_{-13}	0.11981^{+11}_{-11}	121.4
		$16^3 \times 32$	0.13935^{+34}_{-33}	0.11995^{+29}_{-29}	116.4
	1	$16^3 \times 32$	0.14864^{+25}_{-22}		125.8
M_ϕ/M_ρ	$1/u_0^3$	$12^3 \times 32$	0.13939^{+9}_{-9}	0.12000^{+8}_{-8}	115.3
		$16^3 \times 32$	0.13933^{+34}_{-33}	0.11994^{+22}_{-22}	117.0
	1	$16^3 \times 32$	0.14862^{+25}_{-22}		126.4

Table 3.9: κ_s, determined using different mass ratios at $\beta = 5.7$.

and together, these numbers indicate the spread of values due to this systematic error.

Table 3.10 contains the interpolated masses of the hadrons composed of one or more strange quarks, the quark content is also given.

The J Parameter

The parameter J can also be considered to be determined by interpolation. It is defined as [40]

$$J = m_{K^*} \frac{dm_V}{dm_{\rm PS}^2}. \tag{3.8}$$

Calculating J, using the highest and lowest value of κ_s, gives

$$J = 0.38^{+1}_{-1} \quad \text{from } M_K^2/M_\rho^2, \tag{3.9}$$

and

$$J = 0.37^{+2}_{-2} \quad \text{from } M_\phi/M_\rho. \tag{3.10}$$

	Quark Content	Mass in Lattice Units
m_η	PS : (κ_s, κ_s)	0.296^{+10}_{-10}
m_{K^*}	V : (κ_s, κ_c)	$0.332^{+\ 8}_{-\ 8}$
		$0.343^{+\ 9}_{-\ 8}$
m_ϕ	V (κ_s, κ_s)	$0.393^{+\ 8}_{-\ 9}$
m_Ω	Δ : (κ_s, κ_s)	$0.630^{+\ 7}_{-\ 7}$
		$0.647^{+\ 7}_{-\ 6}$
m_Σ	N : $\frac{1}{3}\left(\frac{1}{\kappa_s} + \frac{2}{\kappa_c}\right)$	$0.457^{+\ 8}_{-\ 8}$
		$0.461^{+\ 8}_{-\ 7}$
m_Ξ	N : $\frac{1}{3}\left(2\frac{1}{\kappa_s} + \frac{1}{\kappa_c}\right)$	$0.520^{+\ 7}_{-\ 7}$
		$0.535^{+\ 7}_{-\ 7}$

Table 3.10: The interpolated masses of hadrons containing at least one strange quark and determined from the input M_K^2/M_ρ^2 and alternatively from M_ϕ/M_ρ. For quantities where two masses are quoted, the first corresponds to fixing κ_s using M_K and the second to using M_ϕ. These interpolations were done using the linear fits described in the previous section. m_K is not included since it is an input parameter in this calculation.

These results are consistent with the lattice "world average" of 0.39 but there is still an approximately 20% discrepancy with the number derived from experimental data of $J = 0.48$. This will be investigated further at the end of this chapter.

3.4 The Edinburgh plot and the effect of high statistics

The Edinburgh plot is presented in Figure 3.7. The curve included in the plot is from a phenomenolgical quark-model prediction. It serves only to guide the eye, ratios of (unphysical) quark masses should not be expected to reproduce it. The mass ratios, am_N/am_V, are in Table 3.11.

For a small number of quark masses (as is the case in this baryon analysis), the Edinburgh plot is perhaps the best way to compare nucleon data at different lattice spacings, since it avoids a chiral extrapolation, which has been shown to be problematic. It should also be noted that it is not necessary to set the scale in this calculation, because mass ratios can be compared directly with those at different

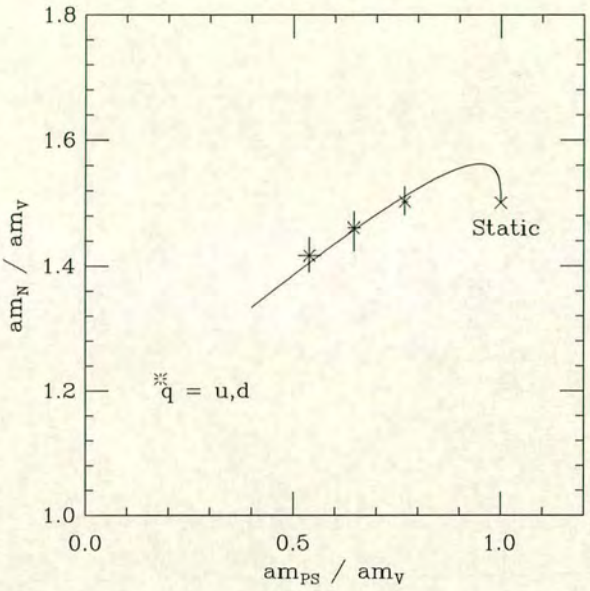

Figure 3.7: The nucleon-to-vector mass ratio at $\beta = 6.2$ for 220 gauge field configurations, using fuzzed data.

β and with experiment. Such a comparison is made at the end of this chapter, for $\beta \in [5.7, 6.0, 6.2]$. For now, however, only the $\beta = 6.2$ data is considered.

In Chapter 2, the Edinburgh plot was seen to be sensitive to tadpole improvement, albeit, only at the lightest quark mass. Fuzzed data was then introduced, on the same 60 configurations and some small effects were seen, again at $\kappa = 0.13745$. Increasing the statistics to 220 configurations, increases the nucleon-to-vector meson ratio, at all three κ values. In a comparison between β values, all three datasets are in good agreement, implying that the ratios in Table 3.11 are correct. It seems therefore, that ratios containing the nucleon mass, are reliably estimated in a high statistics calculation, incorporating fuzzing or smearing.

Figure 3.8 charts the change in the ratio, m_N/m_V, with changing clover coefficient, the introduction of fuzzing and the increase of statistics.

$\kappa_1 = \kappa_2$	m_N/m_V
0.13640	1.51^{+3}_{-2}
0.13710	1.46^{+3}_{-4}
0.13745	1.42^{+3}_{-3}
κ_n	1.33^{+4}_{-3}

Table 3.11: The nucleon-to-vector meson mass ratios at $\beta = 6.2$, for degenerate κ combinations. The ratio of nucleon and vector masses extrapolated to κ_n is also included.

3.5 A Comparison with Experiment

In this section, the lattice masses calculated in the previous section are converted to physical units and compared with experiment. Some quantities *i.e.* mass ratios can be compared directly, but for most, it is necessary to define a scale, relating the lattice and continuum schemes. This is addressed in the following subsection.

3.5.1 Setting the Scale

In any lattice calculation, the scale, a^{-1}, is set by inputting a single experimental mass and comparing this with its lattice value. All other massive quantities calculated on the lattice can be related to their continuum counterparts using this scale. These become the predictions of the theory. Although, in principle any massive quantity can be used as input, in practice, it is usually the ρ meson, or the string tension, as determined in an independent calculation *e.g.* [45]. Since different quantities are affected, to different levels, by discretisation and other systematic errors, the scale will not always be consistent in a given calculation. This can be seen in Table 3.12, which lists the different possible values of a^{-1} from this analysis. There is an $\approx 33\%$ difference between the highest and lowest values.
I note that a^{-1} determined from m_ρ is in good agreement with a^{-1} from $\sqrt{K}$, and I choose to set the scale in these calculations from m_ρ. Where possible, the need to set the scale was avoided by comparing ratios of lattice masses.

Quantity used to determine a^{-1}	a^{-1}
f_π	3.02^{+5}_{-4}
m_{K^*}	2.70^{+7}_{-7}
	2.60^{+6}_{-6}
m_ϕ	2.68^{+5}_{-5}
$(m_{K^*} - m_\rho)/(m_K^2 - m_\pi^2)$	2.00^{+9}_{-9}
	2.09^{+9}_{-9}
$m_{\rho_{\kappa_n}}$	2.63^{+8}_{-8}
$m_{\rho_{\kappa_c}}$	2.66^{+6}_{-6}
m_N	2.42^{+8}_{-7}
m_Δ	2.57^{+9}_{-9}
$\sqrt{K}$	2.73^{+5}_{-5}

Table 3.12: The scale for this lattice calculation, as set by various massive quantities, and compared with the scale from the string tension [45], $\sqrt{K}$. The two values quoted for $(m_{K^*} - m_\rho)/(m_K^2 - m_\pi^2)$, and m_{K^*} correspond to using values of κ_s, determined by fixing M_K and M_ϕ.

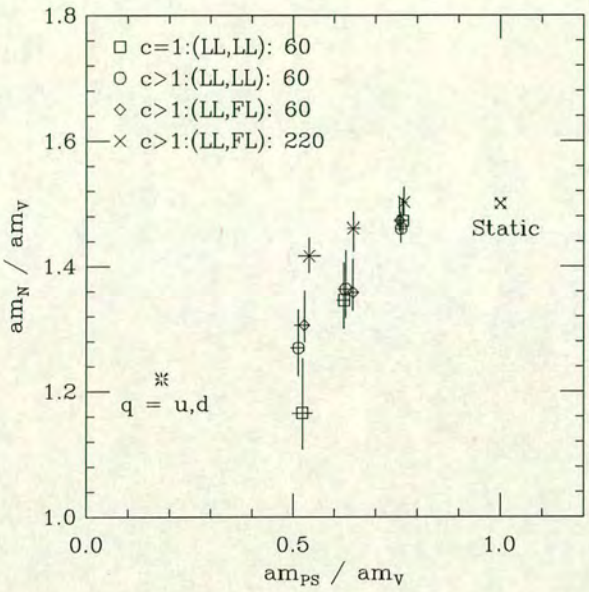

Figure 3.8: The Edinburgh plot at $\beta = 6.2$, using data at increasing levels of sophistication, as indicated on the plot. The benefits of high statistics and fuzzing are clear : not only are the errors reduced, but, as will be seen, the data are in extremely good agreement with results at $\beta = 5.7$ and 6.0.

3.5.2 The Hyperfine Splitting Revisited

The mass-splitting, $(m_V^2 - m_{\rm PS}^2)$, calculated using the full dataset and the best estimates of the vector and pseudoscalar masses, is shown in Figure 3.9. There is a disappointing lack of improvement in the slope : for comparison purposes the results obtained from the analysis of 60 configurations are also included. Although the measured values of $m_\rho^2 - m_\pi^2$ and $m_{K^*}^2 - m_K^2$ are in good agreement with experiment (see Table 3.13), the fall-off in slope is not seen experimentally. Indeed, the splitting remains approximately constant for heavier quarks, as noted in Chapter 2.

Following the discussion in §3.5.1, the hyperfine splitting is also plotted as a mass ratio *i.e.* $(m_V^2 - m_{\rm PS}^2)/m_K^2$ *vs.* $m_{\rm PS}^2/m_K^2$. This should highlight any errors in the previous plot resulting from setting the scale (using m_ρ). From Figure 3.10, it

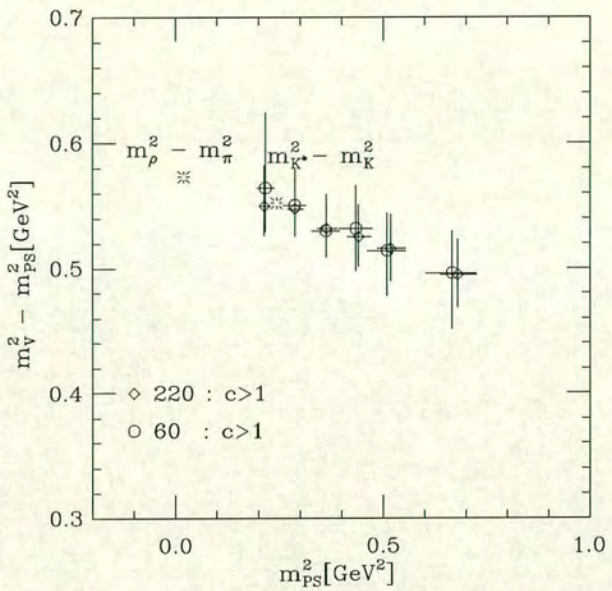

Figure 3.9: The hyperfine splitting, using all $\beta = 6.2$ gauge configurations and compared with that using a subset of 60.

appears these errors are negligible in this quantity : the trend is still a decreasing $(m_V^2 - m_{\rm PS}^2)$, with increasing quark mass. The slopes of both plots agree within the statistical errors,

$$\frac{d(m_V^2 - m_{\rm PS}^2)}{dm_{\rm PS}^2} = -0.15^{+2}_{-2}, \tag{3.11}$$

$$\frac{d((m_V^2 - m_{\rm PS}^2)/m_K^2)}{d(m_{\rm PS}^2/m_K^2)} = -0.12^{+3}_{-3}. \tag{3.12}$$

A final point is that an improvement in the slope of this quantity has been found on using a next-to-nearest-neighbour action, with improved gluonic and fermionic parts [46]. This was contrasted with a calculation using the Wilson action, where the result was similar to that found here.

Baryon Mass splitting

A tentative result for the spin-averaged, $(m_\Delta - m_N)$, splitting is presented in

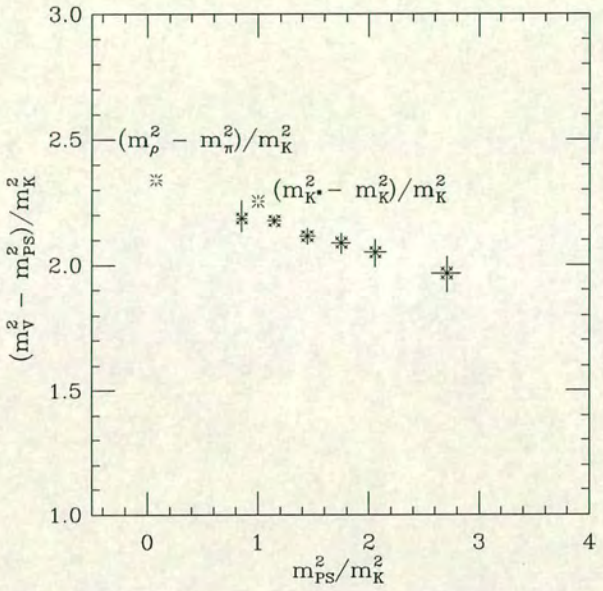

Figure 3.10: The hyperfine splitting using 220 gauge configurations. It is expressed as a mass ratio, to avoid errors in the scale, a^{-1}.

Figure 3.11. However, the errors are large and more quark masses are essential for a clearer picture. An analysis of non-degenerate baryon masses would be particularly useful here.

3.5.3 Hadronic Masses and Experiment

Table 3.13 lists the masses, mass splittings and mass ratios calculated in this chapter and compares them with experimental values. The lattice determinations of physical quantities are generally, in good agreement with experimental numbers. For masses composed of one or more strange quarks, the errors are purely statistical - no attempt has been made here, to include the systematic error, arising from the ambiguity in choosing an input mass for this calculation. Hadrons, containing strange quarks, are again determined by fixing both, $M_K^2/M_\rho^2 = 0.413$ and $M_\phi/M_\rho = 1.32$.

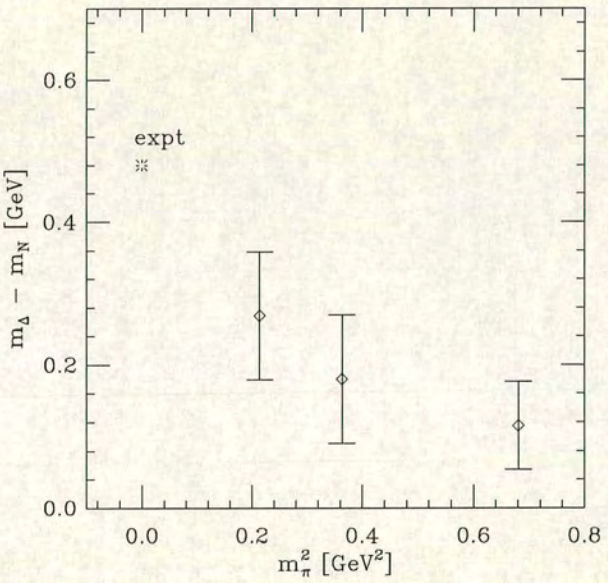

Figure 3.11: The spin-averaged splitting, $(m_\Delta - m_N)$ in physical units, using the three degenerate κ-combinations.

Physical quantity	Lattice value (MeV)	Expt (MeV)
m_η	726^{+8}_{-7}	"686"
	806^{+7}_{-7}	
m_{K^*}	883^{+5}_{-5}	892
	912^{+6}_{-5}	
m_ϕ	1045^{+8}_{-9}	1020
$m_\rho^2 - m_\pi^2$	0.566^{+2}_{-2} [GeV^2]	0.57 [GeV^2]
$m_{K^*}^2 - m_K^2$	0.543^{+2}_{-2} [GeV^2]	0.55 [GeV^2]
	0.568^{+3}_{-2} [GeV^2]	
m_N	1024^{+7}_{-7}	938
m_Δ	1277^{+12}_{-11}	1232
m_Ω	1676^{+3}_{-3}	1672
	1721^{+3}_{-3}	
m_Σ	1216^{+5}_{-5}	1190
	1226^{+6}_{-5}	
m_Ξ	1383^{+6}_{-6}	1315
	1423^{+6}_{-6}	
m_N/m_ρ	1.33^{+4}_{-3}	1.22
m_Σ/m_N	1.20^{+5}_{-4}	1.27
	1.21^{+5}_{-5}	
m_Ξ/m_N	1.35^{+4}_{-4}	1.40
	1.39^{+4}_{-4}	
$m_\Delta - m_N$	0.26^{+1}_{-1} [GeV]	0.48 [GeV]

Table 3.13: Light-hadron masses and mass ratios, in physical units, compared with experiment.

3.6 The Pseudoscalar and Vector Decay Constants

The pseudoscalar and vector decay constants are calculated using the ratios of correlators described in Chapter 2. Recall that the pseudoscalar decay constant is defined by the pion decay matrix element

$$\langle 0|\overline{q}\gamma_4\gamma_5 q|\pi\rangle = f_\pi m_\pi, \tag{3.13}$$

and that in the tadpole-improvement prescription this becomes,

$$\langle 0|\overline{\tilde{q}}\gamma_4\gamma_5\tilde{q}|\pi\rangle = 2\tilde{\kappa}Z_A\left\{1+\left(\frac{1}{2\tilde{\kappa}}-\frac{1}{2\tilde{\kappa_c}}\right)\right\}\times\langle 0|\overline{q}\gamma_4\gamma_5 q|\pi\rangle, \tag{3.14}$$

where the tilde on the quark fields indicates they have been improved by a rotation, such that

$$\tilde{q} = \sqrt{2\tilde{\kappa}}\left\{1+\frac{1}{2}\left(\frac{1}{2\tilde{\kappa}}-\frac{1}{2\tilde{\kappa_c}}\right)\right\}q. \tag{3.15}$$

The $\tilde{\kappa}$ notation is the same as in Chapter 1, where $\tilde{\kappa} = u_0\kappa$. The normalisation is such that the physical f_π, is 132MeV.

Similarly, the vector decay constant is defined by the matrix element

$$\langle 0|J_j^\mu(0)|V(p,\epsilon,j)\rangle = \epsilon_\mu\frac{m_V^2}{Z_V f_V}, \tag{3.16}$$

where ϵ_μ is the polarisation vector for the vector meson. The decay constants, $f_{\rm PS}$ and $1/f_V$, are then calculated from

$$\frac{\sum_{\mathbf{x}}\langle A_4(x,t)P^\dagger(0)\rangle}{\sum_{\mathbf{x}}\langle P(x,t)P^\dagger(0)\rangle} \sim \frac{f_{\rm PS}m_{\rm PS}}{Z_A\langle 0|P|P\rangle}\tanh\left(m_{\rm PS}\left(\frac{N_t}{2}-t\right)\right), \tag{3.17}$$

and

$$\sum_{j=1}^{3}\sum_{\mathbf{x}}\langle V_j(x,t)V_j^\dagger(0)\rangle \sim \frac{3m_V^3}{Z_V^2 f_V^2}\exp^{-m_V\frac{N_t}{2}}\cosh\left(m_V\left(\frac{N_t}{2}-t\right)\right). \tag{3.18}$$

3.6.1 Decay Constants in Lattice Units

Both f_π and $1/f_\rho$, are determined by extrapolation to the normal quark mass, $m_n a$. The decay constants, $f_K, 1/f_{K^*}$ and $1/f_\phi$ are subsequently determined by interpolation. The values of $f_{\rm PS}/Z_A$ and $1/(Z_V f_V)$, for the different κ combinations are in Table 3.14 and the extrapolation, $f_{\rm PS}$ *vs.* $m^2_{\rm PS}$ is shown in Figure 3.12. The decay constant, f_K, is determined by interpolation to $m^2_{\rm PS}(\kappa_n, \kappa_s)$. Considering the evidence in a previous section, that κ_s is not determined consistently, in a quenched lattice calculation, two values of f_K are presented : using the highest and lowest values of κ_s from Table 3.8. These lattice values are listed in Table 3.15.

κ_1, κ_2	$f_{\rm PS}/Z_A$	$1/(Z_V f_V)$
0.13640, 0.13640	0.0647^{+6}_{-6}	0.253^{+4}_{-4}
0.13710, 0.13640	0.0603^{+6}_{-6}	0.251^{+4}_{-4}
0.13710, 0.13710	0.0562^{+7}_{-7}	0.265^{+5}_{-6}
0.13745, 0.13640	0.0581^{+6}_{-6}	0.257^{+5}_{-5}
0.13745, 0.13710	0.0540^{+7}_{-7}	0.273^{+7}_{-8}
0.13745, 0.13745	0.0517^{+8}_{-8}	0.288^{+11}_{-11}

Table 3.14: The lattice values of the pseudoscalar and vector decay constants, for all κ combinations.

The vector decay constant is a dimensionless quantity, which can be compared directly with experiment. $1/f_\rho$ is extracted, by extrapolation to m_ρ at κ_n, from $1/f_V$, plotted as a function of m_V, By interpolation, the decay constants, $1/f_\phi$ and $1/f_{K^*}$ are determined. These values are listed in Table 3.16. Also included are the pseudoscalar decay constants in physical units, for which the scale is set using m_ρ.

The caveat of Chapter 2 still applies for the pseudoscalar case *i.e.* the uncertainty in the perturbative estimate of the current renormalisation constants makes it difficult to say how accurate the physical numbers, extracted from this calculation, are. The perturbative and non-perturbative values of Z_V are close (0.83 and

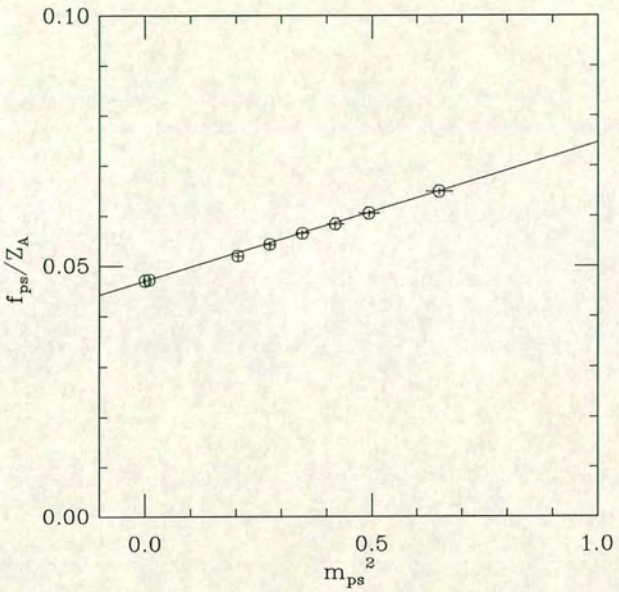

Figure 3.12: The extrapolation of $f_{\rm PS}$ in quark mass. The fit has a χ^2/d.o.f. = 1.5. The values of $f_{\rm PS}/Z_A$ at both κ_c and κ_n are included. These are barely distinguished.

$Z_A = 0.932$	
Quantity	Value in Lattice Units
f_π/Z_A	0.0468^{+7}_{-7}
f_π	0.0436^{+6}_{-5}
f_π/m_ρ	0.151^{+5}_{-4}
f_K	0.0513^{+10}_{-10}
	0.0503^{+7}_{-7}
f_K/f_π	1.18^{+2}_{-2}
	1.16^{+1}_{-1}

Table 3.15: Lattice values of the pseudoscalar decay constants and ratios, extracted from the extrapolation in Figure 3.12. For both f_K and f_K/f_π, the two values quoted correspond to calculations using the strange quark mass determined from the ratios, M_K^2/M_ρ^2 and M_ϕ/M_ρ. The renormalisation constant, Z_A is the perturbative estimate from [29].

0.817^{+10}_{-10} at $c_{sw} = 1$) so there is little cause for uncertainty there. However, recall that for the SW-action, the perturbative and non-perturbative values of Z_A, are 0.97 and 1.045 respectively. If the same trend were to be seen, in a non-perturbative measurement of Z_A, for the tadple-improved action used here, the physical numbers would be brought into good agreement with experiment.

$Z_A = 0.932$, $Z_V = 0.917$		
Quantity	Lattice Value	Expt
f_π	116^{+3}_{-4} [MeV]	132 [MeV]
f_π/m_ρ	0.151^{+5}_{-4} [MeV]	0.172
f_K	137^{+3}_{-3} [MeV]	160 [MeV]
	134^{+2}_{-2} [MeV]	
f_K/m_ρ	0.176^{+3}_{-3}	0.208
	0.172^{+3}_{-3}	
f_K/m_{K^*}	0.155^{+3}_{-3}	0.179
	0.147^{+3}_{-3}	
f_K/f_π	1.18^{+2}_{-2}	1.21
	1.16^{+1}_{-1}	
$1/f_\rho$	0.292^{+8}_{-8}	0.28
$1/f_{K^*}$	0.271^{+7}_{-7}	
	0.266^{+6}_{-6}	
$1/f_\phi$	0.248^{+5}_{-5}	0.23
	0.243^{+5}_{-4}	
$m_\phi/f_\phi m_\rho$	0.318^{+4}_{-3}	0.305
	0.311^{+4}_{-3}	

Table 3.16: The pseudoscalar and vector decay constants and ratios, compared with the experimental numbers. The scale has been set from m_ρ. $Z_V = 0.917$ is the perturbative value of the renormalisation constant.

That the pseudoscalar decay constants lie below the experimental numbers is not surprising, given the arguments in Chapter 2. It is encouraging though, that the ratio, f_K/f_π is in consistently good agreement with experiment.

The quantity, $f_{\rm PS}/m_V$, is compared with its experimental values in Figure 3.13.

The data seem to be constant with increasing quark mass. In [23] it was noted that the slope of this function was in close agreement with experiment but this is not the case here.

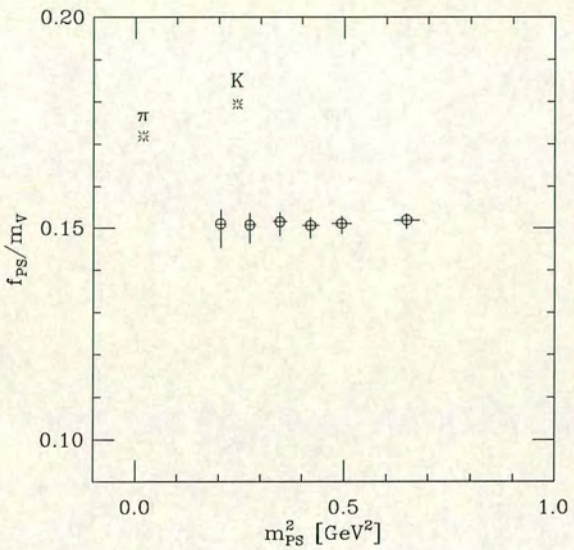

Figure 3.13: The quantity $f_{\rm PS}/m_V$, compared with experiment.

The final plot in this section is the extrapolation of the vector decay constant, $1/f_V \; vs. \; m_V$, in Figure 3.14. The important point here is that the values of $1/f_V$ are much closer to experiment than for the SW-action. The slope is in agreement with both experiment and the $c_{sw} = 1$ data. It appears to be unaffected by high statistics or fuzzing, unlike the pseudoscalar case. The vector decay constants, in this analysis, are larger than their experimental counterparts, a result which is puzzling, given the arguments of [32]. Since the statistical errors are small and Z_V is assumed to be accurate, this suggests that the effect of quenching the theory is subsumed by a larger systematic error, which tends to increase the value of $1/f_V$.

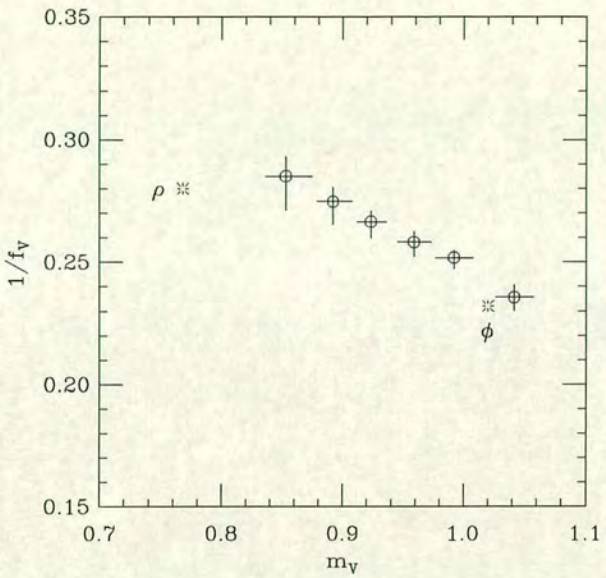

Figure 3.14: The extrapolation of $1/f_V$ in vector meson mass. The fit has a χ^2/d.o.f. = 1.3.

3.7 Summary of the Calculation at $\beta = 6.2$

The aim of this calculation is to reproduce the decay constants and the mass spectrum of light quarks as accurately as possible. Discretisation errors are reduced by using tadpole improvement and with high statistics the statisical errors are brought under control. The data are good enough to resolve κ_c and κ_n. The errors of the physical values quoted in Tables 3.13 and 3.16 are consistently between 1 and 3%. This control of the statistical effects in the data means that the systematic effects can be studied in more detail than was previously possible.

As already mentioned in Chapter 1, finite-size effects cannot be investigated, since only one lattice size is used. I note however, that in [48], a box-size greater than 2fm is recommended, when calculating nucleon masses. The box-size used here is $\approx$ 1.68fm which may explain some of the discrepancy between the calculated baryon masses and experiment. The nucleon, Δ and interpolated baryon masses are consistently larger than their experimental counterparts. Ratios of baryon

masses are, however, in better agreement.

A second source of systematic error arises from the interpolation to κ_s, which is not determined consistently. This effect is seen at different lattice spacings, different values of c_{sw} and different lattice volumes. The effects of this ambiguity propagate to physical quantities containing one or more strange quarks. Hadrons made from pure $s\bar{s}$ states, have the largest spread in value. An interesting situation arises for m_{K^*} : the largest and smallest values straddle the experimental number, making it unclear which, if any, of the values is "more" correct. This systematic effect does not seem to be as problematic for decay constants. In Table 3.16, the highest and lowest values of the relevant pseudoscalar and vector decay constants are quoted, and they agree within errors.

To summarise, lattice masses and decay constants are determined to an accuracy limited only by the inherent systematic effects, which it is now possible to probe. Investigating effects due to quenching the theory is difficult, without control of the other systematic effects and an equivalent simulation in the unquenched theory. In the next section, many quantities are seen to scale, but at values disagreeing with experiment, which may be an indication of quenching errors.

3.8 An Investigation of Scaling

The final section of Chapter 1 described the renormalisation group equation prediction, for the approach to the continuum *i.e.* $g(a) \to 0$ as $a \to 0$. In this regime, ratios of dimensionful quantities should be independent of the coupling. Using data at three values of the lattice spacing, this prediction is tested for the non-strange hadrons, the kaon system and the pseudoscalar decay constants.

3.8.1 Lattice details at different β values

The couplings at which simulations have been done correspond to : $\beta = 5.7, 6.0$ and 6.2. The simulation at $\beta = 6.2$ has already been described (see Table 3.1). At $\beta = 5.7$, the dataset comprises 142 gauge field configurations on a $16^3 \times 32$ lattice. Jacobi-smeared, quark propagators are generated at two κ values and for two values of c_{sw} : $c_{sw} = 1$ and $c_{sw} = 1/u_0^3$. The $\beta = 6.0$ data is generated at

$c_{sw} = 1/u_0^3$ only. Fuzzed propagators at three κ values on 499, $16^3 \times 48$, gauge field configurations are used. The lightest quark mass, at $\beta = 6.0$, has not been fuzzed and for this reason is not included in the Edinburgh plot.

3.8.2 The ρ mass

The mass of the ρ meson at each coupling is evaluated at κ_n, as described previously. Increasing the value of c_{sw} from 1, to $1/u_0^3$, decreases the dependence of $m_\rho/\sqrt{K}$ on the lattice spacing, although this is not completely removed. This is shown in Figure 3.15. For comparison, values of $m_\rho/\sqrt{K}$ at $c_{sw} = 0$, published by the GF11 Collaboration [34] are also included. On comparing these with the $c_{sw} = 1/u_0^3$ data, the trend is clearly towards improved scaling.

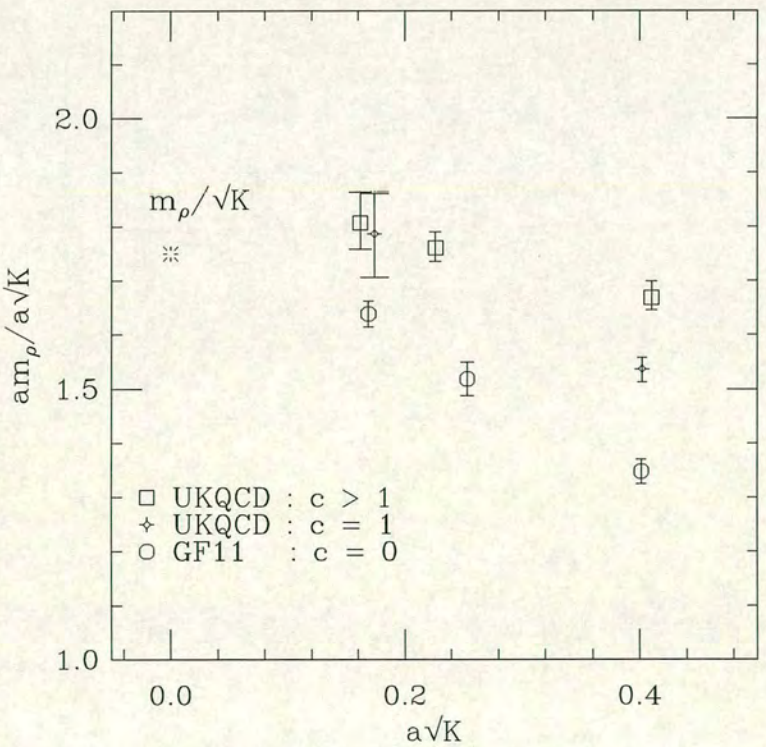

Figure 3.15: am_ρ in units of the string tension, for three β values and for different values of c_{sw}.

3.8.3 The Edinburgh Plot

The nucleon-to-vector meson ratio shows a similarly improved scaling behaviour for $c_{sw} = 1/u_0^3$. As shown in Figure 3.16, data at all three couplings are in good agreement. Only the tadpole-improved data is shown here since the behaviour of the nucleon-vector meson ratio with increasing c_{sw}, at $\beta = 6.2$, has already been shown in Figure 3.8. An interesting point, however, is that while the data at $\beta = 6.2$ increase, (towards the phenomenological curve) with increasing c_{sw} ; at $\beta = 5.7$ the trend is in the opposite direction, decreasing with increasing c_{sw}.

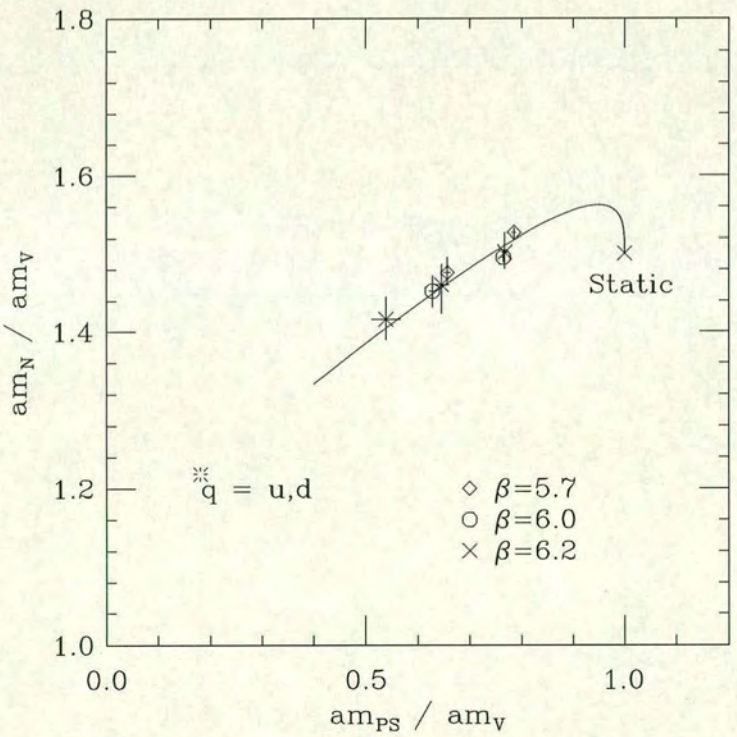

Figure 3.16: The Edinburgh plot, showing that the nucleon-to-vector meson ratio scales for $c_{sw} = 1/u_0^3$.

3.8.4 Vector-Pseudoscalar Mass-splitting

The hyperfine splitting is plotted for all three couplings analysed, in Figure 3.17. There is a remarkable lack of change, for different couplings and for increasing c_{sw}. This suggests that other errors are dominant. Although the results extrapolate to the physical values of both $(m_\rho^2 - m_\pi^2)/m_K^2$ and $(m_{K^*}^2 - m_K^2)/m_K^2$ the worry is the decreasing trend for increasing quark mass and the implications this has for the charmonium system, where $(m_V^2 - m_{\rm PS}^2)/m_K^2 \approx 2.94\,[\mathrm{GeV}^2]$

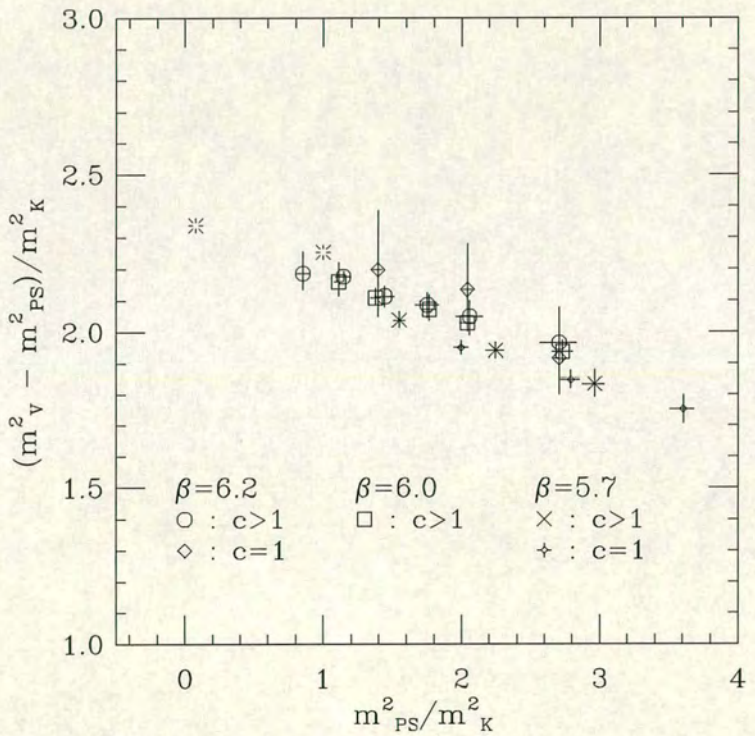

Figure 3.17: Vector-pseudoscalar mass splittings at all β and c_{sw} values.

3.8.5 The Kaon System

The strange quark mass is determined by fixing any one of, $m_K/m_\rho, m_\phi/m_\rho$ or m_{K^*}/m_ρ. However, as was discussed in §3.3.4, the choice of ratio affects the final value of κ_s quite strongly. In Figure 3.18, the ratio m_{K^*}/m_ρ, is calculated by fixing κ_s, from M_K/M_ρ and then from M_ϕ/M_ρ. The data show that m_{K^*} scales with m_ρ, for all values of c_{sw}, but cannot be consistently determined within the quenched approximation. The parameter, J behaves in a similar way. It scales

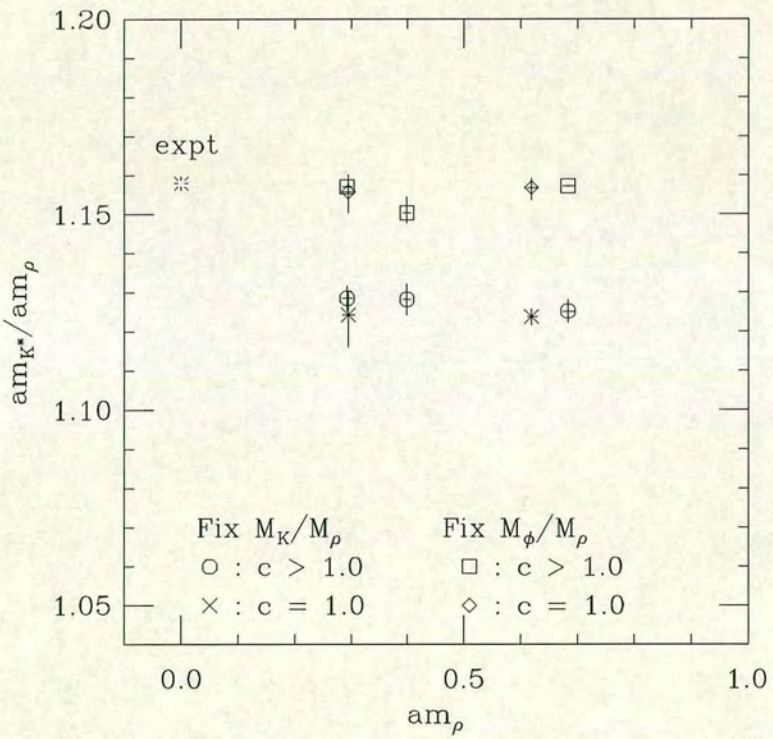

Figure 3.18: Determining m_{K^*}/m_ρ, using M_K and alternatively M_ϕ, as input to the calculation.

with m_ρ for the values of c_{sw} considered here, but again at a value below the experimental number. This is shown in Figure 3.19, it has been determined by fixing, M_K^2/M_ρ^2.

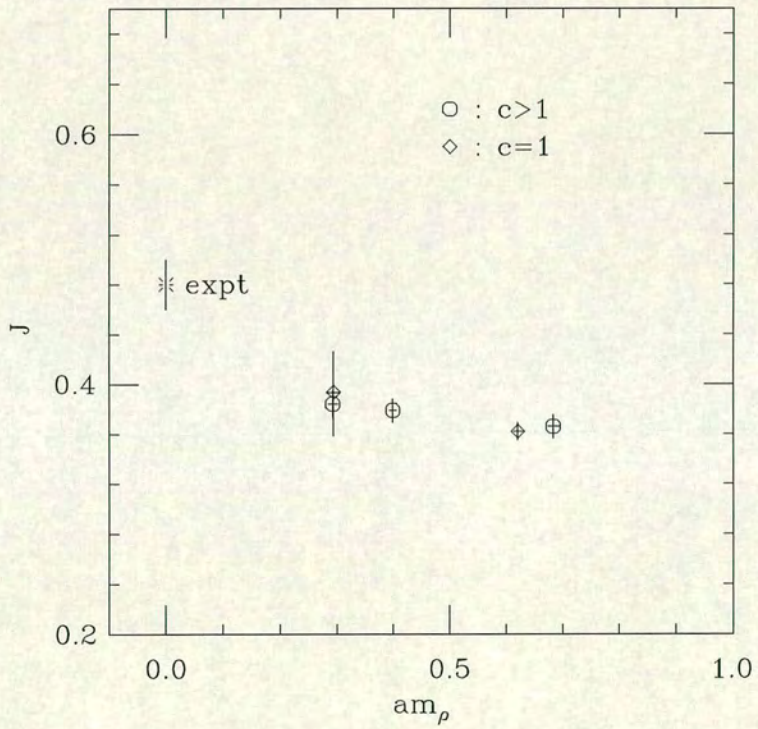

Figure 3.19: J, scaling for all c_{sw} and β values. It is been determined here, by fixing the ratio M_K^2/M_ρ^2.

3.8.6 The Pseudoscalar Decay Constants

The first quantity considered is, f_π/m_ρ. As already pointed out, the accurate determination of $f_{\rm PS}$ is complicated by errors inherent in the calculation of the current renormalisation constant. However, using the same procedure at all β values (described in Chapter 2 and § 3.6) it appears that scaling may set in at $\beta \geq 6.0$. This is illustrated by Figure 3.20. The trend here agrees with that seen at $c_{sw} = 0$, in [34]. Considering now the ratio, f_K/f_π, the situation is somewhat

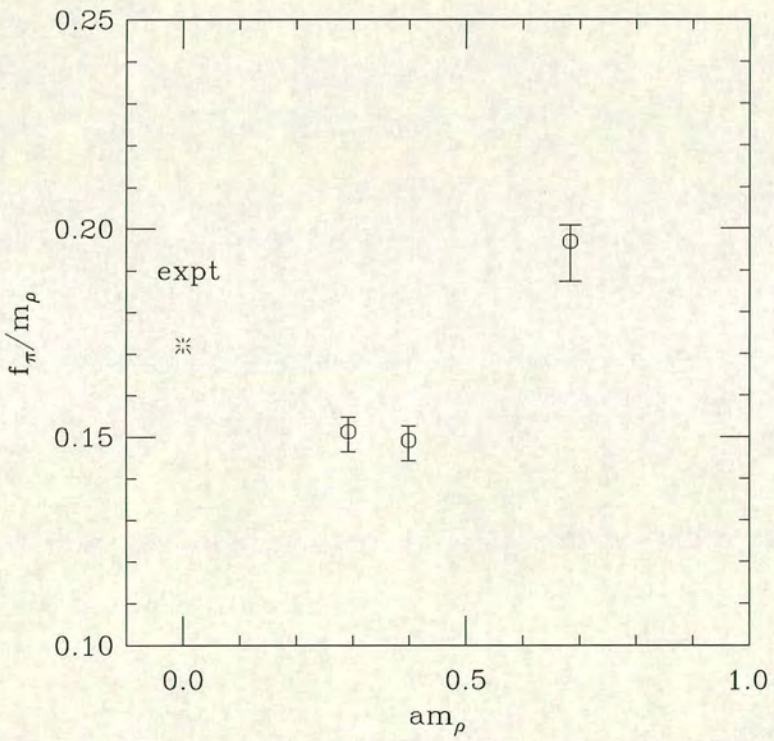

Figure 3.20: The ratio of the pseudoscalar decay constant to the vector meson mass. Scaling sets in at $\beta \geq 6.0$.

improved. Recall that this ratio is independent of Z_A and has been shown to agree within errors, with experiment, at $\beta = 6.2$, for two values of c_{sw}. Once again, the behaviour with β appears to be independent of c_{sw} (at $\beta = 6.2$ and 5.7, both $c_{sw} = 1$ and $c_{sw} = 1/u_0^3$ are determined). For $\beta \geq 6.0$, the ratios scale and within

errors, agree with the experimental number. At $\beta = 5.7$, there is a remaining dependence on the lattice spacing. The ratio, f_K/f_π as a function of the string tension is in Figure 3.21. The values of the string tension, $a\sqrt{K}$, used at different

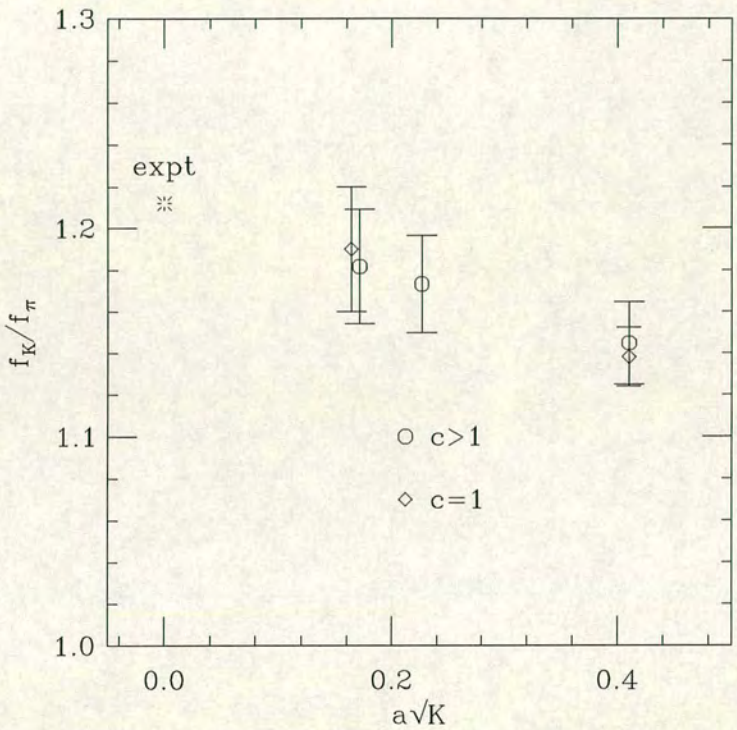

Figure 3.21: The ratio of f_K to f_π. This scales at $\beta \geq 6.0$ and there is a dependence on the lattice spacing at $\beta = 5.7$.

β values, are from [45],

$$\beta = 5.7 \quad : \quad a\sqrt{K} = 0.4099(24), \tag{3.19}$$

$$\beta = 6.0 \quad : \quad a\sqrt{K} = 0.2265(55), \tag{3.20}$$

$$\beta = 6.2 \quad : \quad a\sqrt{K} = 0.1619(19). \tag{3.21}$$

In Table 3.17, the values of the extrapolated mass ratios and J used in Figures 3.15 to 3.21, at the different couplings used, are listed.

Quantity	β	Lattice value
$am_\rho/a\sqrt{K}$	5.7	1.67^{+3}_{-2}
	6.0	1.8^{+3}_{-3}
	6.2	1.8^{+6}_{-5}
am_{K^*}/am_ρ	5.7	1.13^{+1}_{-1}
(fixing M_K/M_ρ)	6.0	1.128^{+7}_{-6}
	6.2	1.129^{+9}_{-7}
am_{K^*}/am_ρ	5.7	1.157^{+13}_{-9}
(fixing M_ϕ/M_ρ)	6.0	1.150^{+7}_{-6}
	6.2	1.157^{+9}_{-8}
J	5.7	0.366^{+12}_{-9}
	6.0	0.379^{+7}_{-6}
	6.2	0.384^{+9}_{-8}
f_π/m_ρ	5.7	0.197^{+4}_{-8}
	6.0	0.149^{+4}_{-5}
	6.2	0.151^{+4}_{-5}
f_K/f_π	5.7	1.15^{+2}_{-1}
	6.0	1.17^{+2}_{-2}
	6.2	1.18^{+3}_{-1}

Table 3.17: Extrapolated mass ratios and J, at three values of the coupling. These data are shown in Figures 3.15 to 3.21. The values of f_K used in this analysis are calculated by fixing M_K.

3.8.7 Continuum Extrapolations

The quantities considered in this section are extrapolated to their continuum ($a \longrightarrow 0$) limit, using uncorrelated fits. Most of the data seem to suggest a linear dependence on the lattice spacing. However, quadratic fits are also done to test the nature of the lattice spacing dependence. A χ^2/d.o.f. cannot be quoted for these fits because only three points are used. The coefficient of the quadratic term is small and when the low χ^2/d.o.f. of the linear fits is considered, a linear dependence on the lattice spacing appears likely. In Table 3.18, the results from both linear and quadratic fits are included. In general, the linear results are in better agreement with experiment, with smaller errors.

Physical Quantity	Fitting Range	Quadratic Coefficient	Lattice (quadratic) (MeV)	Lattice (linear) (MeV)	Expt (MeV)
$m_\rho/a\sqrt{K}$	$\beta \geq 5.7$	1^{+5}_{-5}	2.0^{+4}_{-4}	1.89^{+6}_{-6}	1.75
m_{K^*}/m_ρ	$\beta \geq 5.7$	0.05^{+28}_{-29}	1.12^{+4}_{-5}	1.131^{+6}_{-5}	1.158
J	$\beta \geq 5.7$	0.02^{+73}_{-73}	0.39^{+1}_{-1}	0.40^{+2}_{-2}	0.48
f_π/m_ρ	$\beta \geq 6.0$			1.51^{+2}_{-3}	0.172
f_K/f_π	$\beta \geq 6.0$			1.18^{+1}_{-1}	1.21
	$\beta \geq 5.7$	0.83^{+73}_{-70}	1.14^{+2}_{-2}	1.20^{+4}_{-4}	

Table 3.18: The lattice mass ratios and the parameter J, extrapolated to $a = 0$, using linear and quadratic fits. The results are compared with experiment. The χ^2/d.o.f. of the linear fits is between 0.00006 (for J) and 0.04 (for $am_\rho/a\sqrt{K}$).

3.8.8 Summary

A number of physical quantities are compared, at three values of the coupling. For spectral quantities there is evidence of scaling at $\beta \geq 5.7$. The introduction of tadpole-improvement reduces the dependence on the lattice spacing, especially

at $\beta = 5.7$. This is particularly obvious in Figure 3.15, where data at three values of c_{sw} are included. The Edinburgh plot also shows an improvement in scaling : for $c_{sw} = 1$, the ratios of nucleon-to-vector meson mass, at $\beta = 6.2$ and 5.7, do not agree, but for $c_{sw} > 1$ there is very good agreement. The scaling behaviour of masses and mass ratios in the kaon system appears to be independent of tadpole-improvement and the ambiguity in determining the strange quark mass, makes these quantities inconsistent with experiment.

The decay constants at $\beta \geq 6.0$ appear to be independent of a. Below this, at $\beta = 5.7$ the data do not scale, although the a-dependence is quite weak for the ratio, f_K/f_π.

Chapter 4

Soft Covariant Gauges in Lattice QCD

This chapter investigates a covariant, non-perturbative, gauge-fixing prescription for lattice gauge theories. In principle, the method eliminates the Gribov problem [50]. A smooth, one-parameter family of gauges is defined, using which the gauge dependence of quantities such as quark and gluon propagators can be studied. The origins of this method, in continuum QCD, are described and its lattice form is explained. The efficiency of the algorithm designed to implement the gauge-fixing numerically is tested. An initial study of the gauge dependence of the gluon propagator is done.

4.1 Motivation

The previous chapters have focused mainly on the successes of Lattice QCD in calculating physical *i.e.* gauge-invariant observables. This is a vast area in which lattice gauge theory has proved an invaluable tool.

Consider again however, the motivation for Wilson's initial formulation of Lattice QCD : it was to find evidence, non-perturbatively, that confinement is a feature of QCD. Although a thorough understanding and precision measurements of the bound states of quarks (*i.e.* hadrons) cannot but lend support to this concept, the quark and gluon propagators themselves, are expected to contain the most relevant information, since they are the fundamental quantities of the theory.

These propagators are also useful in their own right : quark and gluon states have been used in a first principles calculation of the QCD running coupling, α_s [65] ; quark states have been used in a non-perturbative determination of renormalisation constants [66] and finally, it has recently been shown that a non-perturbative evaluation of the clover coefficient using a Schrödinger functional on

quark states [67] is possible.

Unlike hadronic quantities, quark and gluon Green functions are gauge dependent and must be calculated in a fixed gauge. Traditionally this has been the Landau gauge. It is nonetheless, important to monitor the gauge dependence of these quantities and, if possible, disentangle any gauge-independent features from the gauge-dependent behaviour.

4.2 A Continuum Quantisation

In Chapter 1, the Faddeev-Popov quantisation was sketched. Gribov [50] showed that fixing the divergence in Equation (1.54) in this way does not uniquely fix the gauge, at a non-perturbative level. Therefore, the gauge-fixing condition

$$\partial_\mu A^\mu(x) = 0, \tag{4.1}$$

may have more than one solution. These are the Gribov copies - multiple configurations on a gauge orbit, related through a gauge transformation and all satisfying the gauge constraint. This means that, given some $A_\mu(x)$, a gauge transformation, g, can be found, such that $A^g_\mu(x)$ also satisfies the gauge-fixing condition above, where $A^g_\mu(x)$ is the gauge-transformed field,

$$A^g_\mu(x) = g(x)A_\mu(x)g^{-1}(x) + g(x)\partial_\mu g^{-1}(x). \tag{4.2}$$

This implies that the Faddeev-Popov determinant, $\det \mathrm{FP}$, introduced through a change of variables in the gauge-fixing procedure, is not positive definite. By imposing an additional gauge-fixing condition, restricting the range of integration, Gribov showed that the number of gauge degrees of freedom is reduced. The conditions are

$$\partial_\mu A^\mu(x) = 0 \quad \text{and} \quad \det \mathrm{FP} > 0. \tag{4.3}$$

Defining Γ, as the set of all $A_\mu(x)$ satisfying, $\partial_\mu A^\mu(x) = 0$, the above conditions define a convex subset of Γ, called Ω. This is known as minimal Landau gauge. It has been shown that every gauge orbit passes through Ω, rendering the full

set, Γ, redundant. These conditions select a local minimum of the action when using a minimisation algorithm. However, since the existence of a unique absolute minimum on the gauge orbit has not been proven there are still Gribov copies in this gauge. The gauge-fixing conditions of Equation (4.3) do however, form the basis of a stochastic quantisation procedure, which avoids the Gribov issue.

A quantisation scheme proposed in [52] for continuum QCD, is used. The path integral

$$Z = \int DA_\mu(x)\, \exp^{-S_{\rm YM}[A]}, \tag{4.4}$$

is modified by inserting a factor of unity, thereby ensuring that gauge-invariant quantities are unaffected. The result is

$$Z_{\rm mod} = \int DA_\mu(x) \exp^{-S_{\rm YM}(A_\mu(x))} \int Dg \exp^{\xi(A^g_\mu(x))} \mathcal{I}^{-1}(A_\mu(x)), \tag{4.5}$$

where $S_{\rm YM}$ is the Yang-Mills action. $\xi(A^g_\mu(x))$ can be any gauge-dependent function of $A_\mu(x)$, with the only constraint being that the integral $\mathcal{I}(A_\mu(x))$, defined as

$$\mathcal{I}(A_\mu(x)) = \int Dg \exp^{\xi(A^g_\mu(x))}, \tag{4.6}$$

exists. This means the integral, $\mathcal{I}$, is a gauge-invariant functional. Using the gauge-invariance of the Yang-Mills action, the Haar measure and $\mathcal{I}(A_\mu(x))$, the gauge group integration can be factored out and Equation (4.5) is written

$$Z_{\rm mod} = \int Dg \int DA_\mu(x)\, \exp^{-S_{\rm YM}(A^g_\mu(x))} \exp^{\xi(A^g_\mu(x))} \mathcal{I}^{-1}(A_\mu(x)). \tag{4.7}$$

A simple change of variables: $A^g \to A' = A$, for which the Jacobian is one, means the integrand is independent of g and the path-integral is

$$Z_{\rm mod} = \int Dg \int DA_\mu(x) \exp^{-S_{\rm YM}(A_\mu(x))} \exp^{\xi(A_\mu(x))} \mathcal{I}^{-1}(A_\mu(x)). \tag{4.8}$$

The volume of the gauge group, $\int Dg$, is finite and can be absorbed by a change

of the normalisation constant (suppressed here for clarity), to give

$$Z_{\text{mod}} = \int DA_\mu(x) \exp^{-S_{\text{YM}}(A_\mu(x))} \exp^{\xi(A_\mu(x))} \mathcal{I}^{-1}(A_\mu(x)). \tag{4.9}$$

A gauge-dependent weight factor has been introduced, as has a gauge-invariant functional, $\mathcal{I}(A_\mu(x))$, without approximation or assumption. This creates a normalised probability distribution on the gauge orbit and the Gribov issue has been avoided by this globally correct, gauge-fixing procedure.

4.3 A Lattice Quantisation

It has been shown [54] that Gribov copies also exist when Landau gauge is numerically implemented on a lattice via a minimisation prescription. This has consequences for gauge-dependent quantities and the Monte Carlo algorithms used to study them, since even the definition of, *e.g.* the gluon propagator, may depend on the somehow "preferred" Gribov copy which is selected.

The generalised path-integral in Equation (4.9) can be expressed as a lattice quantity. Using the theory, developed in Chapter 1, to move from the continuum to the lattice, the equivalent of the continuum path-integral in Equation 4.9 is

$$Z_{\text{lat}} = \int DU \ \exp^{-\beta S_W[U]} \exp^{-\beta \xi_{\text{lat}}[U]} \mathcal{I}_{\text{lat}}^{-1}[U], \tag{4.10}$$

where $\beta = N/g^2$, S_W is the standard Wilson gauge action derived in Chapter 1 and DU is the Haar measure. The gauge-invariant functional integral on the lattice gauge group is

$$\mathcal{I}_{\text{lat}}[U] = \int Dg \exp^{-\beta \xi_{\text{lat}}[U^g]}, \tag{4.11}$$

and in the usual way, U^g is the gauge-transformed link, under a local gauge transformation, g

$$U_\mu^g(x) = g(x) U_\mu(x) g^\dagger(x + \hat{\mu}). \tag{4.12}$$

4.3.1 Choosing the gauge

At this point, the gauge-fixing term, ξ, must be specified, to allow the integral $\mathcal{I}$ to be evaluated explicitly. Choosing ξ is not trivial, since it is here that the Gribov ambiguity can arise. The choice is made with regard to arguments in the continuum theory and it is subsequently redefined on the lattice. As already mentioned the choice is restricted by the necessary existence of the integral $\mathcal{I}$. A clear example of the consideration which must be given is illustrated by the following :

Consider the choice

$$\xi(A^g_\mu(x)) = -M^2||\partial A^g(x)||^2, \tag{4.13}$$

and consider evaluating $\mathcal{I}(A_\mu(x))$ via a saddle-point approximation by taking $M^2 \longrightarrow \infty$. It is assumed that the gauge-fixing term attains a unique absolute minimum on each gauge orbit[1]. In Landau gauge, all Gribov copies will satisfy $\partial A^g(x) = 0$ and so will be absolute minima of $\mathcal{I}(A_\mu(x))$. Clearly this is not a tenable situation.

An argument by Zwanziger suggests that a good choice is

$$\xi(A_\mu(x)) = -M^2||A^g||^2. \tag{4.14}$$

He has shown that the subset, Ω forms the locus of all minima of the functional, $F_A(g) = ||A^g||^2$, for arbitrary $A_\mu(x)$. So that every gauge orbit passes through Ω and, $F_A(g)$ defined on the gauge orbit, A_μ, achieves its minimum. In other words, $||A^g||^2$ has an absolute minimum and so no minimising sequence should run to ∞. This choice was proposed as a solution to the Gribov problem in Landau gauge. It satisfies the gauge constraints suggested by Gribov and can be formally evaluated by taking $M^2 \longrightarrow \infty$ and using a saddle-point approximation. The parameter M^2 is a free gauge-parameter with dimensions of a mass squared. Thus the limit of this scheme is for $M^2 \longrightarrow \infty$ *i.e.* the minimal Landau gauge.

[1]This is a necessary condition for ergodic sampling in a Monte Carlo algorithm.

4.3.2 The lattice gauge-fixing term

Equation (4.14) is easily re-expressed in lattice language, using the technology developed in Chapter 1

$$\begin{aligned} \xi[U^g_\mu(x)] &= M^2 F_{\rm lat}[U^g], \\ &\text{with} \\ F_{\rm lat}[U^g] &= \sum_{n,\mu} \Re\mathrm{eTr}[U^g_\mu(n)]. \end{aligned} \tag{4.15}$$

A second advantage of this choice is now clear. On the lattice, it has a simple, 1-link form. It acts as an effective Hamiltonian with nearest-neighbour interaction of the variables $g(n)$, the group elements, coupled through the links, $U_\mu(x)$. The lattice quantising path-integral can then be explicitly written

$$Z_{\rm lat} = \int DU \, \exp^{-\beta S_W[U]} \exp^{-\beta M^2 F_{\rm lat}[U]} \mathcal{I}^{-1}_{\rm lat}[U]. \tag{4.16}$$

4.4 The Lattice Gauge-Fixing Procedure

A stochastic gauge-fixing procedure to calculate the vacuum expectation values of gauge-dependent quantities is now defined using the above methodology[2] . Starting with the usual gauge-invariant Wilson formalism, where

$$Z_W \equiv \int DU \, \exp^{-\beta S_W[U]}, \tag{4.17}$$

the expression for the expectation value of an observable, $\mathcal{O}$ is

$$\langle \mathcal{O} \rangle_W = Z_W^{-1} \int DU \exp^{-\beta S_W[U]} \mathcal{O}[U]. \tag{4.18}$$

Using Elitzur's theorem, if $\mathcal{O}[U]$ is a local, gauge-dependent function the above expectation value is zero. This motivates a redefinition of the path-integral. In-

[2]From this point all expressions refer to lattice quantities, unless otherwise stated, so the subscript "lat" will be dropped.

spired by the quantisation described in the previous section, the path-integral is modified by inserting a factor of unity (shown in bold type),

$$Z_{\rm mod} \equiv \int DU \, \exp^{-\beta S_W[U]} \int \boldsymbol{Dg \mathcal{I}^{-1}[U] \exp^{-\beta M^2 F[U^g]}} \, , \qquad (4.19)$$

$S_W[U]$ and $\mathcal{I}$ are defined in §4.3 and $F[U^g]$ is the gauge-fixing functional defined by Equation (4.15). Clearly, $Z_{\rm mod} = Z_W$, but with this new expression, the expectation value of a gauge-dependent, $\mathcal{O}[U]$, is non-zero,

$$\langle \mathcal{O} \rangle_{\rm mod} = Z_{\rm mod}^{-1} \int DU \, \exp^{-\beta S_W[U]} \mathcal{I}^{-1}[U] \int Dg \, \exp^{-\beta M^2 F[U^g]} \mathcal{O}[U^g]. \qquad (4.20)$$

To express this more clearly, the gauge-invariant average over the lattice sites, $g(n)$ is defined as

$$\langle \mathcal{O}[U] \rangle_G \equiv \mathcal{I}^{-1}[U] \int Dg \exp^{-\beta M^2 F[U^g]} \mathcal{O}[U^g], \qquad (4.21)$$

and so

$$\begin{aligned} \langle \mathcal{O} \rangle_{\rm mod} &= \frac{\int DU \, \exp^{-\beta S_W[U]} \langle \mathcal{O}[U] \rangle_G}{\int DU \, \exp^{-\beta S_W[U]}}, \\ &= \langle \, \langle \, \mathcal{O}[U] \, \rangle_G \, \rangle_W . \end{aligned} \qquad (4.22)$$

where $\langle \, \rangle_W$ represents the Wilson average in configuration space.

Essentially then, the expectation value of any gauge-dependent quantity is calculated as two averages. The first average forms a gauge-invariant function, $\langle \, \mathcal{O}[U] \, \rangle_G$, from the gauge-dependent, $\mathcal{O}[U]$. The average is over the gauge group with a weight, $\exp^{-\beta M^2 F[U^g]}$. Secondly, the $\langle \, \mathcal{O}[U] \, \rangle_G$, are averaged in the space of link configurations weighted in the usual way by the Wilson term, $\exp^{-\beta S_W[U]}$.

It is important to note that if $\mathcal{O}[U]$ is a gauge-invariant quantity, the Wilson form of the expectation value is recovered, as required by consistency. The gauge-invariance of the Haar measure, $\mathcal{I}$ and the Wilson action allow a gauge transformation to be used, to factor out the group volume. Equation (4.19) can then

be cast in the form of Equation (4.10). Observables measured using this gauge-fixing, have as their $M^2 \longrightarrow \infty$ limit the minimal Landau gauge value and this is included in the results presented. For lattice simulations, the minimal Landau gauge is approximated by imposing that the gauge-fixing term, $F[U^g]$, attain a local minimum. It is impractical to search for the absolute minimum. This approach has been widely accepted in the literature [64].

This procedure defines a gauge-fixing scheme which avoids the problem of Gribov copies. The term "soft" is used to describe gauges defined in this way because of the normalised probability which the scheme creates on the gauge orbit. By enforcing these "soft" gauge-fixing conditions, a gauge is uniquely specified as a probability distribution on the gauge orbit, thus avoiding the choice of any one configuration, which in this language would be a "hard" gauge-fixing condition *e.g.* Landau gauge.

4.5 The Gauge-Fixing Algorithm

The double average structure of the expectation value suggests the use of a Monte Carlo algorithm, which will be implemented in two steps :

A set of link configurations, $\{U_1, \ldots, U_N\}$, weighted by the Wilson action is produced in the usual way, with a gauge-invariant Monte Carlo algorithm for some value of β.

Each of these configurations is then used in a second Monte Carlo step where the dynamical variables that get updated are the group elements, $g(n)$ that live on the lattice sites.

Thus, for each link configuration one can generate a set of gauge-related configurations and the expectation value of a gauge-dependent observable is obtained by evaluating all its ensemble averages and summing all together as

$$\langle \mathcal{O} \rangle_{\text{mod}} = \frac{1}{N} \sum_{i=1}^{N} \langle\, \mathcal{O}[U_i] \,\rangle_G. \tag{4.23}$$

A family of gauges is defined by varying the gauge-fixing parameter, M^2. The gauge dependence of quantities can then be studied. For small values of βM^2 ($\sim$ high temperature) the results from a numerical simulation will be compared with analytic calculations using a strong-coupling expansion. This is outlined in the next subsection. For higher values of βM^2 ($\sim$ low temperature) this work can be compared with results of a continuum, weak-coupling analysis, valid for all M^2. This is discussed in the final subsection.

4.5.1 Strong-Coupling Expansion

A strong-coupling expansion is an expansion in powers of the inverse coupling. Analytic calculations using a generalised, strong-coupling in the lattice gauge-fixed prescription described above, are a useful check on the low βM^2 *i.e.* high effective temperature region, of this scheme.

Traditionally, a strong-coupling expansion is infrequently used because it does not have a continuum limit. In a gauge-invariant lattice model it can provide only qualitative information. Here however, it may be of some use since the gauge-fixing parameter, M^2, is always manifest, it should be possible to trace any gauge-independent features of the gauge-dependent observables calculated.

In [52] it was shown that for small β and M^2 the strong-coupling expansion of the expectation value of a gauge-dependent observable can be done in two steps :

> The first is a strong-coupling expansion of the average over the gauge group, $\langle\, \mathcal{O}[U_i] \,\rangle_G$, which gives a sum of gauge-invariant terms.
>
> Secondly, each of these terms is evaluated in the usual way, using a strong-coupling expansion of the Wilson average ($\langle\,\rangle_W$). Finally the terms are regrouped, order by order in β.

In §4.6.2, for a test case, where $U_\mu(x) \equiv \mathbf{1}$, the internal energy is compared to results from an expansion to lowest order. For the full averaging *i.e.* including $U_\mu(x) \neq \mathbf{1}$, the numerical results of the gauge-fixed energy function are compared with a strong-coupling expansion, to second order at $\beta = 5.7$.

4.6 Results : The Algorithm and Thermodynamics of the System

The aim of this project is to determine if an efficient numerical implementation of the algorithm proposed in §4.5 is possible. This section is organised as follows: the lattice definitions of the three quantities measured, are given. These are the internal energy, the specific heat and the gluon propagator. Initial investigations of the algorithm and the thermodynamics are described for the case $U_\mu(x) = \mathbf{1}$ and then a more complete study is carried out, at $\beta = 5.7$, for non-trivial $U_\mu(x)$. Finally, first attempts at determining the gauge-dependence of the gluon propagator are made.

4.6.1 Definitions

Two quantities are monitored while investigating the thermodynamics of the system :

The internal energy :

$$\begin{aligned} \langle E \rangle &\equiv F[U^g_\mu(x)] \quad , \\ &= \langle \sum_{x,\mu} \Re\mathrm{eTr}\left[U^g_\mu(x)\right] \rangle, \end{aligned} \tag{4.24}$$

which, for the test case, is defined to be

$$\langle E \rangle = \langle \sum_{x,\mu} \Re\mathrm{eTr}\left[\mathbf{1}^g\right] \rangle \tag{4.25}$$

The specific heat :

$$\begin{aligned} c &= \frac{1}{\beta M^2} \frac{dE}{d(\beta M^2)}, \\ &= \langle E^2 \rangle - \langle E \rangle^2. \end{aligned} \tag{4.26}$$

Again, for the case $U_\mu(x) = \mathbf{1}$, the definition is

$$c = \frac{1}{M^2} \frac{dE}{dM^2}. \tag{4.27}$$

The gluon propagator

The zero-momentum gluon propagator is used to define the autocorrelation times of the algorithm. The lattice gluon field is defined in the standard way as [62]

$$A_\mu(x) = \frac{U_\mu(x) - U_\mu^\dagger(x)}{2iag_0} - \frac{1}{3}\mathrm{Tr}\left[\frac{U_\mu(x) - U_\mu^\dagger(x)}{2iag_0}\right], \tag{4.28}$$

with a bare coupling, g_0, and a lattice spacing, a. A general, n-point Green function is defined in momentum space, by Fourier transforming this field, such that

$$G^{(n)}_{\mu_1 \ldots \mu_n}(p_1 \ldots p_n) = \langle\, A_{\mu_1}(p_1) \ldots A_{\mu_n}(p_n) \,\rangle, \tag{4.29}$$

and from this, the gluon propagator is

$$G^{(2)}_{\mu\nu} = \langle\, A_\mu(p) A_\nu(-p) \,\rangle. \tag{4.30}$$

In particular, the zero-momentum propagator is

$$G^{(2)}(0) = \langle\, A_\mu(0) A_\nu^\dagger(0) \,\rangle. \tag{4.31}$$

4.6.2 A Test Case

The viability of the algorithm depends on the second step: updating the $g(n)$ by an integration over the group of gauge transformations. This is the new step and may be subject to critical slowing down. This can be explicitly tested, by using a "cold" start in the updating process. The link variables are set equal to the identity, $U_\mu(x) = \mathbf{1}$, corresponding to taking, $\beta \longrightarrow \infty$, and generating pure gauge configurations with a weight, $\exp^{-M^2 F[\mathbf{1}^g]}$. No Wilson averaging is done.

The system can be considered as a four-dimensional, $SU(3)$ spin-model For the purposes of this test case there is no Wilson average, as already mentioned and the specific heat is defined by Equation (4.27). Figures 4.1 and 4.2 show the internal energy and the specific heat, respectively. In both, it appears there is a

first-order transition, at $M^2 \approx 0.635$. This behaviour agrees with a study of the

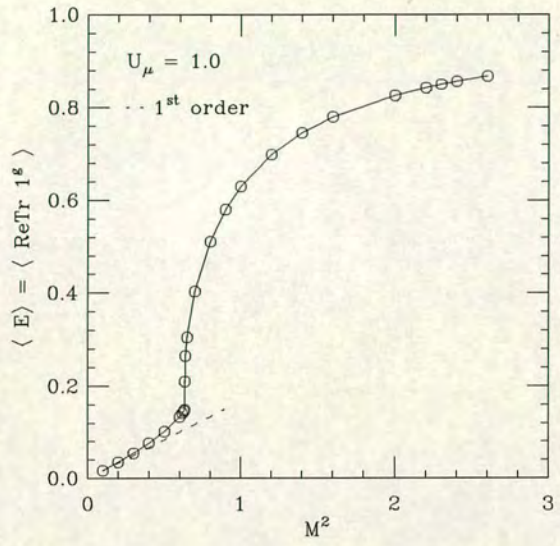

Figure 4.1: The internal energy as a function of M^2 for the case $U_\mu(x) = \mathbf{1}$. The dashed line is the strong-coupling expansion to lowest order in M^2. The numerical and analytical results agree up to $M^2 \approx 0.4$.

three-dimensional case in the literature by Kogut and collaborators [53]. They also see evidence of a first-order phase transition as β (the effective temperature of their model) is increased. The behaviour of both their energy function and the specific heat is qualitatively similar to that of Figures 4.1 and 4.2.

4.6.3 A Study at $\beta = 5.7$

The test case showed that the second step of the algorithm, the average over the gauge group, gives reasonable results. However, a realistic study must be done to test the double average structure. This was carried out at $\beta = 5.7$, on an 8^4 lattice. The gauge configurations, $\{U_1 \ldots U_N\}$, were generated on a single processor DEC-Alpha machine, using the Wilson pure-gauge action, as defined in Chapter 1 and a hybrid-overrelaxed algorithm. Two update sweeps, comprising a combination of 1 Cabibbo-Marinari (CM) pseudo-heatbath and 4 overrelaxed (OR) steps, are

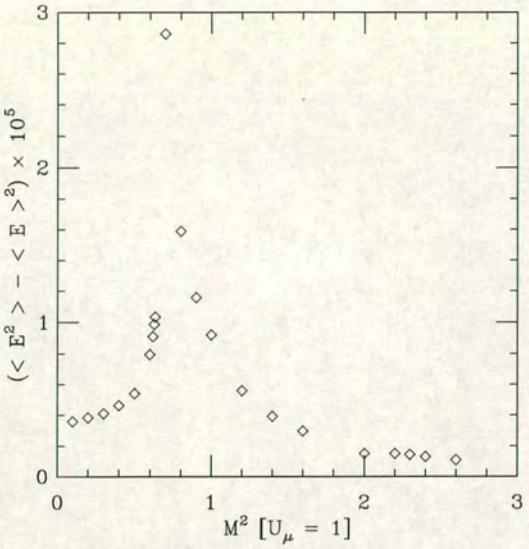

Figure 4.2: The specific heat capacity defined as in Equation (4.27) for the case $U_\mu(x) = \mathbf{1}$ which appears to show a first order phase transition at $M^2 \approx 0.65$

used on three $SU(2)$ subgroups. Configurations are well separated and 21 in total are generated.

Before a study of gauge dependence can be made, a range of values of the gauge-fixing parameter, M^2, must be identified over which the algorithm performs efficiently and successfully. If it is to be implemented as a valid gauge-fixing tool it must be shown to cope with critical slowing down and to be valid for a window of M^2 values.

As in the test case, the thermodynamics are monitored by recording the internal energy and the specific heat. Initial runs are made with different seeds for the random number generator. Some seed dependence is found for both the internal energy and the zero-momentum gluon propagator, as described by Table 4.1. However, it is found that tuning the number of overrelaxed to Cabibbo-Marinari steps, cures this problem.

In tests of the algorithm, the zero-momentum gluon propagator is found to have

OR	$G^{(2)}(0)$	Seed	βM^2
2	$13.202^{+\ 8}_{-\ 8}$	45623	1.8
2	13.034^{+10}_{-10}	9876	1.8

Table 4.1: Values of the zero momentum gluon propagator for different seeds at $\beta M^2 = 1.8$ and for 2 OR steps.

"metastable" states *i.e.* long-lived false plateaux which eventually decay to the correct vacuum state. These metastable states occur in the gluon propagator because it is a non-local quantity, where for higher values of βM^2, the algorithm is sensitive to the energy landscape. The energy function[3], $\langle E \rangle_G$, thermalises easily at all βM^2 values since it is a local observable and metastable states are not found. An example of metastability is shown in Figure 4.3. Again, by tuning the ratio of OR to CM steps the algorithm is made to thermalise correctly, for the range of values studied.

The study is done for the range, $0 < \beta M^2 \leq 2.4$. In the range $0.8 \leq \beta M^2 < 2.4$, 21 configurations are generated. For each configuration, an ensemble of 60 gauge-related configurations is then produced. In the strong-coupling regime the statistics are lower: 10 configurations, for $0 < \beta M^2 < 0.8$, with 15 gauge-related configurations. All errors quoted are jackknife estimates and are generally small.

4.6.4 Autocorrelations

The autocorrelation times for an algorithm give an indication of its efficiency. As mentioned in the previous section the zero-momentum gluon propagator is a non-local quantity and so it is expected to be sensitive to long wavelength modes of the system. Its autocorrelation times will therefore provide an accurate measurement of the efficiency of the algorithm. In general, in an updating process, subsequent configurations are rarely completely statistically independent (decorrelated). The correlation between generated configurations is called the autocorrelation.

Measurements of the autocorrelation times

[3] $\langle E \rangle_G$ denotes the average defined by Equation (4.21).

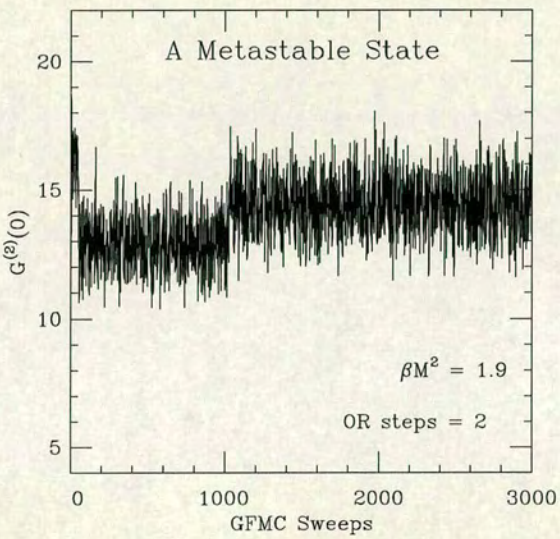

Figure 4.3: The evolution of the zero-momentum gluon propagator with the number of sweeps, showing a metastable state. This was subsequently cured by increasing the number of overrelaxed steps to 10.

A practical means of determining the autocorrelation times is by binning the data. For a long sequence, this involves building blocks of configurations and then averaging quantities in these bins. These averages are treated as single measurements and are used to calculate the variances. If the bin-size is greater than the autocorrelation length, the bin-averages are uncorrelated. The normalised autocorrelation function, $\rho(t)$, is defined as

$$\rho(t) = \frac{\langle A_i A_{i+t} \rangle - \langle A_i \rangle^2}{\langle A_i^2 \rangle - \langle A_i \rangle^2}. \tag{4.32}$$

For large t, this decays exponentially and so the exponential autocorrelation time is defined as

$$\tau_{\text{exp}} \equiv \limsup_{t \to \infty} \frac{t}{-\log |\rho(t)|}, \tag{4.33}$$

and indicates how many sweeps should be thrown away at the beginning of a run. The integrated autocorrelation time is

$$\tau_{\text{int}} \equiv \frac{1}{2} + \sum_{t=1}^{\infty} \rho(t). \tag{4.34}$$

It estimates the number of statistically independent configurations there are in the dataset and so, how many should be skipped between measurements. The exponential autocorrelation times of the zero-momentum gluon propagator, using 2 and 10 OR steps, are in Table 4.2. The integrated autocorrelation time for the range of βM^2 is found to be approximately 1 for both 2 and 10 overrelaxed steps and so is not quoted in Table 4.2. The autocorrelation times are low, an average value being $\approx$ 4 GFMC sweeps[4]. This is encouraging, thermalisation is rapidly achieved and meaningful measurements can be taken at an early stage in the evolution of an observable.

4.6.5 The Specific Heat and the Energy

The phase transition observed in the test case, where $U_\mu(x) = \mathbf{1}$, survives for $U_\mu(x) \neq \mathbf{1}$, at $\beta M^2 \approx 0.89$. This transition is monitored by the behaviour of

[4]GFMC, is a gauge-fixing Monte Carlo sweep, comprising the OR and CM steps.

βM^2	# OR	τ_{exp} (sweeps)
0.2	2	2
0.4	2	3
0.6	2	1
0.62	2	4
0.66	2	3
0.7	2	3
0.8	10	3
1.0	10	2
1.14	10	1
1.25	10	2
1.5	10	3
1.7	10	3
1.9	10	4
2.0	10	3
2.2	10	6
2.4	10	3

Table 4.2: The exponential autocorrelation times for the zero momentum gluon propagator at $\beta = 5.7$. The time is measured in GFMC sweeps, where 1 GFMC sweeps is $2 \times (\#\text{OR} + 2\text{CM})$. The average exponential time is ≈ 4 GFMC sweeps.

the specific heat defined by Equation (4.26) and is shown in Figure 4.4 where it appears to be a first-order transition. The pattern is qualitatively similar to the test case in §4.6.2.

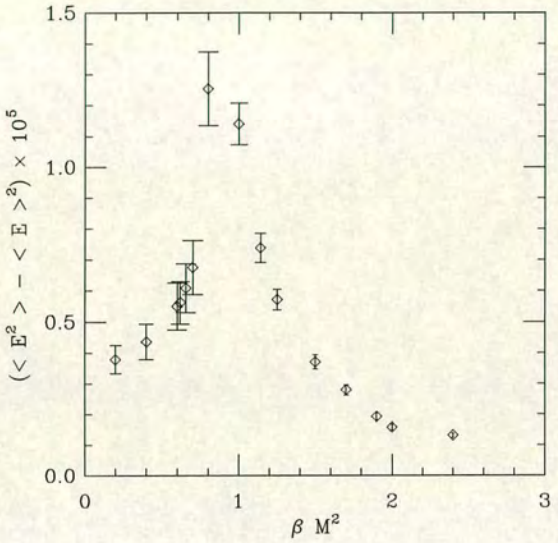

Figure 4.4: Specific heat capacity at $\beta = 5.7$. The phase transition occurs at ≈ 0.89. The errors are statistical and determined by a jackknife analysis.

The variation of the energy with M^2 is shown in Figure 4.5. The dashed line represents the strong-coupling expansion of the energy function to $\mathcal{O}((\beta M^2)^2)$. For small values of βM^2 *i.e.* high temperature, these agree extremely well, as expected, up to $\beta M^2 \approx 0.7$.

As expected from the discussion in §4.4, the energy measured in this family of gauges increases monotonically towards the Landau gauge value of 0.8201^{+6}_{-6}, as M^2 is increased.

The phase transition separates the data into two regions. There is a strong-coupling region at low values of βM^2, for which the data show very little gauge dependence; in fact the effect of the gauge-fixing term is decreasing and as $\beta M^2 \longrightarrow 0$ no gauge-fixing is being done. This is not unexpected, since low βM^2 corre-

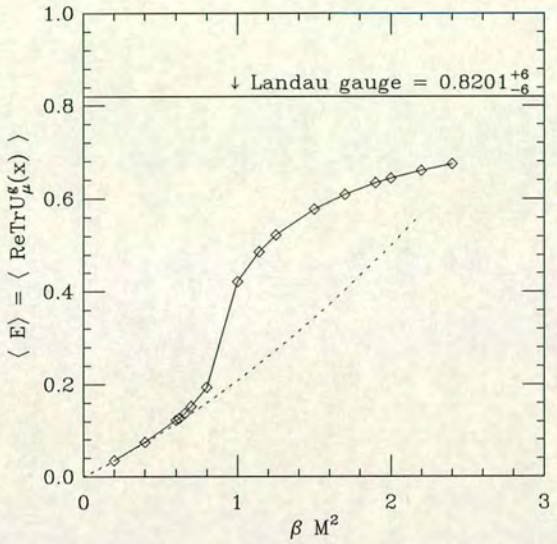

Figure 4.5: The internal energy of the system. The strong coupling expansion and the numerical results are seen to agree closely, up to at least $\beta M^2 \approx 0.7$.

sponds to a high-temperature region. Thermal fluctations here tend to randomise the system because the energy cost to create these excitations is low (compared to kT). This will tend to suppress any gauge-dependence. There is a weak-coupling regime, at higher values of βM^2 for which the system shows a strong dependence on M^2. The gluon propagator is studied in this region, as described in the next section.

4.7 Gauge Dependence of the Gluon Propagator

As discussed at the beginning of this chapter, the gluon propagator will play an important rôle in an understanding of confinement. In pure gluonic QCD, a dynamically-generated mass scale has been predicted because the confinement potential $V(r) = Kr$ contains such a scale. The non-perturbative, continuum, Euclidean, gluon propagator has been the subject of much investigation [50, 56, 57, 58, 59, 60]. In minimal Landau gauge (described in §4.4), a peculiar momentum dependence of the gluon propagator is predicted [50, 58]. Recall that this gauge

is implemented by tightening the traditional Landau gauge-fixing condition to

$$\partial_\mu A^\mu(x) = 0 \quad \text{and} \quad \det FP > 0, \tag{4.35}$$

getting rid of most, though not all [61], Gribov copies. The proposed form of the transverse propagator in momentum space is

$$G(k) \sim \frac{k^2}{k^4 + b^4}, \tag{4.36}$$

where b is the dynamically-generated mass scale.

How to interpret this form is as yet unclear. However, the absence of a particle singularity on the k^2 axis would imply the absence of an asymptotic gluon state. This could be a short-lived excitation emitting a gluon jet or b may correspond to a hadronisation scale. An important point in any future analysis will be the gauge dependence of the gluon propagator and in particular the extraction of any gauge-independent features.

4.7.1 The Lattice Gluon Propagator

The lattice gluon propagator has also been extensively investigated, at different lattice sizes and spacings. The authors [63] have analysed the gluon propagator on four lattices at three lattice spacings, $\beta = 5.7, 6.0$ and 6.3, (two lattices at $\beta = 6.0$), in the minimal Landau gauge of Equation (4.35). They find evidence for dynamical mass generation in this gauge. The aim of this work is to study the gauge dependence of the propagator. For this purpose, from Equation (4.30), the following definition of the propagator is used

$$G^{(2)}_{\text{scalar}}(p) = \sum_{\mu=1\ldots4} \langle A_\mu(p) A^\dagger_\mu(p) \rangle, \tag{4.37}$$

where the expectation value is evaluated in the modified scheme, including all gauge group and Wilson averages.

The evolution of the zero-momentum gluon propagator with βM^2, is shown in Figure 4.6. Below the phase transition there is little effect with changing M^2 but

again the argument about the suppression of gauge-dependence as a consequence of high temperature effects, applies here. Above the phase transition, there is a strong gauge dependence. The propagator increases monotonically with M^2 towards the asymptotic Landau gauge value. The gluon propagator as a function

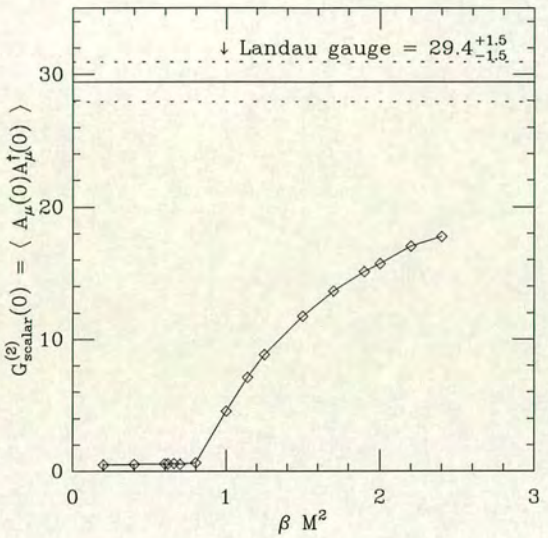

Figure 4.6: The zero momentum gluon propagator as βM^2 is varied in the range $0 < \beta M^2 \leq 2.4$

of the momentum in different gauges, is studied, by varying M^2. This is shown in Figure 4.7. Again, the Landau gauge value is included and the behaviour of $G(p)$ with p is qualitatively the same in all gauges. Gauge dependence decreasing with increasing momentum is observed. However, since discretisation effects become more important at higher momenta, values of p above $2(2\pi)/L$, where $pa \sim 1$, may be unreliable. There is, however, clear evidence for a strongly gauge-dependent zero-momentum gluon propagator and this may have consequences for dynamical-mass generation.

An important point is that this scheme is not proposed to enable a comparison with, or an extrapolation to, Landau gauge but rather it allows a determination

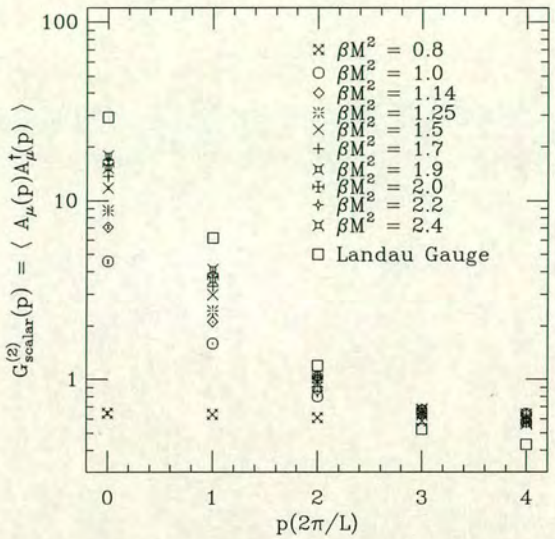

Figure 4.7: The finite momentum gluon propagator as a function of the momentum, p, as βM^2 is varied in the range $0.8 < \beta M^2 \leq 2.4$

of the gauge dependence of, *e.g.* the gluon propagator, in a range of well-defined gauges.

4.8 The Continuum Limit of this Lattice Scheme

In order to draw firm conclusions about this gauge-fixing, it is necessary to make contact with the continuum limit of the scheme. In practice, it is not expected that all values of M^2 will have a continuum limit, since the data show that as M^2 decreases towards zero, the signal to noise ratio deteriorates and no gauge-fixing is done. This is clear from both Figure 4.5 and Figure 4.6. The objective is therefore to isolate a window of M^2, where there is scaling. To do this, it is necessary to study both the M^2 and the β dependence of the scheme. A study of the β dependence was beyond the scope of this initial investigation. However, preliminary attempts at a study of the continuum limit are possible. A weak-coupling, perturbative study of the continuum version of this gauge-fixing scheme has been done by Fachin [68]. He found that the gluon propagator in k-space can

be expressed as

$$D^{ab}_{\mu\nu}(k) = \delta^{ab}\left[\frac{1}{k}\mathbf{P}^{T}_{\mu\nu}(k) + \frac{1}{M^2}\mathbf{P}^{L}_{\mu\nu}(k)\right], \tag{4.38}$$

where $\mathbf{P}^T$ and $\mathbf{P}^L$ are the projections of the transverse and longitudinal components, respectively

$$\mathbf{P}^{T}_{\mu\nu}(k) = \delta_{\mu\nu} - \frac{k_\mu k_\nu}{k^2}, \tag{4.39}$$

$$\mathbf{P}^{L}_{\mu\nu}(k) = \frac{k_\mu k_\nu}{k^2}. \tag{4.40}$$

A summary of his calculations is

- To all orders in perturbation theory there are no radiative corrections to the transverse part of the propagator.
- The propagator reduces, in the $M^2 \longrightarrow \infty$ limit, to the usual Landau gauge form.
- The M^2-dependent propagator can be used to show that the gauge dependence vanishes, for the vacuum expectation value of a gauge-invariant quantity.

Using the first of these points and defining, $p_0 \equiv (p, 0, 0, 0)$, implies the gluon propagator can be written,

$$M^2 G_{11}(0) = \text{constant}. \tag{4.41}$$

This expression is used to examine the onset of continuum behaviour, for a fixed β. The idea is that for varying M^2, Equation (4.41) holds. The results are plotted in Figure 4.8, where M^2 has been varied in the range $0.8 \leq \beta M^2 \leq 2.4$. There are two points to be considered from these results. The first is that the data are constant for all values of momenta. This indicates that UV lattice artefacts are under control, even for this low β value, where finite-volume effects might be expected to be noticeable. The second point is that the data do not reproduce the

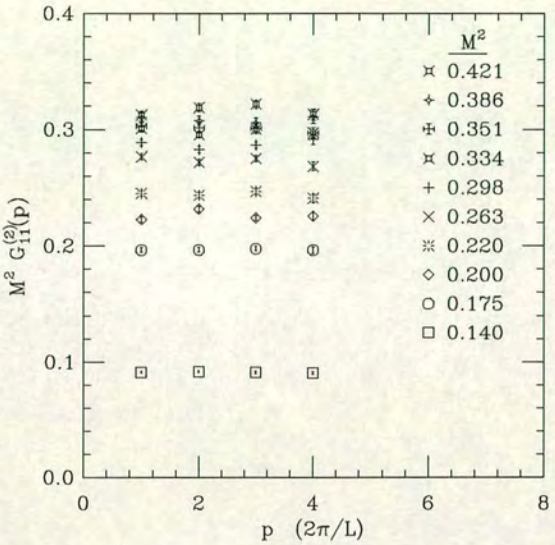

Figure 4.8: $M^2 G_{11}(p)$ plotted against the momentum in units of $2\pi/L$ as a test of the tensor structure of the gluon propagator.

perturbative continuum behaviour described by Equation (4.41). This could be an effect of working at a low β value, which is far from the continuum. A second possibility is that the range of M^2 values used in this study does not have a limit in the continuum theory. Finally, these results have not been renormalised, since the renormalisation constant (and its possible M^2 dependence) is unknown. It is interesting to note that the M^2 dependence decreases as M^2 is increased.

4.9 Summary

An algorithm designed to gauge-fix stochastically has been shown to be efficient and to produce meaningful results. Autocorrelation times are low and it is believed that by tuning the number and type of update sweeps used, metastable states are not a problem.

There is evidence of a first-order phase transition at $\beta M^2 \approx 0.85$ for $\beta = 5.7$. This should not be understood as a "physical" phase transition but rather as a feature of the gauge dependence of the observables studied. Numerical and

analytical (strong-coupling) analyses agree in the region where such a comparison is legitimate.

The main observation of this chapter is that the gauge dependence of both the zero-momentum and finite-momentum gluon propagators is substantial. This may have strong implications for any dynamically-generated mass, particularly if any physical meaning is to be attached to it. An important point is, therefore, the existence of gauge-invariant features of the propagator. The gauge-fixing scheme described and tested here will, in principle, bring to light any such features.

Chapter 5

Conclusions

Much progress has been made in simulating hadronic physics in Lattice QCD since the first work done in the early 1980s [70]. The increases in computer power and efficiency of QCD algorithms has allowed more and more accurate determinations of hadron masses and matrix elements to be made. Statistical errors on these quantities are now, in general, under control : in this work, the statistical error on hadronic quantities is between 1 and 3%. This means that systematic effects can be explored. Of these, most effort is being concentrated on reducing discretisation effects and identifying errors due to quenching the theory. To reduce errors due to the non-zero lattice spacing, one can either make the lattice spacing finer or implement Symanzik's improvement programme. The computational cost of a QCD calculation rises like $1/a^6$ so the former quickly becomes impractical. Improvement, on the other hand has been shown to be a powerful and practical tool *e.g.* the authors in [71] have extracted the static quark potential and charmonium with improved glue, from lattices of $a = 0.4$fm. The hope is that the improvement programme in conjunction with tadpole improvement, as described in Chapter 2 will lead to full improvement of the QCD action.

Quenching effects are more difficult to quantify. Only by controlling the other systematic errors will they become clear. The alternative is to compare a calculation in the unquenched theory with results from a quenched simulation. This should soon become possible, work is already being done in this area, using both staggered and Wilson quarks [72, 73, 74].

For Lattice QCD the aims are therefore to determine accurately, in the quenched approximation, hadronic quantities and to establish the validity of quenching the theory by a comparison with a calculation in full QCD.

The motivation for the study of covariant, non-perturbative gauge-fixing, in the second part of this thesis, was to verify that a successful algorithm could be found, with which the gauge dependence of quantities could be studied. This proved possible, in particular the gauge dependence of the gluon propagator appears to be quite substantial. However, the continuum limit of this scheme must now be investigated. This will be done by repeating the analysis at a higher β and for a wider range of the gauge-fixing parameter, to arrive at a range of M^2 values for which β can be varied and for which the results scale. It will then be possible to study the continuum limit and establish the relevance of results to continuum physics.

References

[1] I. Montvay and G. Münster, *Quantum Fields on a Lattice*, Cambridge University Press, Cambridge (1994).

[2] H.J. Rothe *Lattice Gauge Theories*, World Scientific, Singapore (1992).

[3] D. Gross and F. Wilczek, Phys. Rev. **D8**, 3688 (1973). and Phys. Rev. Lett. **30**, 1343 (1973).

[4] H.D. Politzer, Phys. Rev. Lett. 30 (1973) 1346.

[5] G. t'Hooft, (1972) Marseille Conference on Yang-Mills fields.

[6] Given by *Dyson's formula*, see *e.g.* [1] page 96.

[7] H.B. Nielson and M. Ninomiya, Nucl. Phys. **B185**, 20 (1981).

[8] K.G. Wilson, Phys. Rev **D14**, 2455 (1974).

[9] M. Creutz, Phys. Rev. Lett. **43**, 553 (1979) and Phys. Rev. Lett. **43**, 890 (1979).

[10] K.G. Wilson, Adv. Math **16**, 176 (1975).

[11] K. Symanzik, Some topics in quantum field theory. Mathematical problems in theoretical physics : eds : R.Schrader et al. Lecture Notes in Physics, Vol. 153, Springer New York (1982).

[12] K. Symnazik, Nucl.Phys **B226**, 187 and 205 (1983).

[13] B. Sheikholeslami and R. Wohlert. Nucl. Phys **B259**, 572 (1985).

[14] C.R. Allton *et al.* , UKQCD Collaboration, hep-lat/9205016, Phys. Lett. **B284**, 377 (1992).

[15] G. Heatlie *et al.* , Nucl. Phys **B352**, 266 (1991).

[16] E. Gabrielli *et al.* , Nucl. Phys. **B362**, 475 (1991).

[17] M. Teper, Phys. Lett. **B183**, 345 (1986).

[18] P. Lacock *et al.* , UKQCD Collaboration, Phys. Rev **D51**, 6403 (1995).

[19] C.R. Allton *et. al*, UKQCD Collaboration, ED 92/513

[20] L.D. Fadeev and V.N. Popov, Phys. Lett. **B25**, 30 (1967).

[21] D.K. Sinclair, hep-lat/9509058, Plenary review talk at Lattice'95.

[22] N. Metropolis, A.W. Rosenbluth, M.N. Metropolis, A.H. Teller and E. Teller, J. Chem. Phys. **21**, 1087 (1953).

[23] C.R. Allton *et al.* , UKQCD Collaboration, Phys. Rev. **D49**, 474 (1994).

[24] M. Alford *et al.* , hep-lat/9509087, Nucl. Phys **B47**, 370 (proc. suppl.) (1996).

[25] G.P. Lepage and P.B. Mackenzie, hep-lat/9209022, Phys. Rev. **D48**, 2250 (1993).

[26] S. Sharpe, Phys. Rev. **D41**, 3233 (1990) and Phys. Rev. **D46**, 3146 (1992).

[27] T. Bhattacharya *et al.* , hep-lat/9512021.

[28] H.P. Shanahan *et al.* , hep-lat/9608063, submitted to Phys. Rev. **D**.

[29] N. Stella, University of Southampton thesis.

[30] D.S. Henty *et al.* , hep-lat/9412088, Phys. Rev. **D51**, 5323 (1995).

[31] P.A. Rowland, to be published in *Proceedings of Lattice'96.*

[32] F. Butler *et al.* , hep-lat/9302012.

[33] A.X. El-Khadra, G.H. Hockney, A.S. Kronfeld and P.B. Mackenzie, Phys. Rev. Lett. **69**, 729 (1992).

[34] F. Butler *et al.* , GF11 Collaboration, Nucl. Phys. **B430**, 179 (1990).

[35] H.R.Fiebig and R.M.Woloshyn, hep-lat/9603001 (1996)

[36] S.R. Beane, Duke University preprint DUKE-TH-95-98, hep-ph/9512228 (1995).

[37] APE Collaboration, S. Cabasino *et al.* , Phys. Lett. **B258**, 195 (1991).

[38] M. Lüscher *et al.* , hep-lat 9605038.

[39] R.D. Kenway *et al.* , hep-lat/9608034, to be published in *Proceedings of Lattice'96.*

[40] P. Lacock and C. Michael, Phys. Rev **D52**, 5213 (1995).

[41] S. Naik, Phys. Lett **B311**, 230 (1993).

[42] C.R. Allton *et al.* , UKQCD Collaboration, hep-lat/9208018, Phys. Lett **B292**, 408 (1992).

[43] C.T. Sachrajda, *From Actions to Answers*, editors : T. DeGrand and D. Toussaint, TASI, World Scientific (1990)

[44] C. Michael, H.P. Shanahan, UKQCD Collaboration, hep-lat/9509083, Nucl. Phys. **B**, (proc. suppl.) (1995).

[45] G.S. Bali and K. Schilling, hep-lat/9208028, Phys. Rev. **D47**, 661 (1993).

[46] H.R. Fiebig and R.M. Woloshyn, hep-lat/9607058.

[47] H. Lipps, G. Martinelli, R. Petronzio and F. Rapuano, Phys. Lett. **B126**, 250 (1983).

[48] S. Gottlieb, hep-lat/9608107, plenary talk at Lattice96.

[49] S. Sharpe, Phys. Rev. **D41**, 3233 (1990) and Phys. Rev. **D46**, 3246 (1992).

[50] V.N. Gribov, Nucl. Phys. **B139**, 1 (1978).

[51] D. Zwanziger, Phys. Lett. **B257**, 168 (1991).

[52] C. Parrinello, G. Jona-Lasinio, Phys. Lett. **B251**, 175 (1990).
D. Zwanziger, Nucl. Phys. **B139**, 461 (1990).

[53] J. Kogut, M. Snow and M. Stone, Nucl. Phys. **B200**, 211 (1982)

[54] E. Marinari, C. Parrinello, Nucl. Phys. **B362**, 487 (1991).

[55] S.P. Fachin, C. Parrinello, Phys. Rev. **D44**, 2558 (1991).

[56] J.M. Cornwall, Phys. Rev. **D26**, 1453 (1982).

[57] M. Stingl, Phys. Rev. **D34**, 3863 (1986) and U. Haber *et al.* Z. Phys. **A336**, 435 (1990).

[58] D. Zwanziger Nucl. Phys. **B378**, 525 (1992).

[59] J.M. Namislowski, Invited talk at the First German-Polish Symposium on Particles and Fields, Rydzyna, April 28-May 1, 1992.

[60] S. Mandalstam, Phys. Rev. **D20**, 3223 (1979) and M. Baker, S.J. Ball and F. Zachariasen Nucl. Phys. **B186**, 531 (1981).

[61] M.A. Semenov-Tyan-Shansky and V.A. Franke, Report for the Steklov Institute (Leningrad) 1982.

[62] J.E. Mandula, M. Ogilvie, Phys. Lett. **B185**, 127 (1987).

[63] C. Bernard, C. Parrinello and A. Soni, Phys. Rev. **D49**, 1585 (1994).

[64] P. Marenzoni, G. Martinelli, N. Stella and M. Testa, Phys. Lett. **B318**, 311 (1993). C. Bernard, C. Parrinello and A. Soni, Phys. Rev. **D49**, 1585 (1994).

[65] B. Alles, D. Henty, H. Panagopoulos, C. Parrinello and C. Pittori, LTH-367, hep-lat/9605033, submitted to Nucl. Phys. **B**.

[66] G. Martinelli, C. Pittori, C.T. Sachrajda, M. Testa and A. Vladikas, Nucl. Phys. **B445**, 81 (1995).

[67] M. Lüscher, S. Sint, R. Sommer, P. Weisz, H. Wittig and U. Wolff, hep-lat/9608049, Lattice96 (proc. suppl.).

[68] S.P. Fachin, Phys. Rev. **D47**, 3487 (1993).

[69] D. Henty, O. Oliveira, C. Parrinello and S. Ryan, hep-lat/9607014, submitted to Phys. Rev. **D**.

[70] D. Weingarten, Phys. Lett. **B109**, 57 (1982). and H. Hamber and G. Parisi, Phys. Rev. Lett. **47**, 1792 (1981).

[71] M. Alford *et al.* , hep-lat/9507010 and Nucl. Phys. **B47** (proc. suppl.), 787 (1995).

[72] J. H. Sloan, Nucl. Phys. **B47** (proc. suppl.), 378 (1995).

[73] U. Glaessner *et al.* , Nucl. Phys. **B47** (proc. suppl.), 386 (1996).

[74] L. Conti *et al.* , Nucl. Phys. **B47** (proc. suppl.), (1996).